



Min, Guanbo (2022) *Optimisation of Triboelectric Nanogenerator performance in vertical contact-separation mode*. PhD thesis.

<https://theses.gla.ac.uk/82889/>

Copyright and moral rights for this work are retained by the author

A copy can be downloaded for personal non-commercial research or study, without prior permission or charge

This work cannot be reproduced or quoted extensively from without first obtaining permission in writing from the author

The content must not be changed in any way or sold commercially in any format or medium without the formal permission of the author

When referring to this work, full bibliographic details including the author, title, awarding institution and date of the thesis must be given

Enlighten: Theses

<https://theses.gla.ac.uk/>
research-enlighten@glasgow.ac.uk



University
of Glasgow

Optimisation of Triboelectric Nanogenerator Performance in Vertical Contact-Separation Mode

Guanbo Min

A thesis submitted to the James Watt School of Engineering at the University of
Glasgow in partial fulfilment of the requirements for the Degree of Doctor of

Philosophy

February, 2022

Abstract

Triboelectric nanogenerator (TENG) is one of the most promising energy harvesters – a technology that uses repeated or reciprocating contact of suitably chosen materials to generate charge via the triboelectric effect (TE) and utilizes this as usable voltage and current. TENGs are attractive as they can continuously generate charge over a wide range of operating conditions and have several valuable advantages such as light weight, simple structure, low cost and high efficiency. Therefore, TENGs have been explored in a wide range of applications, including self-powered wearable electronics, powering electronics and even for harvesting ocean wave/wind energy. One of the major limitations of TENGs is their low power output (usually $<500 \text{ W/m}^2$). This thesis focuses on a few specific approaches to optimising TENG output performance. This thesis begins by presenting a solution to this challenge by optimizing a low permittivity substrate beneath the tribo-contact layer. The open circuit voltage is found to increase by a factor of 1.3 in moving from PET to the lower permittivity PTFE. TENG performance is also believed to depend on contact force, but the origin of the dependence had not previously been explored. Herein, we show that this behaviour results from a contact force dependent real contact area A_r as governed by surface roughness. The open circuit voltage V_{oc} , short circuit current I_{sc} and A_r for a TENG were found to increase with contact force/pressure. Critically, V_{oc} and I_{sc} saturate at the same contact pressure as A_r suggesting that electrical output follows the same evolution as A_r . Assuming that tribo-charges can only transfer across the interface at areas of real contact, it follows that an increasing A_r with contact pressure should produce a corresponding increase in the electrical output. These results underline the importance of accounting for real contact area in TENG design, as well as the distinction between real and nominal contact area in tribo-charge density definition. High-performance ferroelectric-assisted TENGs (Fe-TENGs) are developed using electrospun fibrous surfaces based on P(VDF-TrFE) with dispersed BaTiO₃ (BTO) nanofillers in either cubic (CBTO) or tetragonal (TBTO) form in this thesis. TENGs with three types of tribo-negative surface were investigated and output increased progressively. Critically, P(VDF-TrFE)/TBTO produced higher output than P(VDF-TrFE)/CBTO even though permittivity is nearly identical. Thus, it is shown that BTO fillers boost output, not just by increasing permittivity, but also by enhancing the crystallinity and amount of the β -phase (as TBTO produced a more crystalline β -phase present in greater amounts)

Table of contents

<i>Abstract</i>	1
<i>Table of contents</i>	2
<i>List of figures</i>	5
<i>List of tables</i>	10
<i>List of publications and awards</i>	11
<i>Glossary of abbreviations</i>	14
<i>Chapter I</i>	15
<i>Introduction</i>	15
1.1 Motivation	15
1.2 Research objectives	17
1.3 Key contributions of this thesis	17
1.4 Structure of the thesis	19
<i>Chapter II</i>	21
<i>Literature Review</i>	21
2.1 New energy resources	21
2.1.1. Renewable energy.....	21
2.1.2. Micro/nano energy	24
2.2 Triboelectric nanogenerator	28
2.2.1 Triboelectrification.....	28
2.2.2 Working principle of triboelectric nanogenerators.....	29
2.2.3 The modes of triboelectric nanogenerators	31
2.3 Triboelectrification of materials.....	37
2.4 Research progress on triboelectric nanogenerators.....	46
2.5 Summary	61
<i>Chapter III</i>	63
<i>Modelling, simulation and optimization for contact and separation mode triboelectric nanogenerators</i>	63
3.1 Introduction	63
3.2 Model of the working principle of contact and separation mode TENGs.....	65
3.3 Modelling of surface tribo-charge transfer	72
3.3.1 Metal-Dielectric Mode	73
3.3.2 Dielectric-Dielectric Mode.....	75
3.4 Optimizing CS-TENG performance via a low permittivity substrate	77

3.4.1 Simulation and fabrication.....	78
3.4.2 Results and discussion.....	82
3.4.3 Application in a self-powered system by integration with a stretchable photodetector.....	85
3.5 Conclusions	87
<i>Chapter IV.....</i>	<i>89</i>
<i>Origin of the contact force-dependent response of triboelectric nanogenerators....</i>	<i>89</i>
4.1 Introduction	89
4.2 Fabrication and experiments.....	90
4.2.1 TENG fabrication and surface characterization.....	90
4.2.2 TENG Electrical measurements	91
4.2.3 TENG Contact area measurements.....	93
4.3 Results: electrical output and contact area	94
4.4 Implications and applications of pressure and area dependence.....	101
4.5 Conclusions	104
<i>Chapter V.....</i>	<i>107</i>
<i>Ferroelectric-Assisted High-Performance Triboelectric Nanogenerators based on Electrospun P(VDF-TrFE) Composite Nanofibers with Barium Titanate Nanofillers.....</i>	<i>107</i>
5.1 introduction.....	107
5.2 Experiments	108
5.2.1 Preparation of Materials	108
5.2.2 Electrospinning.....	110
5.2.3 Characterization and testing.....	112
5.2.4 Graphene supercapacitor	112
5.3. Result and Discussion	113
5.3.1 TENG performance	113
5.3.3 Ferroelectric-assisted TENG powered high performance self-charging system.....	128
5.4 Conclusions	132
<i>Chapter VI.....</i>	<i>134</i>
<i>A wide range self-powered flexible pressure sensor based on the triboelectric nanogenerator</i>	<i>134</i>
6.1 Introduction	134
6.2 Characterization of self-powered pressure sensor	135
6.3 Applications.....	137
6.3.1 Monitoring of human body movements	137
6.3.2 TENG as self-powered impact force sensor for falling objects	140
6.4 Conclusion	143

<i>Chapter VII.</i>	144
<i>Conclusion and future perspectives</i>	144
7.1 Conclusions	144
7.2 Future perspectives	147
<i>Appendix A: Surface Roughness Metrology</i>	149
<i>Appendix B: MATLAB code</i>	150
<i>References:</i>	151

List of figures

Fig. 2.1: Renewable energy harvesting including solar energy, wind power, hydropower, biomass energy and geothermal energy.....	23
Fig. 2.2: Working principles of micro/nano energy harvesting including pyroelectric nanogenerator, piezoelectric nanogenerator and triboelectric nanogenerator [44, 55, 56].	27
Fig. 2.3: Working principle of contact-mode triboelectric nanogenerators: (a) open circuit voltage (b) short circuit current.....	31
Fig. 2.4: Working principle of the four TENG modes of operation and their equivalent circuits [80, 90, 93, 102, 103].....	33
Fig. 2.5: Studies on the effect of contact area in CS-TENGs [160, 171, 172]	47
Fig. 2.6: A variety of applications of TENG based self-powered sensors, including: (a) self-powered velocity and trajectory tracking sensors (VTTS), (b) self-powered velocity dual-mode sensor, (c) self-powered acceleration sensor, (d) a wide range self-powered pressure sensor, (e) self-powered water wave sensor and (f) health monitor [47, 208-216].....	57
Fig. 2.7: Types of TENG-supercapacitor-based self-charging systems (a) sandwich shape self-charging power unit (SCPU), (b) output comparison of one TENG based SCPU and two TENG based SCPU (c) self-charging screen printed micro-supercapacitor power unit and (d) biodegradable SCPU [219-221].	59
Fig. 3.1: Schematic of the CS-TENG used for numerical study by (a) 2D (b) 3D version [42].	67
Fig. 3.2: Output performance with separation distance (a) open circuit voltage (b) output charge density and (c) short circuit current density.	68
Fig. 3.3: The simulation results of (a) open circuit voltage (b) short circuit current density and (c) output charge density. The effects for the output performances with thickness of PDMS (d) open circuit voltage, (e) output charge density and (f) short circuit current density.....	69
Fig. 3.4: (a) Schematic and device structure information of a metal-dielectric mode CS-TENG and (b) the energy band diagram for surface tribo-charge transfer at before contact and after contact status. ...	74
Fig. 3.5: (a) Schematic and device structure information for a dielectric-dielectric mode CS-TENG and (b) the energy band diagram for surface tribo-charge transfer at before contact and after contact status.	76

Fig. 3.6. Fabrication steps for the ‘top tribo-layer’ [42].	81
Fig. 3.7. Schematic of equivalent circuit for open circuit voltage measurements [49].	81
Fig. 3.8: Simulation results: (a) Open circuit voltage vs separation distance with 5cm×5cm areas and 200µm thickness substrate, (b) Open circuit voltage vs separation distance with 2cm×2cm areas and 100µm thickness substrate, (c) Short circuit charge density vs time, and (d) Short circuit current density vs time with substrate materials having a range of permittivity values (at 1mm separation distance for c and d), (e)–(f) Open circuit voltage, short circuit current density and short circuit charge density versus relative permittivity for different substrate materials (at 1mm separation) [42].	84
Fig. 3.9: Comparison of open circuit voltage signals for the devices with PTFE and PET substrates [42].	85
Fig. 3.10: Bending stability test for TENG devices: (a) Optical image while convex bending, (b) Optical image while concave bending [50].	86
Fig. 3.11: (a) Equivalent circuit for TENG-PD based self-powered system, (b) Integration of stretchable PD with TENG: Output voltage of TENG at different frequency across PD irradiated with and without UV light and their respective responsivity at generated voltage. Photographic demo showing the connection of LED in series with self-powered photodetector for real-time UV detection [50]. (Courtesy: the photodetector was designed and fabricated by Dr. Yogeenth Kumaresan).	87
Fig. 4.1. Schematic of the contact separation mode TENG having copper (Cu) in contact with polyethylene terephthalate (PET) [152].	91
Fig. 4.2. TENG surface topography (a) Cu foil and (b) PET film. Note: the z-axis is in micrometers for Cu and nanometer for PET due to the roughness difference [152].	92
Fig. 4.3. TENG self-aligning test setup: (a) Photo of test rig in mechanical test machine and (b) Sectional view of the test rig. The numbered parts are (1) TENG device (Cu and PET), (2) Glass plates, (3) Upper rig platform, (4) Lower rig platform, (5) Spherical bearing ball and (6) Locking screws [152].	93
Fig. 4.4: Schematic of equivalent circuit for (a) open circuit voltage measurements, and (b) short circuit current measurements [152].	94
Fig. 4.5: Real contact area measurement using pressure sensitive film: (a) Pressure sensitive film sandwiched between tribo-layers, (b) Compression of layers under contact force, (c) Pressure sensitive film operation and (d) Sample tested film showing areas of contact in red/pink [152].	95
Fig. 4.6. (a) Sample of TENG open circuit voltage signals for increasing contact force and (b) Peak open	

circuit voltage and peak short circuit current versus nominal contact pressure (and force) [152]. 96

Fig. 4.7: (a) Real contact area as detected by pressure sensitive film with increasing contact pressure showing as-scanned film with pink indicating solid contact (left) and binarized image with white indicating solid contact (right) and (b) Contact area ratio (A_r/A_n) versus nominal contact pressure (and force). Note: the nominal contact patch size in (a) is $2.5\text{ cm} \times 2.5\text{ cm}$ [152]. 97

Fig. 4.8: (a) Open circuit voltage and contact area ratio (A_r/A_n) versus nominal contact pressure and (b) Short circuit current and contact area ratio (A_r/A_n) versus nominal contact pressure. The blue hatched regions represent the pressure range in previous literature (as depicted in Table 4.2) [152]. 101

Fig. 4.9: (a) LED array performance versus nominal contact pressure and force (and contact area ratio) and (b) representative energy harvesting circuit. The LED array represents the word “BEST” – the LEDs become progressively brighter as the contact pressure (and contact area) is increased [152]. 102

Fig. 4.10: Overall view of the relationship between CS-TENG output and contact pressure [152]. 107

Fig. 5.1: Fabrication procedures for (a) P(VDF-TrFE), (b) P(VDF-TrFE)/CBTO and (c) P(VDF-TrFE)/TBTO NF mats by electrospinning [49]. 110

Figure 0.2 Fig. 5.2: TENG performance versus wt% of TBTO fillers in the tribo-negative P(VDF-TrFE)/TBTO layer showing (a) open circuit voltage and (b) short circuit current density [49]. 111

Fig. 5.3: indicates the purely piezoelectric output when a piezoelectric nanogenerators is fabricated for the PVDF-TrFE/TBTO case [49]. 112

Fig. 5.4: (a) Schematic of equivalent piezoelectric nanogenerator (i.e. piezo only) by PVDF-TrFE/TBTO NFs, (b) output voltage signal with varying applied contact forces and (b) output voltage with varying operation frequencies [49]. 113

Figure 0.1 Fig. 5.5: Characterization of device performance. (a-c) illustrate Fe-TENG device structure having negative tribo-surface as: (a) P(VDF-TrFE), (b) P(VDF-TrFE)/CBTO and (c) P(VDF-TrFE)/TBTO (with PET at the positive tribo-layer in each case). (a-c) also illustrate the role of ferroelectric polarization in affecting the triboelectric surface potential and charge density by indicating how the bias of the bound charges and the level of tribocharges increases as we move to P(VDF-TrFE)/TBTO (Note: X_C is degree of crystallinity & σ_T is tribocharge density). Electrical output is characterized in (d-i) for each of the three device types as follows: (d) open circuit voltage, (e) short circuit current density, (f) output power density and (g-i) output current and voltage versus resistive load for (g) pristine P(VDF-TrFE) & PET, (h) P(VDF-TrFE)/CBTO & PET and (i) P(VDF-TrFE)/TBTO &

PET. Contact pressure was fixed at 12.8 kPa. (j) transferred charge for three devices. (k) the stability of P(VDF-TrFE)/TBTO & PET device [49]...... 117

Fig. 5.6: Comparison of output voltage for the device with (a) PVDF-TrFE and (b) PVDF-TrFE/TBTO by non-poling, poling and electrospinning processes [49]...... 119

Figure 0.3Fig. 5.7: Materials characterization for P(VDF-TrFE) and P(VDF-TrFE)/BTO: (a) X-ray diffraction (XRD) results of P(VDF-TrFE) (red line), P(VDF-TrFE)/CBTO (black line) and P(VDF-TrFE)/TBTO (blue line) with crystalline β -phase (110/200) and XRD patterns of the cubic and tetragonal BTO nanoparticles (001/100); (b) as-measured dielectric properties of the nano-fibrous mats for: P(VDF-TrFE), P(VDF-TrFE)/CBTO, and P(VDF-TrFE)/ TBTO..... 121

Figure 0.4Fig. 5.8: COMSOL simulated potential distributions for PVDF-TrFE (left), PVDF-TrFE/CBTO (middle) and PVDF-TrFE/TBTO (right) devices. Surface potential is clearly highest for the TBTO case [49]. 124

Fig. 5.9: (a) Overlapped electron cloud (OEC) model of electron transfer between interface pairs for (a) P(VDF-TrFE) & PET, (b) P(VDF-TrFE)/CBTO & PET and (c) P(VDF-TrFE)/TBTO & PET [49].... 126

Fig. 5.10: Open circuit voltage versus nominal contact pressure [49]. 128

Fig. 5.11: Surface topography and contact analysis: surface height contour plots of (a) P(VDF-TrFE), (b) P(VDF-TrFE)/CBTO and (c) P(VDF-TrFE)/TBTO. SEM images of nanofiber surfaces for (d) P(VDF-TrFE), (e) P(VDF-TrFE)/CBTO and (f) P(VDF-TrFE)/TBTO (inset images at higher magnification). BEM prediction of real contact area (in black) for: (g) P(VDF-TrFE) & PET, (h) P(VDF-TrFE)/CBTO & PET and (i) P(VDF-TrFE)/TBTO & PET. Note how the predicted contact area follows the peaks of the fibers in the fiber orientation [49]...... 129

Fig. 5.12. (a) Schematic of graphene electrode based flexible supercapacitor (SC), (b) energy harvesting circuit for self-charging system (i.e. integration with the Fe-TENGs), (c) charging and discharging voltage of SC at different contact forces (frequency of 8Hz), (d) the maximum value of voltage charge into the SC versus nominal contact pressure, (e) charging and discharging voltage of SC by different frequencies (contact pressure 12.8 kPa), (f) the maximum value of voltage charge into the SC versus vibration frequencies, (g) representative energy harvesting circuit of Fe-TENGs for lighting LEDs and (h) photograph of lighted LED array representing the word “BEST” [49]. 132

Fig. 6.1: Characterization of TENG based self-powered pressure sensor and its potential applications: (a) working principles of a CS-TENG, (b) a sample of TENG Voc signal under the contact pressure of

1176kPa (735N). (c-e) Voltage output of TENG based self-powered pressure sensor for: (c) low, (d) medium-high pressure and (e) Super high-pressure ranges [27]. 139

Fig. 6.2: Voltage signal of the pressure sensing TENG when pressed using different numbers of fingers. 140

Fig. 6.3: Gait information from a man of 80kg weight collected by the pressure sensing TENG (a) walking, (b) jogging, (c) running and (d) jumping..... 141

Fig. 6.4: Gait information from a woman of 45kg weight collected by the pressure sensing TENG (a) walking, (b) jogging, (c) running and (d) jumping..... 142

Fig. 6.5: (a) Schematic of free-falling object onto TENG impact sensor from different heights of 5cm, 10.5cm, 13cm, 14cm; (b) output voltage peaks of TENG impact sensor showing the consecutive rebounding of the object from different heights shown in (a); (c) represents the results of output voltage against heights; (d) depicts impact velocity versus fall height and (e) shows the results for impact force against heights. 145

List of tables

Table. 2.1: Comparisons of output performances for energy harvesters [45, 52].	26
Table. 2.2: Triboelectric series for common materials following a tendency to lose electrons (positive) to gain of electrons (negative) [12].	40
Table 2.3: Literature comparison of TENG factors and parameters effecting electrical output.	47
Table 2.4: Typical PVDF based TENG performances compared with the present work (final row).	56
Table 3.1. Summary table of the key theoretical formulas describing CS-TENG operation.	74
Table 3.2. Parameters for ‘top tribo-layer’.	81
Table 3.3. Substrate relative material permittivity ϵ_r , ‘top tribo-layer’ relative equivalent permittivities $\epsilon(r,eq)$ and ‘top tribo-layer’ absolute equivalent permittivities ϵ_{eq} .	81
Table 3.4: Comparison of fabricated TENG devices and test parameters.	82
Table 4.1: Areal surface topography parameters of TENG tribo-contact surfaces (see Appendix A for information on parameters used).	94
Table 4.2: Typical nominal contact pressures (force/area) used in TENG studies compared with the present work (final row).	101
Table 4.3: Typical contact pressures available in possible high load applications for TENGs.	105
Table 5.1: Areal root mean square surface roughness of the tribo-contact surfaces and predicted contact area percentage (BEM) of the Fe-TENGs tribo-contact pair.	132
Table 5.2: Typical charging performance and charging period for TENG based self-charging systems in the literature as compared with the present work (final row).	136
No table of figures entries found.	

List of publications and awards

Journal papers:

1. G. Min, L. Manjakkal, D. Mulvihill and R. Dahiya, Triboelectric Nanogenerator with Enhanced Performance via an Optimized Low Permittivity Substrate, *IEEE Sensors Journal*, (20) 6856 – 6862, 2020. (DOI: 10.1109/JSEN.2019.2938605)
2. G. Min, Y. Xu, P. Cochran, N. Gadegaard, D.M. Mulvihill, R. Dahiya, Origin of the Contact Force- Dependent Response of Triboelectric Nanogenerators, *Nano Energy*, (83) 105829, 2021. (DOI: 10.1016/j.nanoen.2021.105829)
3. G. Min, A. Pullanchiyodan, A. S. Dahiya, E.S. Hosseini, Y. Xu, D.M. Mulvihill and R. Dahiya, Ferroelectric-Assisted High-Performance Triboelectric Nanogenerators based on Electrospun P(VDF- TrFE) Composite Nanofibers with Barium Titanate Nanofillers, *Nano Energy*, (90) 106600, 2021. (DOI: doi:10.1016/j.nanoen.2021.106600).
4. Y. Xu, G. Min, N. Gadegaard, D. Mulvihill and R. Dahiya, A unified contact force-dependent model for triboelectric nanogenerators accounting for surface roughness, *Nano energy*, (76) 105067, 2020. (DOI: 10.1016/j.nanoen.2020.105067)
5. Y. Kumaresan, G. Min, A. S. Dahiya, A. Ejaz, D. Shakthivel and R. Dahiya, Kirigami and Mogul patterned Ultra-Stretchable High-Performance ZnO Nanowires based Photodetector, *Advanced Materials Technologies*, 2100804, 2021 (DOI: 10.1002/admt.202100804).
6. Guanbo Min, Gaurav Kandelwal, Abhishek Singh Dahiya, Radu Chirila, Daniel M. Mulvihill and Ravinder Dahiya, “A wide range self-powered flexible pressure sensor based on triboelectric nanogenerator.” (Under review, IEEE Sensors Journal)

Conference paper:

1. G. Min, L. Manjakkal, D. M. Mulvihill and R. Dahiya, “Enhanced triboelectric nanogenerator performance via an optimised low permittivity, low thickness substrate,” *IEEE Sensors conference*, N. Delhi, India, Oct 2018.
2. G. Min, A. Dahiya, D. M. Mulvihill and R. Dahiya, “A wide range self-powered flexible pressure sensor based on triboelectric nanogenerator” *the IEEE Int. Conf on Flexible and Printable Sensors and Systems (FLEPS 2021)*, Manchester, UK, June 2021.

Awards:

1. Finalist (Top 4) at British Society for Strain Measurement (BSSM), 2021 Young Stress Analyst Competition.
2. Top 5% paper award at IEEE Sensors 2018 Conference (N. Delhi, India).

Acknowledgements

I would like to express my utmost gratitude and thanks to my supervisors Dr. Daniel Mulvihill and Prof. Ravinder Dahiya for their continuous support through my PhD. I appreciate the trust and freedom they gave me to explore my own research interests, without which this research would never have been possible. Further, I am grateful for the excellent service from the electronics and mechanical workshop and the James Watt Nanofabrication Centre (JWNC) staff.

I want to extend my sincere thanks to all the members of Bendable Electronics and Sensing Technologies (BEST) group and Materials and Manufacturing Research Group (MMRG). I particularly thank Dr. Libu Manjakkal, Prof. Yang Xu, Dr. Abhishek Dahiya, Dr. Abhilash Pullanchiyodan, Dr. Gaurav Khandelwal, Dr. Ensieh Seyed Hosseini and Mr. Radu Chirila who were closely associated in shaping some key outcomes of the research presented in this thesis and the associated publications. Also, I would like to thank Dr. Yogeenth Kumaresan, Dr. Saoirse Dervin, Dr. Bhavani Yalagala and Mr. Adamos Christou who supported me during the work.

Finally, I would like to express my deepest gratitude to my parents (Mr. Qinggang Min and Ms. Ling Li) for their unconditional sponsorship, love and support. Especially, thanks for your encouragement, when I was down, alone and sad. Thank you for your love and for your complete faith in me; this success would not be possible without you.

Author's declaration

I declare that, except where explicit reference is made to the contribution of others, this thesis is the result of my own work and has not been submitted for any other degree at the University of Glasgow or any other institution.

Guanbo Min

Glossary of abbreviations

TENG	Triboelectric nanogenerator
CS-TENG	Contact and separation mode triboelectric nanogenerator
LS-TENG	Lateral sliding mode triboelectric nanogenerator
SE-TENG	Single electrode contact mode triboelectric nanogenerator
CF-TENG	Contact freestanding tribo-layer mode triboelectric nanogenerator
T-TENG	Textile triboelectric nanogenerator
V_{oc}	Open circuit voltage
I_{sc}	Short circuit current
Q_{sc}	Short circuit output charge
J_{sc}	Short circuit current density
A_r	Real contact area
σ_T	Tribo-charges density
σ_U	Free charge density
C	Capacitance
x(t)	Separation distance
d	Thickness
E_z	Electric field
ϵ	Permittivity
ϵ_0	Permittivity of air
ϵ_r	Relative permittivity
A_n	Norminal contact area
TE	Triboelectric effect
FE	Ferroelectric effect
PTFE	Polytetrafluoroethylene
PDMS	Polydimethylsiloxane
PVDF	Polyvinylidene fluoride
P(VDF-TrFE)	Poly(vinylidene fluoride-trifluoroethylene)
TBTO	Tetragonal Barium titanate
PET	Polyethylene terephthalate
PMMA	Poly(methyl methacrylate)
PI	Kapton

Chapter I.

Introduction

1.1 Motivation

Since energy is the basis for human beings to accomplish their daily activities (e.g., powering electronics and commercial activity), its generation and impact on the environment has become the pre-eminent issue around the world. However, as consumption of non-renewable energy (i.e., petroleum, coal, etc.) is increasing exponentially, a world energy crisis is approaching progressively and restricting economic development [1]. Reportedly, it is roughly estimated that the reserves of coal and uranium will be exhausted by the mid-21st century and within 170 years [1-3]. The reserves of petroleum and natural gas are approximately 1.3k hundred million tons and 140 kMcm³ worldwide, respectively [4, 5]. Petroleum is expected to be exploited exhaustively until 2055 with an exploitation speed of 30 hundred million tons per year, and natural gas also can only be used for a further 50 years, with a consumption speed of 2.5 kMcm³/year. Because of the high consumption and the limited reserves of the raw material, it is a tremendous challenge for humanity to acquire innovational energy sources for the future. Indeed, the development of such an energy source can enhance the development of a country, placing it in a better international position with accompanying influence. Developing a renewable energy source requires significant pioneering work. Note that an innovational energy source, which has the characteristic of low pollution and high energy storage, means energy without the traditional dependency on fossil fuels. This development of renewable energy can respond to the challenge of resource exhaustion and environmental pollution [6].

Additionally, exploiting and employing microdevices and micro-electromechanical systems (MEMS) is one of the methods to settle the challenge of resource exhaustion, because of their low power consumption [7-10]. The external power suppliers (e.g., lithium batteries and supercapacitors) are necessary for these microdevices and MEMS to provide continuous electrical energy supply. Simultaneously, these external power suppliers increase the limitation of the energy storage and environmental pollution [11].

In order to figure out the energy requirements, nanogenerators were suggested to convert ambient energy into electricity. Because of the separate positive and negative charges, the differential potential can drive induced charges as the oriented current to power the applications [12-15]. Most of the nanogenerators depend on properties such as pyroelectricity, piezoelectricity and triboelectricity [13, 16-19]. Therein, triboelectrification and electrostatics are part of our daily lives – think for example of the charging of cloths when rubbed over hair. Generally, triboelectrification is often regarded as a negative effect, for example, factory dust explosions, separation between medicine and powders, etc. Additionally, triboelectrification has often been ignored by researchers, as triboelectricity was difficult to harvest and utilise. The advent of triboelectric nanogenerators (TENGs) changed the stereotype of the negative effect of triboelectrification, due to its high energy conversion efficiency for converting ambient mechanical energy to electricity (the maximum conversion efficiency can be 85%) [12].

Triboelectric energy harvesting depends on converting ambient random mechanical energy to electricity, and it can reduce the amount of energy waste. Depending on this definition, TENGs are fabricated by two types of flexible materials with large differences in the triboelectric properties such as the interface pair [12, 13]. Due to the rubbing or contact and separation of the contacting tribo-material surfaces, tribo-charges are generated on the interface surfaces. Because of electrostatic induction and polarization, applications can be powered by free charges which are induced on the two sides of the electrodes. Using TENGs, the mechanical energy from daily life can be transformed efficiently, including vibration, human motion, ocean wave, wind power, etc [20-23]. Moreover, TENGs can also be applied as self-powered sensors and into self-charging systems, to increase their coefficient of utilization [24, 25]. Especially, this can be a response to the challenge of a 24-hour power supply. These results demonstrate that this technology can be valuable in wearable applications, where higher power output, more efficient charging and flexibility are paramount.

1.2 Research objectives

The main objective of this work was to understand, design and characterize high performance flexible TENGs and their applications in self-powered/charging systems.

The detailed major objectives are:

1. To understand the principle of contact and separation mode triboelectric nanogenerators (CS-TENGs) by MATLAB simulation to summarize the effect of parameters for optimisation of device performance.
2. To characterize the electrical output of TENGs and the effect of real contact area (A_r) at the tribo-contact interface.
3. To understand the origin of the contact force-dependent response of CS-TENGs.
4. To investigate the properties of TENG contact materials that can improve surface tribo-charge generation.
5. To understand the principle of optimizing the performance of the tribo-material by electrospinning and fabricating a high-performance tribo-layer by electrospinning.
6. To design a CS-TENG as a self-powered sensor and integrate a high-performance TENG with a supercapacitor to develop as a wearable self-charging system.

1.3 Key contributions of this thesis

The key contributions of this thesis can be summarized as follows:

- A simulation study was presented to investigate the effects of varying substrate relative permittivity upon TENG outputs such as open circuit voltage, short circuit current density and transferred charge density. In addition to further in-depth simulation, two fabricated devices with polyethylene (PET) and polytetrafluoroethylene (PTFE) substrates also were tested to verify the simulation results.
- The work is the first-time both real contact area and electrical output have been measured simultaneously between two nominally flat surfaces during the operation of a TENG device.

- The origin of the contact force-dependent response of TENGs is shown to result from the contact force dependence of the real contact area (A_r), as governed by the unavoidable presence of surface roughness. The open circuit voltage V_{oc} , short circuit current I_{sc} and A_r for a TENG, having two nominally flat tribo-contact surfaces, were found to increase with contact force/pressure. The A_r was notably small at low pressures (0.25% at 16 kPa) that are typically experienced in wearable applications. However, it increased 328-fold to as much as 82% when it saturated beyond about 1.12 MPa pressure - achievable for impact with ocean waves. Critically, V_{oc} and I_{sc} saturate at the same contact pressure as A_r suggesting that electrical output follows the evolution of the A_r as governed by the surface topography.
- This thesis also presents high-performance ferroelectric-assisted TENGs using electrospun fibrous surfaces based on P(VDF-TrFE) with dispersed BaTiO₃ (BTO) nanofillers in either cubic (CBTO) or tetragonal (TBTO) form. The results shown were that BTO fillers boost output, not just by increasing permittivity, but also by enhancing the crystallinity and amount of the β -phase (as TBTO produced a more crystalline β -phase present in greater amounts).
- The ferroelectric-assisted TENG was integrated with a flexible graphene electrode-based supercapacitor to produce a self-charging system capable of charging to 1.25 V in just 5 min.
- A CS-TENG was designed as a wide-range, self-powered flexible pressure sensor. The fabricated TENG can detect a wide range of applied pressures from 3.2 to 1176 kPa. The sensor sensitivities in three pressure regimes, namely low (1-10 kPa), medium-high (10-500 kPa) and ultra-high (>500 kPa) were extracted as 3.16, 0.023 and 0.031 V/kPa, respectively.
- A wide range pressure sensor has been demonstrated showing how the sensor can be used to detect finger tapping, collect user gait information and detect impact forces.

1.4 Structure of the thesis

Following the introduction, this thesis is organised as follows:

- **Chapter II** introduces an overview of triboelectric nanogenerators (TENGs) with emphasis on the recent progress on contact and separation mode triboelectric nanogenerators (CS-TENGs). In particular, the power generation mechanisms, working principles of the four TENG modes and different tribo-materials that have been used along with their properties and their performances. In addition, the key parameters, which can optimize TENG performance have been highlighted. Simultaneously, the thesis determines a rank order of the sensitivity of CS-TENG output to the different parameters. Finally, because of the results of the comparisons, three aspects have been afforded particular focus: increasing contact area between the interface pair, enhancing the crystallinity of the contact materials and TENG applications in self-powered sensors and self-charging systems.
- **Chapter III** presents the formulation and model validation through electrical characterization of CS-TENGs. Firstly, the progress of CS-TENG models based on device structure is introduced such as parallel-plate capacitor mode, distance-dependent electric field model and Load-dependent model in the first part of this chapter. After that, a numerical study on tribo-charge generation behaviors has been analyzed by the energy bands between the interface pair materials. Finally, a study on optimizing CS-TENG performance via a low permittivity substrate by both the simulations and experiments is carried out.
- **Chapter IV** describes experiments that uncover the origin of the contact force-dependent response of TENGs. Their performance is believed to depend on the contact force, but its origin had not yet been established. Herein, we show that the contact force-dependent electrical response is due to the contact force-dependent real contact area that results from the inevitable presence of surface roughness on the tribo-contact surfaces.
- **Chapter V** develops high-performance ferroelectric-assisted TENGs using electrospun fibrous surfaces based on P(VDF-TrFE) with dispersed BaTiO₃ (BTO)

nanofillers in either cubic (CBTO) or tetragonal (TBTO) form. TENGs with three types of tribo-negative surface (pristine P(VDF-TrFE), P(VDF-TrFE)/CBTO and P(VDF-TrFE)/TBTO) in contact with PET were investigated. Essentially, tribo-charge transfer is boosted due to increased surface potential owing to enhanced ferroelectric polarization induced during electrospinning. P(VDF-TrFE)/TBTO produced higher output than P(VDF-TrFE)/CBTO even though permittivity is nearly identical. Thus, it is shown that BTO fillers boost output, not just by increasing permittivity, but also by enhancing the crystallinity and amount of the β -phase (as TBTO produced a more crystalline β -phase present in greater amounts).

- **Chapter VI** presents a triboelectric nanogenerator (TENG) based wide-range, self-powered flexible pressure sensor. The fabricated TENG can detect a wide range of applied pressures from 3.2 to 1176 kPa. The sensor sensitivities in three pressure regimes, namely low (1-10 kPa), medium-high (10-500 kPa) and ultra-high (>500 kPa) were extracted as 3.16, 0.023 and 0.031 V/kPa, respectively. Stable and repeatable TENG responses were achieved for all three pressure regimes and this is due to how the real contact area at the TENG interface varies reliably with contact pressure. To the best of our knowledge, this is the first time a TENG as a self-powered pressure sensor has been characterized over such a wide pressure range (that includes higher pressures). These results highlight the potential for TENGs as pressure sensors in a wide range of applications such as: detecting pressure in wearables, self-powered e-Skin for the sole of humanoid robots to help them walk and stand, and for detecting impact forces with water waves.
- **Chapter VII** summarizes the contribution of this research on tribo-materials design, CS-TENG fabrication and characterization of high-performance CS-TENG based self-powered sensor/ system and self-charging system. It also provides suggestions for future work.

Chapter II.

Literature Review

2.1 New energy resources

2.1.1. Renewable energy

The utilization of energy was one of the major drivers of social economic development and increasing standard of living. Wind power, water wave power, firewood and animal power were the major applied power sources for a classical civilization [26-29]. After the industrial revolution, fossil fuels gradually became the dominant energy source around the world [30]. With the consumption of fossil fuels, renewable energy sources are being explored and developed promptly. However, non-fossil and renewable energy sources still only cover 20% of the total energy utilization [6]. With energy requirements growing and the non-renewable traditional energy sources exhausting, an energy crisis is approaching, even threatening human life. It is estimated that only one person out of four can survive into the indefinite future (on average) with this speed of energy consumption. Therefore, renewable energy sources have been suggested as a response to these energy challenges, because of their high efficiency, cleanliness, diversification and globalization.

Additionally, the traditional energy source (e.g., fossil fuel) is falling out of fashion due to its many harmful effects. Compared with the traditional energy sources, renewable energy is clean, it can reduce the greenhouse effect and it reduces the problem of resource shortage and dust pollution [3]. There are nine current renewable energy sources that satisfy these conditions, including solar energy, geothermal energy, wind power, hydrogen energy, biomass energy, nuclear energy, nuclear fusion energy, tidal energy and natural gas hydrate (NGH) [16, 26, 31-37]. The advantages of renewable energy technologies are: (1) they are an underdeveloped resource with high potential, (2) there are abundant reserves widely spread geographically, (3) they are environmentally friendly and (4), the wind power, geothermal energy and solar energy can be a bottomless supply. In short, renewable energy has more advantages than the traditional energy sources and application spaces. Currently, solar energy, geothermal

energy, tidal energy, wind power and biomass energy are being applied extensively and have a highly developing prospect. They are explained further here (A to E):

- A . Solar energy is one of the most well known renewable energy sources globally, owing to its advantages of being clean, environmentally friendly and sustainable etc. It depends on converting solar radiation energy to electricity. Notably, the average solar radiation energy per hour can supply the energy to use for a year for all humans sufficiently, which is approximately 430 quintillion joules [16]. However, solar cells have the disadvantage of energy interruption due to the environmental limit [38]. For example, solar energy is only outstandingly adequate in the sunny daytime and summer season, irrespective of the geographical location.
- B . Wind power generation is the second largest source among the renewable energy sources. The mechanical energy from wind can be collected by turbines to drive generators which then transfer electricity into the national grid. Reportedly, more than 5% of global electricity was from wind power production in 2018 with 591 GW of global capacity [26]. Nonetheless, wind power generation is not suitable for every property due to its high noise, threatening presence to wildlife, unpredictable wind intensity and location limitations. Hydropower is the largest renewable energy source for power generation.
- C . Similar to the wind power generation, hydropower generates electricity by the flow of water to drive a turbine. Because of the barrier placed in the water (the dam), the potential energy of the river can be controlled and also allow electrical power to be stored for use when demand reaches a peak [32]. Therefore, compared with the other renewable energy sources, hydropower is more reliable due to its stability and controllability [39]. Tidal energy is a variation of hydropower. However, its stability is lower than hydropower energy.
- D . Biomass energy is a sort of energy that is shaped by solar energy in the form of

chemical energy (i.e., renewable carbon source); it is because of photosynthesis [33]. Simultaneously, biomass includes a wide range of varieties such as plant, microorganism and the waste produced by the herbivores. There are 1,700 million tons of organisms produced by photosynthesis per year [33]. Simultaneously, the energy in these organisms is approximately 15 times the total energy consumption in the world. However, its coefficient of utilization is only 3%, although biomass is abundant [40]. Additionally, the cost of biomass power generation is uncompetitive, and its waste is harming the environment.

E . Power generation by geothermal energy depends on the temperature difference between the earth's surface heat and the heat below the earth's surface [31]. A geothermal heat pump is used to convert this heat difference to the electricity. A special application is ocean thermal energy, which depends on the temperature difference between the ocean surface and deep below the surface [41]. Comparing with fossil fuels, the heat (or electricity) can be extracted without burning. Simultaneously, geothermal energy can be used uninterruptedly, compared with solar energy and wind power. However, the release of H₂S is the main disadvantage of geothermal energy power generation.

Renewable energy is an important route of response to the energy crisis in the world. In 2020, there are 34% world electricity from renewable sources [42]. However, renewable energy sources still have weaknesses in their applications such as the energy interruption from the environmental limit, location limit, low conversion rate and technical difficulty. In addition, recent renewable energy is only replacing the original mega energy by a green route. It still requires a direct and repaid energy route for powering the micro/nanoelectronics/devices such as micro/nano-sensors, robotics, health monitoring and tribotronic transistors [43]. It is to be noted that these devices only need relatively low power (around 0.1–100 mW/m²). From the analysis in the previous section, it can be seen that the method for power generation of renewable energy involves:

1. Collecting the heat from the energy source and converting it into electricity.
2. Transferring the renewable energy sources as the mechanical energy. After that, the mechanical energy can be converted to electricity (e.g., turbine).

However, their similarity is that a reasonable power terminal is adopted. Therefore, after determining the collected energy category, designing a power terminal (e.g., nanogenerators, solar cells, etc) is the key to micro/nano energy harvesting (see Table 2.1).

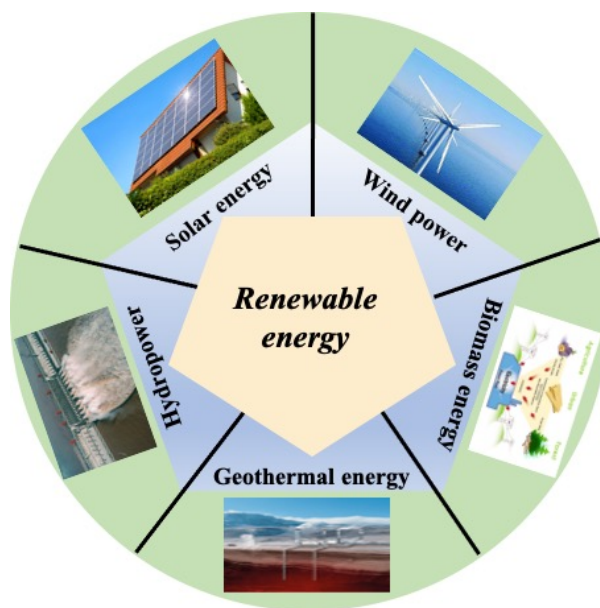


Fig. 2.1: Renewable energy harvesting including solar energy, wind power, hydropower, biomass energy and geothermal energy.

2.1.2. Micro/nano energy

The potential of renewable energy as the energy source for the large-scale power grid has been discussed in Section 2.1.1. Their characteristics include high energy reserves, high cost of power generation, large power terminal equipment and high output power. Moreover, nano-scale energy (i.e., milliwatt) harvesting is also a promising method to provide power for small electronics and nano/micro-systems, as it is sustainable and maintains free and self-powered operation [12, 14]. The application of renewable

energy in the aspect of nano energy is also developing increasingly with the progression of nanotechnology, including energy harvesting, energy conversion, energy storage and applications [14, 24, 44]. Nano energy technology also improves the utilization factor of renewable energy, as the random and waste energy in human life can also be utilized such as human motion, gentle breezes and rolling tires. Integrating these varieties of nano energies can also accumulate as high energy because nano energies also have high energy reserves.

Therefore, a number of nanogenerator concepts have been designed depending on how their materials properties might facilitate electricity generation. For instance, solar cells depend on solar radiation. Pyroelectric nanogenerators depend on the temperature sensing of materials [45, 46]. Piezoelectric nanogenerator and triboelectric nanogenerator, on the other hand, can convert mechanical energy [12, 47]. Nanogenerators are innovative self-powered devices that can directly transfer ambient energy to electricity. Nanogenerators can convert many variations of ambient energy to electricity, including wind, water flow and human motion [12]. Additionally, this promising technology has a wide range of applications. Firstly, nanogenerator-based sensors and sensor arrays can detect location, acceleration, pressure, temperature and humidity precisely [24]. For example, if we integrate nanogenerators into the slopes of Parkinson's disease, patients' gait information (e.g., normal walking, rapid walking or tumble) can be analysed effectively [48]. Because of its self-powered and highly sensitive characteristic, its prospect of application obtains positive responses. Simultaneously, it is also a beneficial power supplier for low power electronics such as self-powered systems. Nanogenerators have been demonstrated to power pH sensors, LED arrays and photodetector-based systems [49-51]. Finally, due to its high output power (perhaps up to $500\text{W}/\text{m}^2$), energy storage systems also can be charged by nanogenerators, such as supercapacitor and lithium batteries [50, 52]. Energy harvesting through various mechanisms such as triboelectric, piezoelectric and pyroelectric has been widely explored. These devices are discussed in this section.

Table. 2.1: Comparisons of output performances for energy harvesters [45, 52].

Energy harvesters	Voltage (V)	Current (μA)	Power density (mW/cm^2)	Efficiency (%)	Application
PyENG	0.01-190	0.0006-11	0-0.014	0.01-14.8	Geothermal energy and Solar energy
PENG	0.01-200	0.01-10	0.001–30	0.01-25	Wind power and hydropower
TENG	12-1500	10-2000	0.01-100	10-85	Wind power and hydropower

Pyroelectric nanogenerators (PyENGs) utilize pyroelectric material to convert ambient thermal energy to electricity. Regularly, thermoelectric energy harvesting relies on the Seebeck effect, where the heated electrons flow toward the cooler side of the device [46]. However, the environmental temperature distribution is spatially consistent rather than with a gradient. Thus, it is not able to use Seebeck effect to harvest thermal energy in the environment, as the temperature is changing with time. Owing to this behaviour, the PyENG is the most suitable selection for thermal energy harvesting. Because of the anisotropy of the solid material, the pyroelectric material will be self-polarized by the change of the temperature. A wearable PyENG, which was integrated on a N95 face mask, can generate a power density of $0.68\mu\text{W}/\text{cm}^2$ [45]. Additionally, there are also many potential applications for PyENGs such as self-powered temperature sensor, temperature imaging and medical monitoring and diagnosing.

The piezoelectric nanogenerator (PENG) is the first-generation mechanical energy harvester; it depends on the piezoelectric property of the material between two electrodes [47]. Generally, PENGs were fabricated as a sandwich structure. Since piezoelectric materials exhibit the phenomenon of self-polarization by external applied pressure, the free charges can be induced on the electrodes by the internal electric field (i.e., from the piezoelectric material self-polarization). After that, the free charges can be induced on two sides of the electrodes. Recently, there are many well-known piezoelectric (PE) materials that have been investigated for nanogenerators, including zinc oxide (ZnO), zirconate titanate (PZT), barium titanate (BaTiO_3) and polyvinylidene fluoride (PVDF), even the ferroelectric material as Poly(vinylidene fluoride-co-trifluoroethylene) (P[VDF-TrFE]) [53]. These materials with piezoelectric

property are so because of their specific atomic structure. For example, ZnO is a type of metallic oxide with a piezoelectric property, as the zinc atom and oxide oxygen atoms present non-symmetrical configuration in the ZnO molecule [47]. In addition, β -phase PVDF is piezoelectric due to the differences in electronegativity between the fluorine atom and the hydrogen atom [19]. The piezoelectric material is placed between two electrodes in a PENG device. After a mechanical pressure is applied to the piezoelectric material, the electric charges within piezoelectric crystal go ‘out of balance’ (i.e., self-polarization) [47]. Owing to the material self-polarization, an internal electric field is formed to induce the free charges on two sides of the electrodes. Because piezoelectricity is the process of using crystals to convert mechanical energy to electricity effectively, this principle is applied in a wide range of applications, including human motion monitoring, voice recording, self-powered active sensors for health care monitoring and electronic skins for discriminating static/dynamic pressure stimuli. However, its low output power density ($\sim 30\text{mW}/\text{cm}^2$) [54] is the largest limit for extending its applications, as depicted in Table 2.1.

The triboelectric nanogenerator (or TENG) is the second-generation mechanical energy harvester. Recently, a high performance record for CS-TENGs was $100\text{ W}/\text{m}^2$ output power density, which is over 3-fold higher than the average PENG output. Additionally, the conversion efficiency of a TENG can be higher than 85%, which is approximately 5 times that of a solar cell [12, 16]. For instance, a spherical TENG with 7 cm diameter has been fabricated to harvest water wave energy [55]. A single spherical TENG can generate a 10mW instantaneous output power at 10Kohm load. It is estimated that, if these types of TENG devices are installed onto a 1km^2 area on the sea surface (i.e., combining them as a TENG-based energy network), they could produce 27.6GWh of average output energy. This result envisages a blue energy dream based on TENGs, in which many TENG-based energy networks combined by cables can provide energy for a coastal town. This idea also demonstrates the possibility of compound nano/micro scale energy to be converted as mega/giga scale energy. Overall, these reasons also demonstrate that TENG technology can be more valuable in the applications of wearable, water wave energy and sensing technology, where high power, high transfer

efficiency and flexibility are paramount.

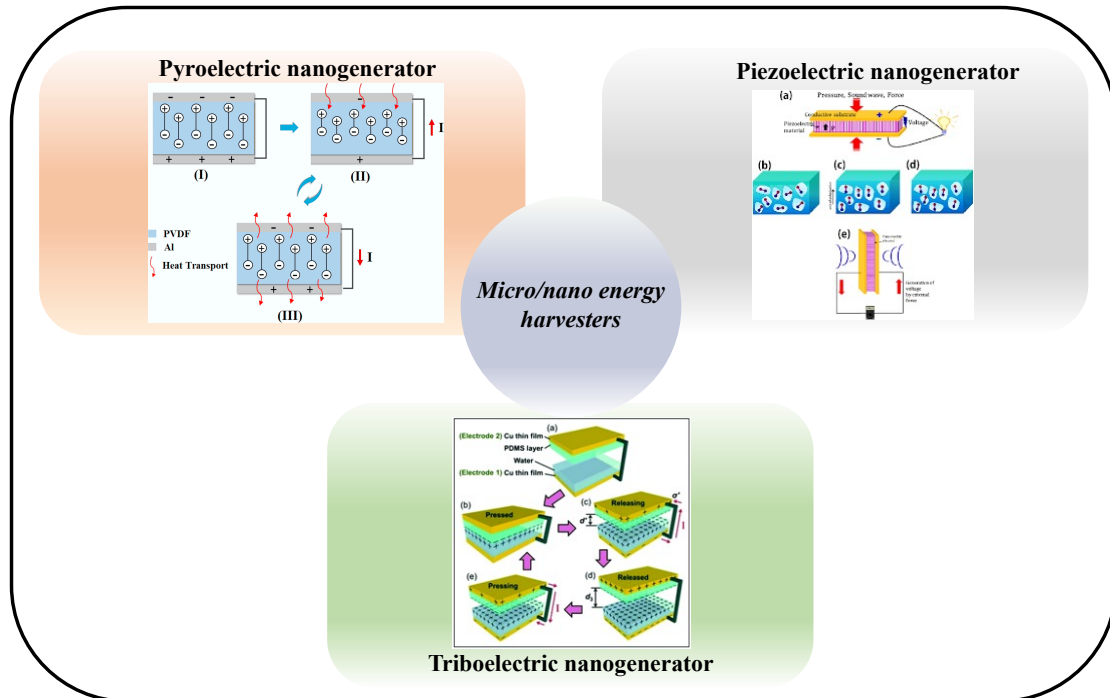


Fig. 2.2: Working principles of micro/nano energy harvesting including pyroelectric nanogenerator, piezoelectric nanogenerator and triboelectric nanogenerator [44, 55, 56].

2.2 Triboelectric nanogenerator

The key parameters that govern TENG performance are understanding in this section 2.2-2.3 and then explore ways to boost output in section 2.4.

2.2.1 Triboelectrification

Triboelectrification phenomenon are often considered as a negative effect in human life. For example, electrostatics usually influence the wireless network during the flight of a plane at high altitudes, interrupting the communication between the flight and ground service. In pharmaceutical preparation, tribo-charges attract dust and decrease medical purity. For electronics, the tribo-charges will breakdown the electronic element and IC to boost the device burn-in. Additionally, the electrostatic effect easily attracts dust on electronic surfaces such as TV and phone screens to reduce their resolution. In factories, tribo-charges result in fires with inflammable and explosive materials. Therefore, people usually avoid triboelectrification [56]; however, the triboelectric nanogenerator is one of the applications that has a positive effect via high efficiency power generation [12].

In the contact-separation triboelectric nanogenerator, it is the coupling of contact

electrification and electrostatic induction that defines the operating principle [12]. Therein, the generated tribo-charges are the power source that drives the TENGs to induce the free charges on the electrodes [12, 57-59]. The generation of tribo-charges depends on the contact electrification phenomenon between the contacting material interfaces [58]. Because of that, the transfer of opposite and equal tribo-charges occurs on each of the contact surfaces. The phenomenon of contact electrification and triboelectrification is widely experienced in daily life. For instance, after rubbing a plastic rod on a woollen sweater, it can be observed to attract paper scraps and hairs. Also, when people wear out their sweaters, they can sometimes hear the sound of a charge or even see an emerging electric spark. Tribo-charge generation by contact electrification or triboelectrification depends on the differences in the tribo-polarity between two tribo-materials [12]. Generally, when metal and dielectric or dielectric and dielectric are in contact, an output electrical signal can be detected [60]. During the friction between two metals, tribo-charges can also be generated; however, the charges would be lost promptly due to the metal's conductivity [60]. The tribo-charge generation is widely understood as the charge transfer between the contacting atom and molecule (or molecule and molecule) [12, 56, 60]. Note that the chain structure of a material surface is different to the chain structure of material bulk, in that there are dangling chains on a material surface [61, 62]. Furthermore, a temporary chemical bond is formed during contact, because of the differences in electron affinity [63]. In order to balance the differences in energy band (i.e. chemical potential) of the contacting atom and molecule (or molecule and molecule), the electrons can transfer from one material surface to the other. After the interface pair is separated, opposite and equal tribo-charges will be accumulated on the two sides of the interface.

2.2.2 Working principle of triboelectric nanogenerators

The reason why the triboelectrification phenomenon could be employed as a nanogenerator is because triboelectrification contains a vast energy reserve, and it is occurring in real time. In 1929, Van de Graaff's generator based on the triboelectrification principle was born, which can transfer electrostatic charges to the

metal ball surface through corona discharging [64, 65]. Simultaneously, two electrodes could be discharging, once the charge density reached the threshold value [65].

However, in 2012, the first TENG was reported by Zhonglin Wang's group in Georgia Tech [66]. When two tribo-materials contact each other by an external force, they generate opposite and equal tribo-charges on two contact surfaces due to their difference capability in gaining and losing electrons to produce the device internal voltage [12, 43, 57]. After connecting the applications with a TENG by the external wires, the induced free charges can be used for driving the electrons across the applications. Because the internal voltage is changing with the varying separation between the contact surfaces, the external voltage is also changing to balance the internal voltage. Because of the external voltage, the induced free charges flow to form the current in the circuit [67].

Herein, this thesis concentrates on the vertical contact-separation mode triboelectric nanogenerator (CS-TENG) as an example to explain its working principles at open circuit and short circuit conditions, respectively. The working steps applying to the open circuit voltage and short circuit current condition for a CS-TENG are shown schematically in Fig. 2.3. Here, we explain the working principle of a contact-separation TENG (CS-TENG) at open circuit and short circuit conditions step by step: The open circuit voltage and short circuit current are the significant parameters for presenting the performance of CS-TENGs [12, 57-59]. There is no free charge on the two electrodes for the open circuit configuration in Fig. 2.3(a) [12]. The open circuit voltage is created by the difference in potential between the electrodes as separation occurs. Simultaneously, these built-in electric fields cause the polarization of the dielectric material and produce the induced charges on the electrodes [58]. In the short circuit mode, after the tribo-charges have been generated on the contact surfaces, the tribo-layers are being polarized to form the bound charges inside of the tribo-layer materials. Because of the bound charges, there will be induced free charges on two sides of the electrodes. Neutralizing the negative charge on the bottom electrode, the positive charges on the top electrode will be conducted to the bottom electrode to form the short circuit current, as shown in Fig. 2.3(b).

Working principles of a CS-TENG is similar to the short circuit condition, when it connected to applications (e.g., electronics). However, due to connecting the application to an external circuit, there is a differential potential between two sides of applications. When the separation is increasing to the amplitude, the internal voltage of CS-TENG is also increasing, and the top induced free charge is pumped from top to bottom electrode to balance the internal different potential. Additionally, the output current from the CS-TENG could be flowing from positive polar to the negative polar of the application. However, when the separation is reducing from amplitude to zero, it is equivalent to adding an opposite voltage at two electrodes. For this reason, the electrons on the bottom electrode are driven back from bottom to the top electrode. Thus, owing to this periodic vibration by the external applied force, two interfaces are contacting and separating continuously, and the device is generating alternating current signal.

2.2.3 The modes of triboelectric nanogenerators

The working principle of the TENG has been introduced with reference to the CS-TENG, however, there are another three modes of TENG that have been invented to harvest different modes of vibration effectively, including sliding mode, freestanding mode and single electrode mode, as shown in Fig. 2.4 [68]. The theoretical module of TENGs depends on the parallel capacitor module and the concept of displacement current (i.e. Maxwell's law) [12, 69, 70]. Note that the current from the TENG corresponds to the varying of the internal electric field and the tribo-layer polarization [68]. However, the output voltage for different modes of TENGs related to the device total capacitance and total surface tribo-charges. Note, device total capacitance can be calculated by TENGs' equivalent circuit. We now focus in more detail on the individual modes.

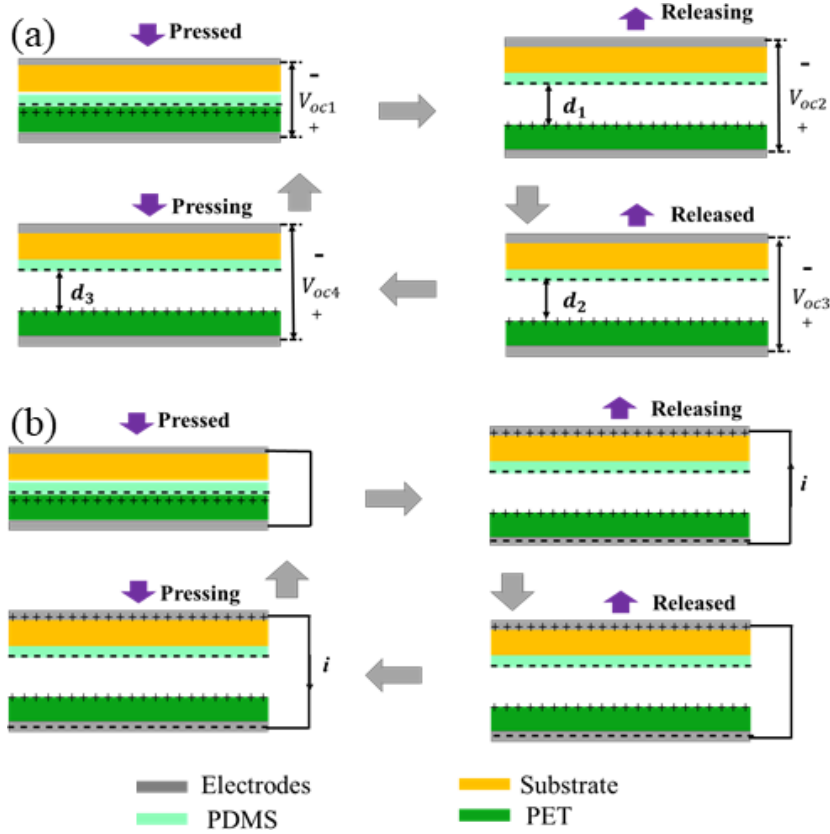


Fig. 2.3: Working principle of contact-mode triboelectric nanogenerators: (a) open circuit voltage (b) short circuit current.

i. Contact and separation mode triboelectric nanogenerator (CS-TENG)

Contact and separation triboelectric nanogenerators (CS-TENG) couple contact electrification and electrostatic induction [12, 57]. Fig 2.3 has already explained the working principles of a CS-TENG with an interface pair of PDMS and PET. After the tribo-charges are generated on the interfaces, the electric fields inside the TENG device are shown schematically in Fig. 2.4(a). The total electric field is equal to the sum of the electric fields inside of the tribo-layers and the air gap electric field [57]. If we assume that the transferred free charges quantity is Q in Fig 2.4(a), the output voltage could be calculated by the parallel capacitor module as [57]:

$$V_{out} = -\frac{Q}{S\epsilon_0} \left(\frac{d_1}{\epsilon_{r1}} + \frac{d_2}{\epsilon_{r2}} + x(t) \right) + \frac{\sigma_T x(t)}{\epsilon_0} \quad (2.1)$$

where, S is the nominal contact area, d_1 and d_2 are the thickness of tribo-layers, ϵ_{r1} and ϵ_{r2} are the relative permittivity of tribo-layer materials, ϵ_0 is the permittivity of air, $x(t)$ is the separation distance, $v(t)$ is the speed of vibration and σ_T is tribo-charge density.

Since Q is equal to zero at the open circuit condition, we have

$$V_{oc} = \frac{S\sigma_T}{C_{air}} = \frac{\sigma_T x(t)}{\epsilon_0} \quad (2.2)$$

Depending on the equivalent circuit of a CS-TENG in Fig. 2.4(a), the total capacitance of the device is deduced from:

$$\frac{1}{C_{total}} = \frac{1}{C_1} + \frac{1}{C_{air}} + \frac{1}{C_2} \quad (2.3)$$

Due to the $V_{out} = 0$ at short circuit condition,

$$Q_{sc} = \frac{S\sigma_T}{C_{air}C_{total}} = \frac{S\sigma_T x(t)}{d_0 + x(t)} \quad (2.4)$$

$$I_{sc} = \frac{dQ_{sc}}{dt} = \frac{S\sigma_T d_0 v(t)}{(d_0 + x(t))^2} \quad (2.5)$$

ii. Lateral sliding mode triboelectric nanogenerator

The working principle of a lateral sliding mode triboelectric nanogenerator (LS-TENG) has been shown schematically in Fig. 2.4(b), and it couples the triboelectrification (rubbing interfaces) with electrostatic induction. Comparing with the CS-TENGs, the interface pair presents relative displacement to replace the separation step to generate tribo-charges on the material sliding surfaces [71]. The working principle of a LS-TENG is still based on the parallel capacitor, as shown in Fig. 2.4(b).

However, it depends on altering the swept area of tribo-layers to form the output signals by the external applied force [72]. Increasing the swept area, both surface tribo-charges (Q) and horizontal electric fields of two tribo-layers are rising to form the output voltage between two side of electrodes, as shown in Fig. 2.4(b) [71, 72]. Therefore, the output voltage could be calculated by the parallel capacitor module as [71]:

$$V_{out} = -\frac{Q}{w(l-x(t))\epsilon_0} \left(\frac{d_1}{\epsilon_{r1}} + \frac{d_2}{\epsilon_{r2}} \right) + \frac{\sigma_T x(t)}{(l-x(t))\epsilon_0} \left(\frac{d_1}{\epsilon_{r1}} + \frac{d_2}{\epsilon_{r2}} \right) \quad (2.6)$$

where, w and l are the width and length of tribo-layer, $x(t)$ is the horizontal relative displacement, d_1 and d_2 are the thickness of tribo-layers, ϵ_{r1} and ϵ_{r2} are the relative permittivity of tribo-layer materials, ϵ_0 is the permittivity of air, $v(t)$ is the speed of rubbing and σ_T is tribo-charges density. The total capacitance of the device can be calculated from:

$$\frac{1}{C_{total}} = \frac{1}{C_1} + \frac{1}{C_2} = \frac{\epsilon_0 w(l-x(t))}{\frac{d_1}{\epsilon_{r1}} + \frac{d_2}{\epsilon_{r2}}} \quad (2.7)$$

If it is at short circuit condition ($V_{out} = 0$),

$$Q_{SC} = \sigma_T w x(t) \quad (2.8)$$

$$V_{oc} = \frac{\sigma_T x(t)}{(l-x(t))\epsilon_0} \left(\frac{d_1}{\epsilon_{r1}} + \frac{d_2}{\epsilon_{r2}} \right) = \frac{Q_{SC}}{C_{total}} \quad (2.9)$$

$$I_{sc} = \frac{dQ_{sc}}{dt} = \sigma_T w v(t) \quad (2.10)$$

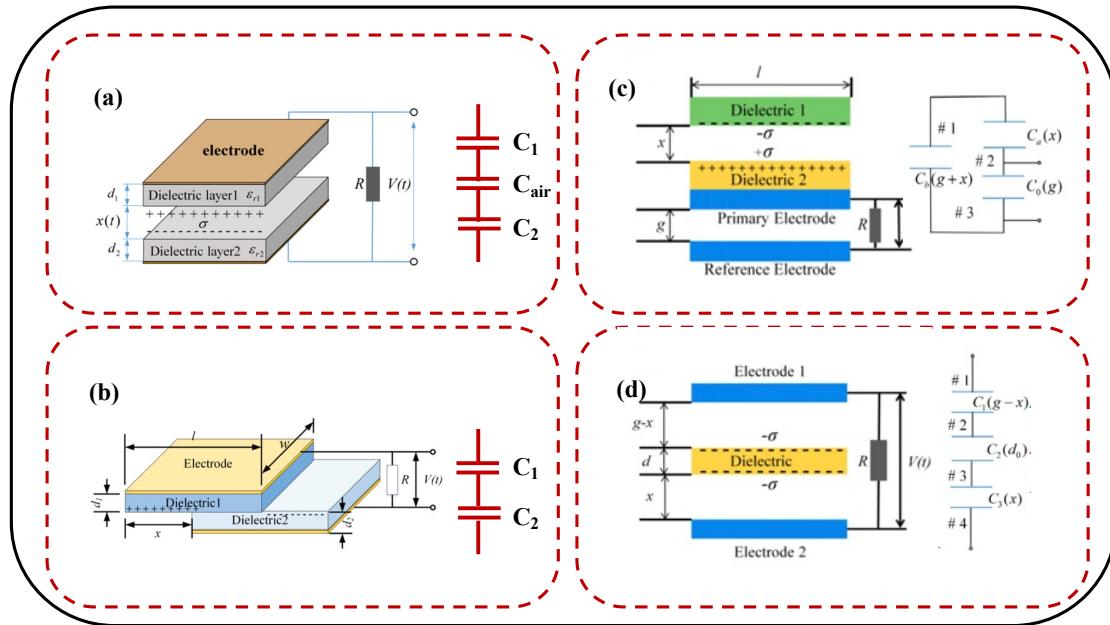


Fig. 2.4: Working principle of the four TENG modes of operation and their equivalent circuits [80, 90, 93, 102, 103].

iii. Single electrode contact mode triboelectric nanogenerator

Both CS-TENGs and LS-TENGs all require employing two electrodes to construct a closed circuit to conduct charges in the TENG-based circuit. However, the single electrode triboelectric nanogenerator (SE-TENG) overcomes the limits of applications and increases the diversity of energy harvesting (e.g. [73], [74], [75] and etc.). The SE-TENG could especially be applied as a human skin based TENG, due to its flexible and practical power generation model. Therein, it has high potential for use in tactile screen sensors or generators [76-78]. Fig. 2.4(c) shows the working principles and equivalent circuit of a SE-TENG schematically. The tribo-layer based on a layer of dielectric was coated by a layer of conductor as the electrode, and it requires to be connected with a reference electrode. After the independent tribo-layer makes contact with the bottom

dielectric surface, tribo-charges are generated on the dielectric and independent tribo-layer material surfaces. Due to the electrical potential based on the tribo-charges, the electrons flow from the electrode to the reference electrode [79]. When the independent tribo-layer makes contacts with the bottom interface again, the voltage between Node #1 and #2 decreases as the $x(t)$ reduces in Fig. 2.4(c). The relationship between the voltage between Node #1 and #2 (V_1), Node #1 and #3 (V_2) and Node #2 and #3 (V_3) is [68, 80]:

$$V_2 = V_1 + V_3 \quad (2.11)$$

Both V_2 and V_1 are decreasing, because the $x(t)$ and $x(t) + g$ are reducing. Thus, the charges are drawn from Electrode 2 back to the Electrode 1. When the device is in the open circuit condition, the total charges on Node #1, Node #2 and Node #3 are $-S\sigma_T$, $S\sigma_T$ and 0, respectively. Therefore, depending on the charge conservation, it can be seen

$$C_2V_2 + C_1V_1 = -S\sigma_T \quad (2.12)$$

$$C_3V_3 - C_1V_1 = S\sigma_T \quad (2.13)$$

Its open circuit voltage V_3 in Fig. 2.4(c) can be calculated by combining Eq. (2.11-2.13) as:

$$V_{OC} = V_3 = \frac{S\sigma_T C_2}{C_1 C_2 + C_2 C_3 + C_1 C_3} \quad (2.14)$$

Because $Q_{sc} = V_{oc} C_{2,3}$, the short circuit output charge could be obtained as:

$$Q_{sc} = \frac{S\sigma_T C_2}{C_1 + C_2} \quad (2.15)$$

Note that $C_{2,3}$ is the capacitance between Node #2 and Node #3, in which it is equal to:

$$C_{2,3} = C_3 + \frac{C_1 C_2}{C_1 + C_2} \quad (2.16)$$

iv. Contact freestanding tribo-layer mode triboelectric nanogenerator

Contact freestanding tribo-layer mode triboelectric nanogenerator (CF-TENG) is composed of two fixed metal electrodes and one freestanding dielectric layer between them, as shown in Fig. 2.4(d) [68, 81]. Both sides of the surface of the freestanding dielectric layer could contact intermittently with the two sides of the electrode interfaces depending on the external applied forces. When the dielectric layer makes

contact with the top metal surface, the top electrode generates tribo-charges; the charges conducted to the bottom electrode [81]. When the dielectric layer makes contact with the bottom metal layer, the distance ($g - x(t)$) between top metal layer and dielectric layer decreases until they are in contact. The bottom metal surface and dielectric layer bottom surface transfer tribo-charges and connect to the top electrode [68, 81]. Repeatedly, according to the middle dielectric layer motion between two electrodes, the alternating current is formed in the external circuit. Fig. 2.4(d) shows the working principle and equivalent circuit of a CF-TENG schematically. Comparing with the CS-TENG, the distance between two electrodes is fixed as g . However, due to the varying of the distance ($g - x(t)$ and $x(t)$) between the independent dielectric layer, the voltage between two electrodes could be calculated as (assuming the transferred charge on the electrode is Q) [81]:

$$V_{out} = \frac{\left(\frac{d_1}{\epsilon_1} + g\right)Q}{\epsilon_0 S} + \frac{2\sigma_T x(t)}{\epsilon_0} \quad (2.17)$$

$$V_{oc} = \frac{2\sigma_T x(t)}{\epsilon_0} \quad (2.18)$$

The CF-TENG is equivalent to three capacitors in series; thus, the total capacitance of the CF-TENG should be:

$$C_{total} = \frac{1}{\frac{1}{C_1} + \frac{1}{C_2} + \frac{1}{C_3}} \quad (2.19)$$

The charge quantity at short circuit stage should be:

$$Q_{sc} = \frac{2\sigma_T S x(t)}{\frac{d_1}{\epsilon_0} + g} \quad (2.20)$$

We have just reviewed the electrical theories of the four TENG modes, which all depend on the parallel plate capacitor model. However, in reality the plates are not infinite and the effect of their finite in-plane dimensions must be accounted for [59]. Therefore, a distance-dependent electric field model (DDEF model) was proposed by Dharmasena *et al*, 2017 [59]. In the DDEF model, the variation of the electric field is stimulated reasonably at different sites in the three-dimensional space firstly, and subsequently, the total electric field operating in a fixed dimension TENG device is calculated rather than regarding the triboelectric surfaces as an infinite plate. Integrating the charged micro-segments along the charged surface could account for the electric field across the tribo-

charges charged surface [59, 67]. Therefore, this triboelectric electric field across the contact surfaces should be corresponding to the separation distance rather than distributing uniformly in space. According to Dharmasena *et al* (2017) [59], the electric field in the vertical position of a surface not only depends on the vertical distance from the point in the space to the planar surface, but also relates to the dimension of the contact surface.

$$E_z = \frac{\sigma_T}{\pi\epsilon} \arctan\left(\frac{\frac{L}{W}}{\frac{2z}{W}\sqrt{4\left(\frac{z}{W}\right)^2 + \left(\frac{L}{W}\right)^2 + 1}}\right) = \frac{\sigma_T}{\pi\epsilon} f(z) \quad (2.21)$$

where, L and W are the length and width of contact surface. z is the distance from point to the contact surface, ϵ is the permittivity of medium and σ_T is the tribo-charge density.

Combining Eq. (2.21) with the TENG device structure, the potential of two electrodes can be calculated to investigate the open circuit voltage, short circuit current and output power even for non-planar devices. Therefore, the parallel capacitor model and the DDEF model are two fundamental models for prediction of TENG output. These models can also be used to inform TENG system design.

2.3 Triboelectrification of materials

In Section 2.1.3, we have reviewed theoretical models applicable to the four triboelectric nanogenerators (TENG) modes. According to these, TENG output performance depends on a number of factors, including the surface tribo-charge density [12], separation distance [59], device dimensions [82], permittivity of the tribo-contact materials [83] and difference in electron affinities of the interface pair [84]. Among these, the surface tribo-charge density is the key parameter driving TENG performance, because it is the energy source for a triboelectric device [12]. We have already discussed how surface tribo-charge generation depends on the contact materials. This is very much related to the differences in electron affinities (i.e. work function) of the interface pair [58]. When contact occurs at the interface, the material with high electron affinity (tribo-negative material) gains electrons from the material with low electron affinity (tribo-positive material) [57]. After that, the generated negative and positive tribo-

charges are fixed on the tribo-negative and tribo-positive material surfaces, respectively. Thus, it is critical for TENG design to select a pair of contact materials with large differences in tribo-properties. For the basic materials selection in triboelectric device design, the triboelectric series is the best reference [12, 85], as shown in Table. 2.2. In general, there are two positions in the series: positive and negative. Many of the common polymers are tribo-negative, including Teflon materials (e.g. PTFE and FEP), PDMS, PI (Kapton) and PVDF [86]. Metals such as gold, aluminum and copper are in the middle region of the triboelectric series [12]. However, nylon, silk and human skin are tribo-positive [20]. Generally, researchers adopt a tribo-negative material thin film (such as Teflon materials, PDMS, PI (Kapton) and PVDF) in contact with a tribo-positive material (such as metal, nylon or silk, etc.) to fabricate flexible TENGs. We now review some of the material possibilities in turn.

Table. 2.2: Triboelectric series for common materials following a tendency to lose electrons (positive) to gain of electrons (negative) [12].

	Polyformaldehyde 1.3-1.4	(continued)	
	Etylcellulose	Polyester (Dacron)	
	Polyamide 11	Polyisobutylene	
	Polyamide 6-6	Polyuretane flexible sponge	
	Melamine formol	Polyethylene Terephthalate	
	Wool, knitted	Polyvinyl butyral	
	Silk, woven	Polychlorobutadiene	
	Aluminum	Natural rubber	
	paper	Polyacrilonitrile	
	Cotton, woven	Acrylonitrile-vinyl chloride	
	Steel	Polybisphenol carbonate	
	Wood	Polychloroether	
	Hard rubber	Polyvinylidene chloride (Saran)	
	Nickel, copper	Polystyrene	
	Sulfur	Polyethylene	
	Brass, silver	Polypropylene	
	Acetate, Rayon	Polyimide (Kapton)	
	Polymethyl methacrylate (Lucite)	Polyvinyl Chloride (PVC)	
	Polyvinyl alcohol	Polydimethylsiloxane (PDMS)	
	(continued)	Polytetrafluoroethylene (Teflon)	

(Continue)

	Aniline-formol resin	Polyvinyl alcohol	
	Polyformaldehyde 1.3-1.4	Polyester (Dacron) (PET)	
	Etylcellulose	Polyisobutylene	
	Polyamide 11	Polyuretane flexible sponge	
	Polyamide 6-6	Polyethylene terephthalate	
	Melamine formol	Polyvinyl butyral	
	Wool, knitted	Formo-phenolique, hardened	
	Silk, woven	Polychlorobutadiene	
	Polyethylene glycol succinate	Butadiene-acrylonitrile copolymer	
	Cellulose	Nature rubber	
	Cellulose acetate	Polyacrilonitrile	
	Polyethylene glycol adipate	Acrylonitrile-vinyl chloride	
	Polydiallyl phthalate	Polybisphenol carbonate	
	Cellulose (regenerated) sponge	Polychloroether	
	Cotton, woven	Polyvinylidene chloride (Saran)	
	Polyurethane elastomer	Poly(2,6-dimethyl polyphenyleneoxide)	
	Styrene-acrylonitrile copolymer	Polystyrene	
	Styrene-butadiene copolymer	Polyethylene	
	Wood	Polypropylene	
	Hard rubber	Polydiphenyl propane carbonate	
	Acetate, Rayon	Polyimide (Kapton)	
	Polymethyl methacrylate (Lucite)	Polyethylene terephthalate	
	Polyvinyl alcohol	Polyvinyl Chloride (PVC)	
	(continued)	Polytrifluorochloroethylene	
		Polytetrafluoroethylene (Teflon)	

i. Polytetrafluoroethylene (PTFE) based TENGs

PTFE is a type of synthetic polymer where all the hydrogen atoms in polyethylene (PE) are replaced by fluorine atoms [87]. PTFE is one of the most commonly used tribo-negative materials in TENGs [88-92]. Simultaneously, because of properties of acid resistance, alkali resistance and resistance to organic solutions, the application range for PTFE based TENGs is extended [93]. For example, a Teflon material based single electrode TENG (SE-TENG) was used to detect the chemical sensing of solutions in Jiang et al. [94]. The PTFE based SE-TENG was tested on 10 types of ionic standard solutions, and it showed different sensing output (V_{oc} , I_{sc} and Q_{sc}) with each. Moreover, due to the super hydrophobic characteristic of PTFE thin films, one can even harvest water wave or water droplet energy using TENGs. Therein, Yang *et al* (2018) [117] used a PTFE based tribo-layer to make contact with DI water, tap water and 0.6M NaCl solution in a water tank. For the TENG with a pristine PTFE surface, the output power density could be 5mW/m^2 . Additionally, the output power density could be increased to 9.62W/m^2 , when the hydrophobic property of the PTFE surface was increased. A high-performance droplet electricity generator with metal/PTFE/ITO structure has also been designed using the super hydrophobic property of PTFE and the triboelectricity between the droplet and PTFE [118]. Note that after the droplet impinged on the PTFE surface, the tribo-charges could be generated by the droplets spreading, retracting and sliding. Therein, the maximum open circuit voltage and short circuit current could were approximately 143.5V and $270\mu\text{A}$. Therefore, using PTFE to harvest water energy has potential and requires further investigation.

ii. Polydimethylsiloxane (PDMS) based TENG

Polydimethylsiloxane (PDMS) is a variation of high molecular organic silicon compound, which is short for organosilicon [95]. Normally, sluggishness, non-toxicity and unflammability characterize PDMS [96]. Because of the properties of high viscosity, workability and ease of sealing with self and other materials, it always been fabricated as thin films with high surface functionalization [97-99]. For instance, exploiting the patterned silicon wafer, it is easy for PDMS to define the nanopatterns

on its surface. Because of the high surface-to-volume ratio, the contact area of the interface pair could be increased effectively, especially defining the mating contacting surface patterns [100]. A stretchable TENG was fabricated with PDMS micro-pyramids and Al coated PDMS micro-pyramids patterns to increase the effective contact area of two tribo-layers [93]. Other important properties of PDMS are its transparent and soft property which could also be applied in the TENG design (especially, using as a tactile screen sensor). Because of its high output sensitivity and self-power specialties, PDMS based triboelectric tactile screen sensors have the potential to replace the traditional electronic tactile screen sensor to reduce the pressure on battery life [101]. Human skin and PDMS could be combined as a SE-TENG (i.e. the maximum output power density could be $10\text{mW}/\text{cm}^2$) and employed as a tactile screen sensor [102]. Additionally, this SE-TENG could also be used as a pulse sensor which could perform 2V output voltage under pulse beating. PDMS is widely employed to design flexible and stretchable TENGs.

iii. Polyvinylidene fluoride (PVDF) based TENG

Polyvinylidene fluoride (PVDF) is also a material used, for example, in protective films for glasses, building exteriors and billboards [86]. Simultaneously, as a consequence of its capability in filtrating impurities (e.g. sediment and germs), PVDF thin films can also be used for pretreatment of sewage purification and sea water desalination [103]. Furthermore, the separation films, which are inside of many energy storage devices (e.g. supercapacitor, lithium battery and etc.), are adopted PVDF thin films [104, 105]. In the case of its application in energy harvesting, PVDF, which is composed of the repeating $-(\text{CH}_2-\text{CF}_2)-$ unit, is becoming one of the more popular polymer materials in piezoelectric and triboelectric technologies [50, 106]. Because of the all-trans (ttt) chain conformation for the β phase PVDF and its copolymer, it can generate a piezoelectric response or piezoelectric energy harvesting by external applied forces [107]. Therefore, PVDF and its copolymers have drawn tremendous attention as sensing materials in wearable and flexible sensors. According to the triboelectric series in Table. 2.2, PVDF is a tribo-negative material [85]. For example, a TENG device in

Mi *et al*, 2018 [108] using PVDF and CNF/PEI as the tribo-negative and positive materials generated 105V and $4.5\mu A/cm^2$ open circuit voltage (V_{oc}) and short circuit current (I_{sc}), respectively. Interestingly, a pristine β phase PVDF thin film (without any modifications) contacting Al foil can generate $0.8mW/m^2$ power density [109]. However, after performing the forward poling process on the PVDF, the output power could be increased over three times. The output power was decreased 1.3 times by the reversed poling process on the pristine PVDF thin film. This is because dipole alignment can be increased by the poling process (from the external electric field) to increase the material surface potential [109]. Additionally, reversed polarized PVDF decreased the device performance, because the position of the ferroelectric dipole moments mismatch with the triboelectric electric field [110]. Owing to this principle, the piezo/triboelectric nanogenerator has also been designed by inserting one PVDF layer under the negative tribo-layer to self-align the dipoles inside tribo-layer [111]. As a results of these, electrospun PVDF and its copolymer have been suggested as the tribo-negative layer, because of the high surface to volume ratio and surface potential [112]. Therein, PVDF is also an appropriate electrospinning material, because of its suitable solution viscosity [113]. Additionally, PVDF films also have other advantages, including high thermostability, high abrasive resistance (e.g., mechanical strength and toughness) and high chemical stability (e.g., resisting many chemicals and solvents) [113].

iv. Polyethylene terephthalate (PET) based TENG

PET is a semi-aromatic polymer that is synthesized by ethylene glycol and terephthalic acid as well as being one of the most commonly manufactured thermoplastics [114]. Its melting point and glass transition temperature is 250 to 255°C and 67 to 81°C, respectively [115]. Because of its characteristics of excellent abrasion resistance, high flexibility, creep resistance, high dimensional stability, weak corona resistance and fair oxygen barrier property, it is applied in industrial applications extensively. Simultaneously, PET is also a common contact or substrate material selection for use in flexible TENGs [116-120]. However, the electron affinity of PET is weaker as compared to the abovementioned polymers [12, 20]. Since it is in the middle region of

the triboelectric series, as shown in Table. 2.2, PET could be used as both a tribo-positive and negative material in the TENG designs [118, 119]. For example, a SE-TENG composed by a nanowire-structured PET thin film and Cu foil could generate 1000V, $4.3\mu\text{A}$ and $15\text{W}/\text{m}^2$ V_{oc} , I_{sc} and power density by 115L/min air flow [118, 119, 121]. Fan *et al* (2012) [122] fabricated a high transparent TENG by a regular and uniform PDMS patterned array based film and ITO coated PET as tribo-negative and positive materials, respectively. It could generate 18V and $0.13\mu\text{A}/\text{cm}^2$ output voltage and current density. Because the TENG exhibits a high transmittance of 75%, its potential application in touchscreen, high-definition LCD and self-powered electronic displays is obvious.

v. Metals in TENG design

According to the triboelectric series (Table. 2.2), metals are in the tribo-positive region: examples include aluminum (Al), copper (Cu), nickel (Ni) and gold (Au) [12]. Therefore, aluminum and copper are often employed as the tribo-positive material in TENG construction. These metals are also often used as electrodes. These can be prepared by commercial foils or by metallization etc. Furthermore, the foils could also be used as the substrate to fabricate the tribo-layer [123]. For instance, a solution of polymers (e.g. PDMS, PVDF, PMMA and PI) can be spin-coated on the foil. Additionally, the Al foil has been extensively used as the substrate to collect electrospun nanofibers, because of the conductive property [124]. After forming the nanofibers based thin film, the Al foil can then be used as the electrode of the tribo-layer [50].

In the previous sections, we have discussed fundamental principles, including the principle of power generation, modes of TENG operation, equivalent circuits and important triboelectric materials. The basic common parameters, which influence the output performance of TENGs, include surface tribo-charge density, permittivity, separation distance, sliding distance, thickness of tribo-layers, device dimensions, operation frequency and contact area. These parameters have been demonstrated as effective methods to improve the performance of TENGs, as shown in Table 2.3. A

detailed parametric study would be required to determine a rank order of the sensitivity of TENG output to the different parameters. Comparing with the dimensional and operational parameters in a TENG device (see Table 2.3), it could observe gains of 5.8 and 4.9 for V_{OC} and I_{SC} , respectively as real contact area (A_r) was increased from 0.25 to 82% (present work). It is less than the gains of 50 and 8.5 reported in [59] for V_{OC} and I_{SC} , respectively, as separation distance was varied from 0.1 to 1 mm. However, for example, the V_{OC} gain of 5.8 is comparable with V_{OC} gains of 2.6 to 8 reported with changes in tribo-layer thickness (0.02 to 2 mm) in [125, 126], while the I_{SC} gain of 4.9 is of a similar order to I_{SC} gains of 2.4 to 6 reported with change in frequency (0.5 to 5 Hz) in [59, 127]. Considering optimization via the interface materials, the tribo-charge density, which is key to power generation, (Table. 2.2) depends on the strength of the triboelectric effect generated by a particular interface pair [12]. Additionally, the major parameter used to quantify the surface tribo-charge generation performance for the contact materials is the material's surface potential [109, 128, 129]. Comparing with the other dimensional and operational parameters in TENGs, gains of 4 and 4.5 for V_{OC} and I_{SC} , respectively, when P(VDF-TrFE)'s surface potential was increased from -0.65 to -5.15V can be observed. It is approximate to the gains from A_r reported in the present thesis. Thus, increasing the materials surface potential is another significantly effective parameter to enhance CS-TENG performance. For example, after increasing the crystallinity of P(VDF-TrFE) in [133], its surface potential is enhanced from -0.87 to -2.37V and V_{OC} and I_{SC} of the device were optimized 1.7 and 1.8 times, respectively. Consequently, enhancement of the triboelectric performance of an interface surface pair via optimization of real contact area, surface potential and permittivity are promising routes to boosting TENG output.

Table 2.3: Literature comparison of TENG factors and parameters effecting electrical output.

	V_{oc} Gain	I_{sc} Gain
Frequency (f) Hz		
0.5 to 5 (PET & PDMS [59])	-	6
1 to 4 (Al & FEB [127])	1	2.4
1 to 5 (Cu & FEP [130])	1	3.6
0.3 to 3 (Nylon & PTFE [131])	1	-
Separation distance (d) mm		
0.1 to 1 (PET & PDMS [59])	50	8.5
1 to 20 (Al & PTFE [125])	9	2.5
Contact Material Permittivity (ϵ - relative)		
7.5 to 20 (PA6 & PVDF-BTO [126])	1.2	1.4
Thickness of Tribo-Layer (t) μm		
200 to 1000 (Nylon & PTFE [131])		
t for PTFE	2.8	-
32 to 220 (PDMS & PTFE [132])		
t for PDMS	7	2.2
300 to 2000 (Al & PTFE [125])		
t for PTFE	8	-
20 to 100 (PA6 & PVDF-BTO [126])		
t for PVDF-BTO	2.6	1.6
Real Contact Area Ratio (A_r) %		
0.25 to 82 (Cu & PET) [133]	5.8	4.9
Surface potential		
Al & (-0.65 to -5.15V) P(VDF-TrFE) [128]	4	4.5
Al & (-0.87 to -2.37V) P(VDF-TrFE) [109]	1.7	1.8
Al & (-240 to -540mV) PVDF/AgNW [129]	1.7	1.7
Crystallinity (FWHM)		
PET & (0.95 TO 0.81) P(VDF-TrFE)/BTO [50]	1.4	3.4
Al & (0.79 to 0.7) P(VDF-TrFE) [109]	1.7	1.8

2.4 Research progress on triboelectric nanogenerators

i. Real contact area

Surface roughness is known to affect aspects such as the frictional response of surfaces [134], the failure behavior of materials [135] and the contact stiffness of interfaces [136]. The real contact area between two rough surfaces is generally much lower than the idealized nominal contact area between two perfectly flat surfaces – this is an established result in the field of Tribology. What has been observed in the TENG literature is that CS-TENG electrical output is generally contact force dependent and generally increases as the force pressing the tribo-contact surfaces together increases [137-143]. Some researchers have reported results with electrical output (e.g., V_{oc} and I_{sc}) varying linearly with force [139, 141], while in others, a later-stage saturation occurs at higher forces [137, 138, 141, 142]. However, a link between contact area (mostly studied by tribologists) and electrical output in TENGs has never really been proposed and certainly has not been studied experimentally.

One might presume that charge transfer might increase with contact area since contact within the interatomic repulsive regime is required for electron transfer [63, 144]. In order to demonstrate this mechanism of surface tribo-charge transfer, material surface potential has been measured by Kelvin probe force microscopy (KPFM) between the centre of the scanned area and the edge after a KPFM scan [144]. Based on a parallel capacitor assumption, the tribo-charge induced dielectric surface potential change can be associated with the surface tribo-charge density as [145]:

$$\Delta V = \frac{\sigma_T t_{dielectric}}{\epsilon_0 \epsilon_{dielectric}} \quad (2.22)$$

$$\sigma_T = \frac{Q_T A_r}{A_n} \quad (2.23)$$

Q_T is the quantity of surface tribo-charges. Therefore, variation of surface tribo-charge generation could be predicted by investigating the material surface potential after combining Eq. 23 [133]. Li *et al* (2016) [144] extended the experiments of Zhou *et al* (2013) [145] by changing the phase shift of the KPFM probe vibration (from attractive to repulsive force regime). Depending on their experimental results, the surface potential change could be detected when the tip was vibrating at repulsive regime.

Inversely, there was no surface potential identified in the attractive regime. Therefore, these results demonstrated the surface tribo-charge generation is limited to areas of solid contact (i.e. real contact areas).

The influence of contact pressure on TENG output has been investigated by a TENG device consisting of a pyramid patterned PDMS surface (negative tribo-layer) in contact with a flat Ag surface (positive tribo-layer) in Fig. 2.5 (a) [137]. Typical increase in the open circuit voltage, with load, up to the point of saturation (Fig. 2.5 (b)) was shown together with microscopic images of the PDMS pyramids in contact with a glass slide which qualitatively indicated a corresponding growth in contact area (i.e. size of the square contact patches). From the simulation and experimental results, it can be seen that only point contacts at the peaks of the pyramids occur in the low contact pressure range (e.g. from 0.1 to 1 kPa). Because the PDMS based pyramids were deforming with increasing contact pressure, the contact area between glass slide and PDMS layer are approaching to full-contact status by the time the high contact pressure is reached. According to its electrical output (i.e. V_{oc}), it increases close to linear between 10 to 100 kPa and starts to saturate after 100kPa (Fig. 2.5(b)). The relationship between V_{oc} versus contact pressure has been predicted numerically in Fig. 2.5(c). Note, the transition point from the qualitative partial contact (PC) to the qualitative full contact (FC) condition matches with the transition point to V_{oc} saturation. However these results were somewhat qualitative – contact area was not measured and no relationship between the TENG outputs and quantitative measurement of contact area is evident in the contribution of Seol *et al.* [137].

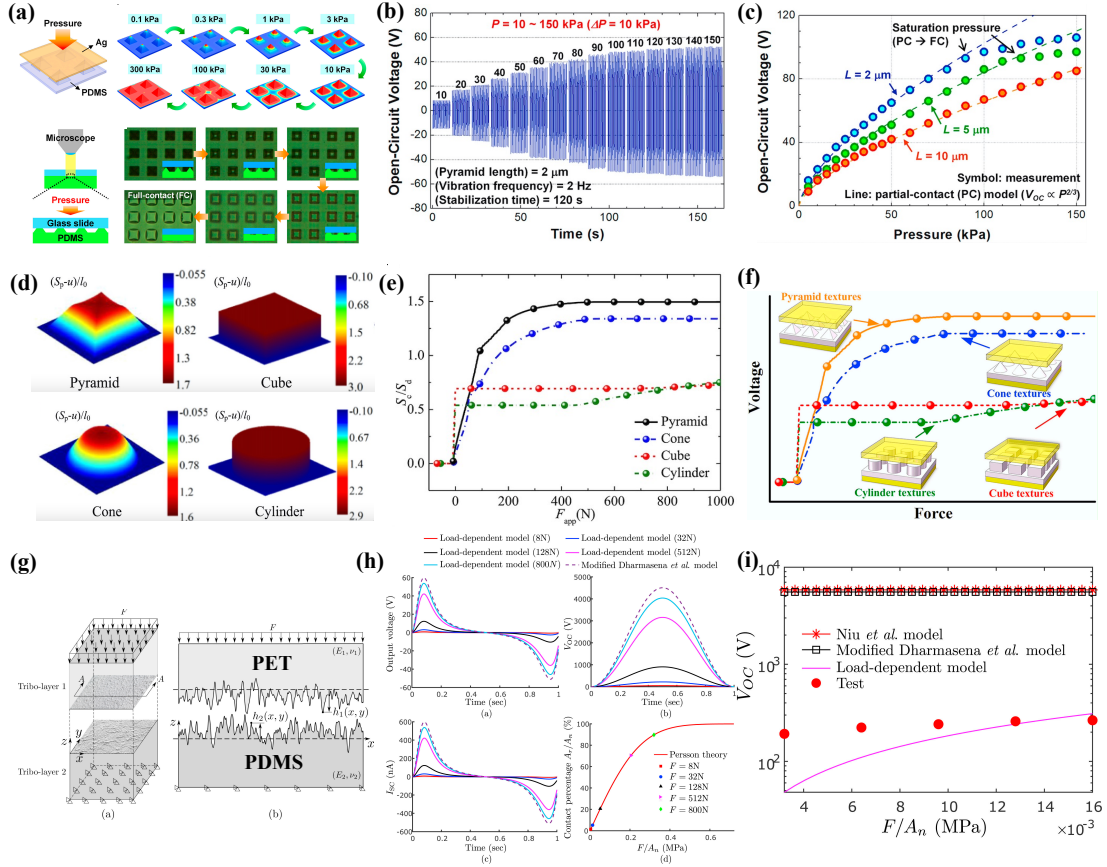


Fig. 2.5: Studies on the effect of contact area in CS-TENGs [160, 171, 172].

Yang *et al* (2018) [146] modeled the effect of different patterned surface types such as pyramids etc. (in contact with a flat surface) on the evolution of both contact area and electrical output (and included the effect of adhesion) – Fig. 2.5(d-f). The deformation of the pyramid and cone patterns are increased by rising the contact pressure, however, there is an extremely low deformation of the cube and cylinder patterns by the increasing contact pressure in Fig. 2.5(d). In addition, the variation of the contact areas (patterned surface in contact with the same flat surface) were calculated at different applied contact forces in Fig. 2.5(e). Especially, the effective contact area ratio increased at the low applied forces range (≤ 400 N) and saturated after applied forces ≥ 400 N for the pyramid and cone patterned surfaces. Oppositely, the deformations of the cube and cylinder patterns are roughly constant, and their contact area ratios are roughly constant in Fig. 2.5(e) as might be expected from the geometry. Note, the contact area ratio of the cone patterned film is lower than for pyramid patterned film. The electrical output results for V_{oc} of the CS-TENGs with pyramid and cone patterns

predicted the same changes with contact force as the effective contact area, which increase and later saturate as the surface pattern is flattened in Fig. 2.5(f). However, the V_{oc} for the CS-TENGs with the cube and cylinder patterns remain roughly constant – again in line with how the contact area varies for these geometries. Because the parameters of V_{oc} in Eq. (2.2) (e.g. the separation distance, device dimension and air permittivity) are constant, the variation of the V_{oc} is related to the change of the effective contact area ratio. However, this work was numerical and only considered structured surfaces with certain geometries.

A recent load dependent model (LDM) by the present authors in Xu *et al.* (2020) [147] has shown how accounting for a contact force-dependent real contact area (arising from random surface roughness) produces the commonly observed force-dependent TENG electrical performance, depending on the DDEF mode of CS-TENG in Fig. 2.5(g-i). Persson's contact theory is used to determine the real contact area of the interface pair and is therefore applicable to contact from first touch up to nearly complete contact (i.e. nearly 100% contact) as long as deformation remains elastic. Fig. 2.5(h) presents the contact area fraction as increasing linearly with increasing contact pressure from 0 to about 0.4MPa and saturating gradually after a contact pressure of over 0.4MPa. The DDEF model considered the generated tribo-charges distributed on a constant, unchanging nominal area, but the load-dependent model [147] essentially adapts the DDEF to a situation where the contact area evolves with contact pressure. The simulation study is carried out to study the influence of surface roughness (and real contact area) on the output voltage and short-circuit current of TENGs under different pressures. Comparing the experimental and simulation results, the simulated results from load-dependent model is more representative of the experimental results than the simulated results from DDEF model in Fig. 2.5(i). The important aspect being that the predicted voltage is now contact force dependent. These previous papers contributed to qualitative understanding enhanced by theoretical and numerical predictions. However, no quantitative experimental contact area measurements were plotted in any of these studies [137, 143, 146] and the experimental study by Seol *et al* (2015) [137] was based on qualitative observations of the deformation of idealized highly engineered (pyramid-

on-flat) type contacts. Therefore, the role of contact area still remains to be demonstrated experimentally via measurement and calculation of real contact. Crucially, this kind of experimental study needs to be applied to the general class of non-engineered nominally flat rough surfaces (i.e. all non-patterned surfaces).

Chapter IV of this thesis resolves this issue by accurately measuring both TENG real contact area and electrical output simultaneously over a wide range of contact pressures (from first touch to heavily loaded) for two nominally flat rough surface tribo-contact pairs. All other parameters are fixed so that just the effect of the contact force and area can be elucidated. Experiments are carried out where electrical output (such as V_{oc} & I_{sc}) were measured together with A_r under increasing contact pressure (or force) with identical test conditions for a TENG in contact separation mode. Fabrication of nano/micropatterns on the contact surface has been considered extensively as an approach to enhance the real contact area of the interface pair such as pyramids, line patterns, nano-helices and nanofibers [148, 149] – although many of these approaches do not succeed in enhancing contact area very effectively (primarily because of the gaps between the features). This aim of increasing contact area leads partly to the next topic: that of a TENG with electrospun PVDF-TrFE composite nanofibers. Here, there is also a second major optimizing factor – permanent material polarization made possible as PVDF-TrFE is ferroelectric. Hence, the next section reviews the literature related to the work in Chapter V on a ferroelectric-assisted high performance triboelectric nanogenerator based on electrospun PVDF-TrFE composite nanofibers with BaTiO₃ nanofillers.

ii. Electrospun ferroelectric assisted triboelectric nanogenerator

Many applications place very particular demands on TENG materials such as: high flexibility, ability to maximize electrical output and robustness in sustaining high mechanical stress/strain [150-154]. In terms of maximizing electrical output, a tribo-contact material pair that maximizes charge transfer is required. Four key factors that help optimize this are maximizing: (real) contact area [133, 147], difference in electron affinities of the interface pair [12], permittivity of the tribocontact materials [99, 155,

156] and difference in residual surface potential between the interface surfaces [128, 157]. With these demands in mind, materials that have received particular attention are the ferroelectric (FE) polymers polyvinylidene (PVDF) and copolymer poly(vinylidene fluoride-co-trifluoroethylene) (P(VDF-TrFE)) as these are flexible, but also allow for permanent polarization of the tribo-contact surfaces and are piezoelectric.

In Section 2.2, this manuscript has already discussed PVDF (with its repeating $-(\text{CH}_2\text{-CF}_2)-$ unit molecular structure). PVDF is one of the advantageous tribo-negative materials, because it is a fluoride. Note, fluorine has the highest electron affinity among the atoms to increase material triboelectric property [158]. Its co-polymer P(VDF-TrFE) combines the trifluoroethylamine structure into the PVDF molecular structure (i.e. $-(\text{CH}_2\text{-CF}_2)_m-(\text{CFH-CF}_2)_n-$). In addition, the polar β -phase is crystallized from the melt form of P(VDF-TrFE) readily comparing with PVDF [109]. According to Nalwa (1995) [159], crystallinity of P(VDF-TrFE) up to 90% can be achieved by pretreatment. Simultaneously, the high crystallinity of PVDF-TrFE can increase its negative tribo-property for the application of PVDF-TrFE in TENGs as well. It has been demonstrated to promote higher crystallinity and better dipole alignment similarly to how high dipole moment solvents have been shown to increase crystallinity and dipole alignment for P(VDF-TrFE) [126]. As expected, a high triboelectric output performance corresponds to the TENG device with highest crystallinity P(VDF-TrFE) thin film. The higher crystallinity results in a higher dipole alignment of P(VDF-TrFE), and the presence of aligned dipoles in the β -phase of ferroelectric (FE) polymers results in the enhancement of the spontaneous polarization (i.e. higher surface potential) and hence the surface charge density [160]. Thus, enhancing the crystallinity of the FE polymer is an effective method to optimize the ferroelectric assisted TENG performance. Comparing with PVDF, P(VDF-TrFE) has been selected as the tribo-negative polymer in Chapter V, because PVDF-TrFE could be fabricated at higher crystallinity than PVDF under the same conditions.

Additionally, recent work has shown significant improvements (1 to 5 times) in TENG electrical output when polarized PVDF or P(VDF-TrFE) are compared to their non-polarized equivalent [66, 160, 161]. Especially, Lee *et al* (2016) [162] analyzed the

influence from the polarization of P(VDF-TrFE) thin film for the TENG devices, including forward, reverse and non-polarized situations. The experiments not only explained the effect from surface potential for a TENG device, but of most interest is the tribo-property changed by the direction of the polarization. From their results, the highest occupied energy level of electrons of original P(VDF-TrFE) was shifted to the lower or higher level by forward or reverse-polarizing its thin film. After that, differences of work function between the contacting materials are enhanced and this boosts the tribo-charge transfer between the interface pair surfaces. The poling process is the general method to increase the β -phase formation and crystallinity of P(VDF-TrFE) [163]. However, to promote the β -phase formation and crystallinity, electrospinning also could be used as it combines uniaxial stretching and electric field poling in a single step [133, 147, 164]. The jet initiation could not happen for the viscous PVDF-TrFE solution until applying the high voltage during the electrospinning fabrication, because the electrostatic force is inadequate to overcome the surface tension of the PVDF-TrFE solution droplet and shoot out the droplet from the nozzle [165-167]. It is clear that the high voltage can increase the stretching force, because it is observed that the diameter of the nanofiber decreases with increasing voltage [165]. Therefore, the PVDF-TrFE molecular chains dipole is oriented as the stretching of a polymer jet under the high applied voltages during the electrospinning fabrication to shift it from α to β -phase [166, 167]. For example, experimental results have shown that the PVDF β -phase content could be increased from 67.8% to 72.4% by increasing the applied voltage from 12kV to 25kV [168]. Simultaneously, the degree of crystallinity of the PVDF is enhanced from 48% to 56.3% corresponding to a growth of β -phase content from 70% to 76%, after applied voltage increases from 14kV to 20kV [169]. Hence, the high applied voltage can increase both the β -phase content and degree crystallinity of the PVDF-TrFE. Additionally, it has been reported that the real contact area could be increased by optimisation of the nanofiber surface shape [153]. Film surfaces include roughness and microscale defects and the nanofibers (from electrospinning) can potentially match the contours of these during contact. Due to the high surface-to-volume ratio of the interface pair, the contact area of the nanofiber

based TENG device could potentially be improved, compared with their spin-coated thin film-based equivalent. Therefore, electrospinning seems an attractive method to fabricate a high performance P(VDF-TrFE) nano-fibrous TENG. This has not been done before and is the subject of Chapter V.

Third, different material optimization routes have been followed to enhance the formation of the β -phase of FE polymers. For instance, it has been shown that addition of filler materials such as metal nanostructures, and ceramic nanoparticles into the FE polymer matrix can enhance the formation of a highly polar crystalline β -phase, because of the electrostatic interactions between the nanostructures and the highly aligned dipoles of the FE polymer chains [126, 128, 129, 170, 171]. The introduction of nanoparticles has another very important advantage i.e. high permittivity inorganic fillers can increase the dielectric constant of the tribo-contact materials, which serves to increase the TENG capacitance and hence the ability to store charge [126, 128, 155, 163]. As an example, by dispersing particles of tetragonal barium titanate (TBTO with formula BaTiO_3) in a PVDF matrix, an increase in open circuit voltage and short circuit current density of spin coated TENGs by 1.5 to 2.4 and 1.8 to 2.3 times, respectively has been reported [126, 128] (Table 2.4). Similarly, voltage and current increases of 1.6 and 1.5 times were observed with a similar dispersion of TBTO particles in a P(VDF-TrFE) matrix [128]. However, a significant observation from Seung *et al* [163] reports that the output performance of the P(VDF-TrFE)/TBTO thin film based TENG device could not be improved much without the poling process. This is because the more random dipole alignment decreases the intensity of the material intrinsic electric field and even the material surface potential. The electrospinning fabrication approach holds the potential to resolve this problem, because a high voltage can be applied during the fabrication. Considering that TENGs produce high voltages but low currents, the current density is a vital parameter for performance. If tribo-charge density increases with real contact area [133, 147], significant gains over the state of the art are potentially possible if above materials are used in fibrous form. In this regard, electrospinning can provide better outcomes than the methods such as spin coating used in previous works. Further, electrospinning could enable even more highly charged P(VDF-TrFE)/TBTO

(nanofiber (NF) based) surfaces capable of further boosting current density. The premise is that electrospinning the P(VDF- TrFE)/TBTO surface will lead to higher dipole alignment and crystallinity in the P(VDF-TrFE)/TBTO matrix (due to higher voltage and extra alignment due to fiber stretching).

Table 2.4: Typical PVDF based TENG performances compared with the present work (final row)

Contact materials	Fabrication Method	Category	Pressure (kPa)	Freq. (Hz)	V_{oc} (V)	J_{sc} ($\mu A/cm^2$)	$V_{oc}/Pressure$ (V/kPa)	$J_{sc}/Pressure$ ($\mu A/N$)	Sample size cm^2	Ref.
PVDF & Al	Electrospinning	Tribo	-	2	94.3	0.28	-	-	25	[172]
PVDF-HFP & Silicon Rubber	Electrospinning	Tribo+piezo	20	1	17	0.06	0.85	0.03	4	[173]
PVDF-AgNWs & Nylon	Electrospinning	Tribo+Piezo	12.5	3	240	3.0	19.2	2.46	4	[174]
PVDF & CNF/PEI aerogel	Electrospinning	Tribo	30	10	105	4.5	3.5	1.5	2	[108]
PVDF & Silk fibroin	Electrospinning	Tribo+piezo	32.1	4	500	1.5	15.6	0.47	8	[175]
PVDF/MXene & PA6	Electrospinning	Tribo+piezo	25	1	50	2.5	2	1	4	[176]
			125	4	300	15	2.4	1.2		
PVDF/Graphene & PA6	Electrospinning	Tribo+piezo	25	5	1373	14.1	54.9	5.64	4	[177]
			225	5	1720	21.3	7.6	0.95	4	
PVDF/MXene & Nylon 11	Electrospinning	Tribo+piezo	23	4	75	3	3.3	1.3	3	[178]
PDMS/BTO & Al	Spin-coating	Tribo+piezo	-	2	375	0.3	-	-	16	[179]
PVDF & PVA	Spin-coating	Tribo	15	5	230	1.5	15.3	1	4	[180]
P(VDF-TrFE) poled & Al	Spin-coating	Tribo+Ferro	380	5	10	4.0	0.03	0.11	1	[181]
P(VDF-TrFE) & PET	Spin-coating	Tribo+piezo	-	0.5	35	0.6	-	-	1	[182]
P(VDF-TrFE)/BTO poled & Al	Spin-coating	Tribo+ferro	98	-	45.7	1.25	0.47	0.13	1	[128]
PVDF-BTO & PA6	Spin-coating	Tribo+piezo	250	5	450	3.2	1.8	0.13	4	[126]
P(VDF-TrFE)/BTO & PET	Electrospinning	Tribo+ferro	12.8	4	315	6.7	24.6	5.23	6.25	[50]

Therefore, in this work, we develop high-performance hybrid-TENGs using electrospun fibrous tribo-negative surfaces based on P(VDF-TrFE) composites with dispersed BaTiO₃ (BTO) nanofillers in Chapter V. This is the first time that a nano fibrous P(VDF-TrFE)-based TENG has been developed. We also explore the use of cubic BTO (CBTO) as a means of probing the differences introduced by the piezoelectric TBTO as compared to the non-piezoelectric CBTO. Accordingly, three types of β -phase crystalline P(VDF-TrFE) NF-based films are fabricated (via electrospinning) as active negative TE layers: pristine P(VDF-TrFE), P(VDF-

TrFE)/CBTO and P(VDF-TrFE)/TBTO. PET sheet material is used as the positive tribo-layer in all three cases to complete the Fe-TENGs. Table 2.4 compares outputs from the studies discussed above and also includes the present work which exhibits the highest current density even though the contact pressure is the lowest – suggesting a significant boosting of current density via the approach in Chapter V.

iii. Self-powered/charging electronics/system based on triboelectric nanogenerator

TENGs have emerged recently as effective self-powered sensors: examples include physical sensors (e.g., dynamic pressure sensor, speed sensor, acceleration sensor, fluid sensor and position sensor) and biomedical or healthcare monitoring sensors [48, 183-191]. Firstly, a TENG is a displacement dependent energy device whether it be sliding or vertical separation distance. Because TENG output increases with displacement of the tribo-surfaces, there is a sufficient reason to use TENGs to detect motion. Fig.2.6(a) presents a work on multi-dimensional self-powered velocity and trajectory tracking sensors (VTTS) which are composed of a sliding mode TENG array and a LED array [184]. The moved location of an object can be regarded as it moves in a plane rectangular coordinate system on a 2D plane, as characterized by corresponding coordinates, (x, y) . Since TENGs can charge the LED array, the location of the object can be read out from the LED array with a resolution of $250\mu\text{m}$. This multi-dimensional VTTS can respond to the limitation of the test motion from single-dimensional motion sensor advantageously. Many modern industrial applications also require measuring speed effectively, including for transportation, airport baggage carousels and for robotic automation etc. Simultaneously, the motion or vibration speed (i.e. frequency) of TENGs is one of the important parameters governing their output [12]. For instance, Jing *et al* (2014) [185] reported a self-powered velocity dual-mode sensor to detect both rectilinear and rotary motion, depending on the variation of operational speed - see Fig.2.6(b).

Self-powered acceleration sensors based on TENGs have the potential to be applied to earthquake monitoring, vibration monitoring such as global position systems, biomedical devices, vehicle safety, intelligent electronic products and mechanical

equipment vibration monitoring and troubleshooting. A high performance self-powered acceleration sensor based on a TENG has been fabricated by a PVDF nanofibers-based film and a liquid Hg ball for vibration monitoring with a high sensitivity of $0.26 \text{ V}\cdot\text{s}/\text{m}^2$ by Zhang *et al* (2017) [190], as shown in Fig. 2.6(c). We say in Section 2.2.2 that electrical output has mostly been observed to be pressure dependent. Hence, a pressure sensor is the one of the basic applications of the CS-TENG. However, due to its pulse AC output signal, the CS-TENG is almost designed as dynamic pressure sensor, especially when applied as a wide range pressure sensor. Because the electrical output (e.g. open circuit voltage) of a CS-TENG is always saturated at high contact pressure, as shown in Fig. 2.5(b), there is a sufficient reason to use it as a wide range self-powered pressure sensor. For example, the electrical output (e.g., output voltage) shows linear variation in different contact pressures ranges (e.g., 0 to 5kPa, 5 to 60kPa and 60 to 600kPa), as shown in Fig.2.6(d) [192]. Another advanced TENG sensing application is to detect the characteristics of fluids, including gas and liquid flow [186]. Based on converting the mechanical energy from the fluid, the fluid characteristics (e.g., pressure & flow speed) can be recorded by the TENG (e.g. rotating TENG) effectively [191]. Additionally, wave energy and sensing also could be detected by a single electrode TENG due to the hydrophobic feature of the triboelectric material surface [188]. A self-powered water wave sensor was designed by Xu *et al* (2019) [189] with an accuracy of 10 mm, as shown in Fig 2.6(e). Self-powered sensors based on TENGs could also be applied in the field of smart medicine and biomedical engineering [193]. The basic parameters in these applications often depend on pressure and frequency such as heart and pulse monitoring [187]. Additionally, a textile TENG (T-TENG) was integrated with a sock to detect the gait information of Parkinson's disease patients [48]. This design also depends on the walking frequency of the patients and these are different at normal walking, loss of stride and freezing of gait. Collection of this data could allow medics to monitor patients in real-time, as depicted in Fig 2.6(f). Moreover, in the field of biomedical engineering, a PTFE based single electrode TENG was integrated into a medical infusion tube, and the triboelectric output signal can then represent the flow velocity of liquid and gas produced from the injector [183]. This can demonstrate the

monitoring of the transfusion process for a patient. In this section, the self-powered sensors based on TENGs have been reviewed from the perspective of physical sensors and biomedical or healthcare monitoring.

Due to their extensive design in orientation of object, patient monitoring, vibration monitoring, wide range pressure and speed sensing, the potential of the TENG-based self-powered sensor applications have been highlighted. In theory, expanded Maxwell equation demonstrated the reason why TENG-based self-powered sensors can actively detect the static and dynamic processes arising from mechanical agitation by TENGs output electric signals [194]. Note that the contact surfaces is deforming via the shear stresses between the interface pair. The second term (i.e., $\frac{\partial P}{\partial t}$) of the displacement current density (J_D) function is the current owing to the movement of the changed media as driven by an external mechanical agitation/force. In Wang's calculation [195] for $\frac{\partial P}{\partial t}$, the time variation of the surface charge density and the movement speed of the medium were import into the final results. The results also indicates the variation of the medium volume and surface are also influencing the TENG outputs. It also illuminates the potential of CS-TENGs to be a self-powered pressure sensore, because the shear stresses deformed the surface shape (i.e., the real contact area of the interface pair). This thesis builds on findings about the effect of contact pressure in Chapter IV to develop a wide rage pressure sensor for various novel sensing applications in Section VI.

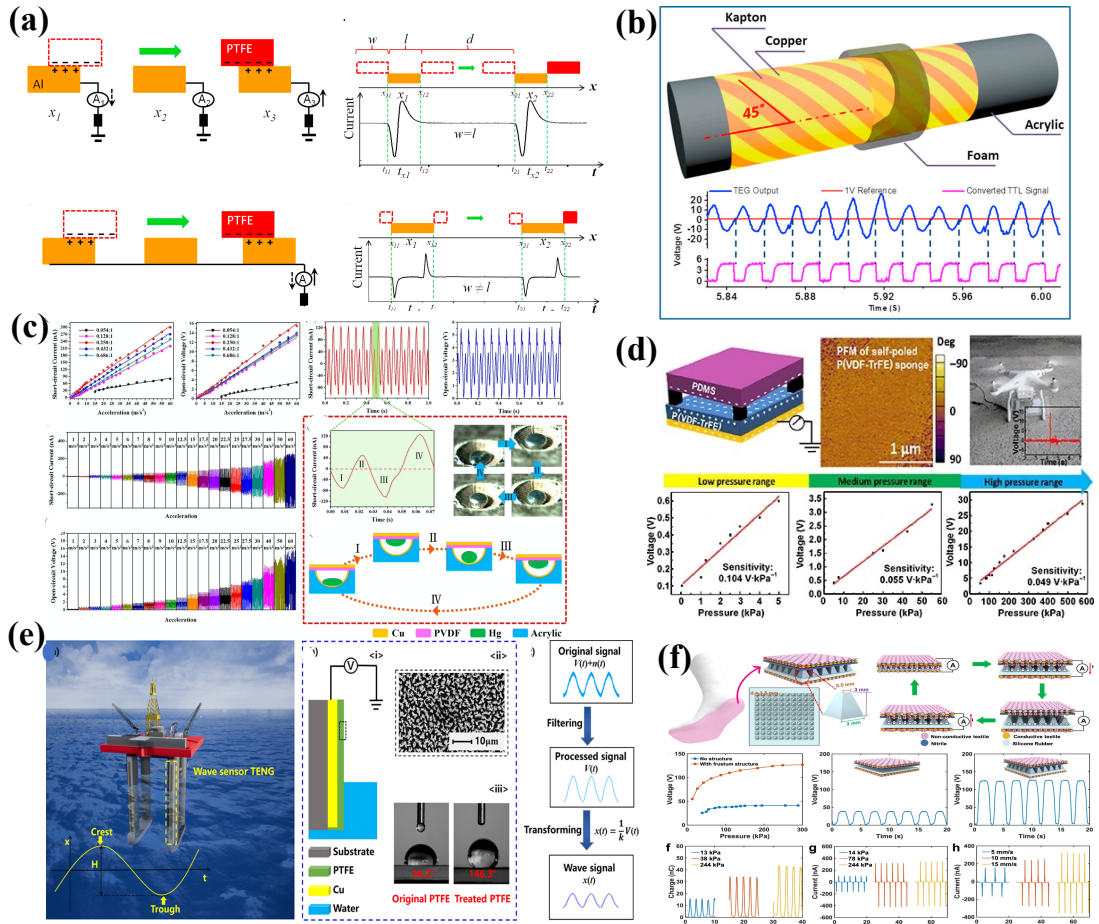


Fig. 2.6: A variety of applications of TENG based self-powered sensors, including: (a) self-powered velocity and trajectory tracking sensors (VTTS), (b) self-powered velocity dual-mode sensor, (c) self-powered acceleration sensor, (d) a wide range self-powered pressure sensor, (e) self-powered water wave sensor and (f) health monitor [47, 208-216].

Having explored TENGs as sensors, another important application for TENGs is as a power supplier to electronics or energy storage devices. Therein, charging energy storage should be one of the major applications for next generation TENG-based self-charging systems, because these self-charging systems can facilitate 24-hour powering by nanogenerators such as TENGs. Owing to the high voltage and low current characteristics of TENGs, one of the challenges for this TENGs-based self-charging system is reducing the charging time of the energy storage devices [196, 197].

Supercapacitors are the general selection in self-charging systems, due to their high-power density (i.e. lower the charging time), as shown in Fig. 2.7. Simultaneously, the TENG outputs are AC power and must be converted to DC power. Hence, a rectifier circuit is the most common method to integrate the TENG and supercapacitor [197]. In

order to improve the charging performance, the straightforward method is to increase the output power of the TENG. Two TENGs were integrated at the top and bottom side of one supercapacitor to enhance the input power, as shown in Fig. 2.7(a-b) [197]. Comparing with the system integrating one TENG and a supercapacitor, the stored voltage of the supercapacitor with two TENGs was increased 2 times with an 8s charging time in Fig. 2.7(b). The second challenge for the self-charging system is the integration between the TENGs and supercapacitors. Lou et al (2015) [196] inserted 4 microampere supercapacitors onto the TENG substrate in series as a single device. Since they are connected in series, the input currents are the same for each supercapacitor. Thus, although the required current for charging the supercapacitor array is not increased compared with a single supercapacitor, the output voltage from the supercapacitor array is enhanced four times, as shown in Fig. 2.7(c) [196]. This optimization not only decreased the input current for the supercapacitor array and improved the output performance of the supercapacitor array, but TENGs and supercapacitors could be integrated as a single device. By this method, the low input current from TENGs can be answered commendably. Finally, adopting the same materials for both TENG tribo-layer and the package of supercapacitor is another challenge, because this could reduce the complexity of the final integrated system, as shown in Fig. 2.7(c-d). Thus, it can decrease the number of the system layers and boost the range of device applications - a biodegradable self-charging system was fabricated by Shi *et al* (2019) [198]. Both supercapacitor package and TENG substrate used cellulose paper, and the interface pair of the TENG were nitrocellulose and PPy/cellulose paper. This design could combine the TENG substrate and supercapacitor package as one layer and extend the application range of this self-charging system due to its biodegradable property. However, the recent designs use an external circuit (or PCB) to combine TENGs and supercapacitors. Therefore, this is one of the key challenges for future work.

In this work, we successfully integrate the Fe-TENGs (P(VDF-TrFE)/TBTO) with a graphene electrode-based flexible supercapacitor to realize a self-charging system that can charge to 1.25 V in just 5 mins (see the application section of Chapter V).

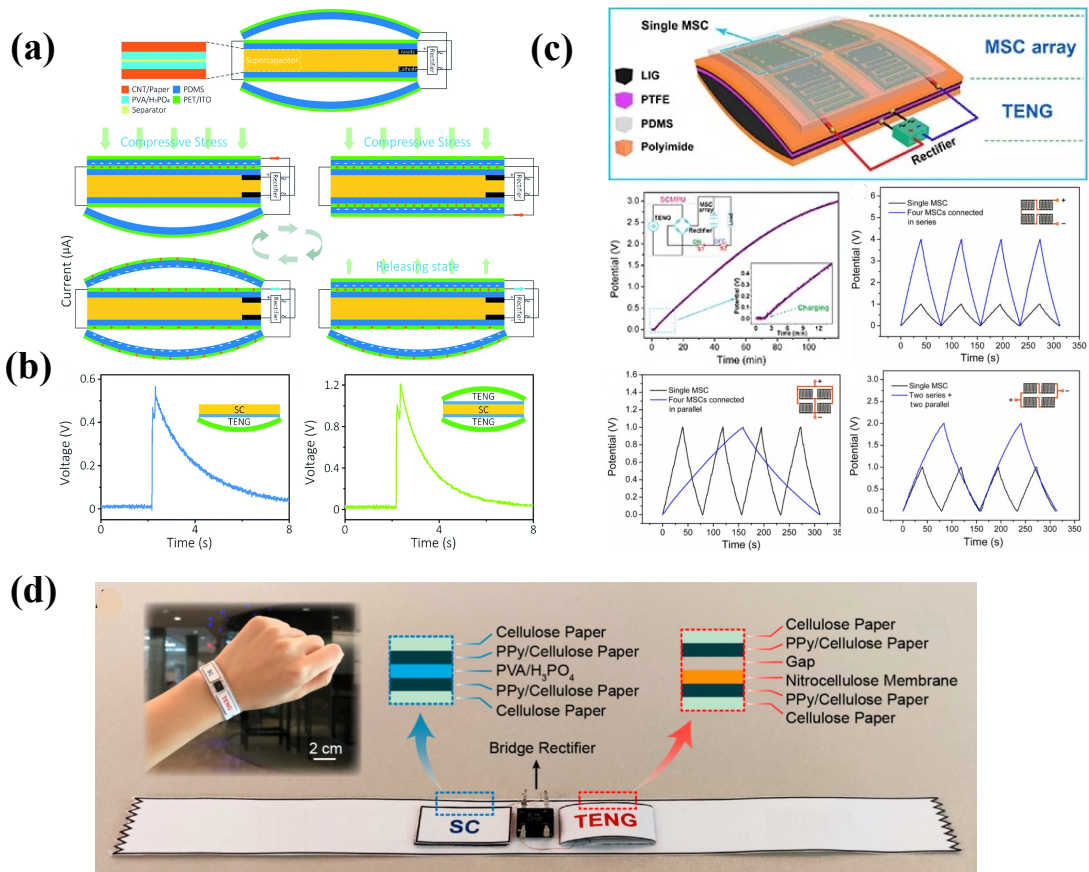


Fig. 2.7: Types of TENG-supercapacitor-based self-charging systems (a) sandwich shape self-charging power unit (SCPU), (b) output comparison of one TENG based SCPU and two TENG based SCPU (c) self-charging screen printed micro-supercapacitor power unit and (d) biodegradable SCPU [219-221].

In the previous sections, the methods of optimizing TENG performance have been discussed, including enlarging (real) contact area, difference in electron affinities of the interface pair, permittivity of the tribocontact materials (min) and difference in residual surface potential between the interface surfaces. Additionally, as we have just seen, TENGs have also been developed as self-powered sensors (e.g. acceleration sensor, dynamic pressure sensor, velocity sensor, trajectory tracking sensor and etc.) due to its high electric output and sensitivity. Examples are the TENG based self-powered pressure sensors in the sole of humanoid robots or in the shoes of a person with walking problems. Another reason why we need to optimize the performance of TENGs is the current gap between their power output (~ 0.1 - 100 mW/cm^2) [54] and the power needed to develop self-powered systems for charging sensors and electronics (8.44 - 107 mW/m^2) [199]. Generally, TENGs can generate electrical power from the ambient energy and use it to charge the sensors, sensor arrays and electronics. Additionally,

TENG generated power can also be channeled into energy storage devices such as supercapacitors and lithium batteries to realize 24-hour power supply to key applications. For example, the self-powered charging system with a ferroelectric assisted TENG and graphene electrode supercapacitor is sufficient for wearable applications as often low power sensors (nanowatt to microwatt power range [200-203]) need to be powered. Thus, the two major applications of TENGs are self-power electronics (system) and self-power/charging system.

2.5 Summary

This Chapter has presented an overview of TENGs and their applications. It has also explored key areas that are likely to be critical in leading to significant optimization of output. TENG output is still low when compared to many device power requirements and the need for optimization is clear. The chapter discussed the principle of operation of the four TENGs modes, TENG materials and triboelectric energy generation. Key areas with promise for significant optimization were identified. The identified areas are: real contact area, difference in electron affinities of the interface pair, permittivity of the tribocontact materials and difference in residual surface potential between the interface surfaces.

It was noted that reducing the permittivity of the tribo-contact materials would be likely to increase electric field strength and boost output. The problem is that low permittivity and optimized tribo-electric surface properties (tribo-positivity or tribo-negativity) do not necessarily coincide. An approach to finding an optimized solution to this problem is identified in Chapter III. The next route towards optimization emerged from results in the literature indicating that TENG output increases with contact pressure. There are some qualitative observations suggesting that a contact force-dependent real contact area might be the origin of this behavior. However, concurrent measurements of TENG electrical output and real contact area have never been made. Nor has this phenomenon been studied for standard engineering surfaces possessing random surface roughness. Hence, Chapter IV explores the fundamental origins of this behavior and shows how output can be optimized via contact area. The next impetus for optimization emerged

from the body of literature suggesting how permanent polarization of ferroelectric tribo-contact materials can be used to boost output. P(VDF-TrFE) with BaTiO₃ (BTO) nanofillers was identified as a suitable high performance ferroelectric material. Although PVDF/BTO and P(VDF-TrFE)/BTO have been used previously, this has been to produce a film based spin-coated TENG surface. What has not been explored is how much output can be boosted if high voltage electrospinning is used to create a nano-fibrous P(VDF-TrFE)/BTO TENG surface. Furthermore, the enhancing effects of the BTO nanoparticles has not been adequately explained. Previous studies have identified the benefit of their high permittivity, but have not explored their effect on the amount and degree of crystallinity of the β -phase in P(VDF-TrFE). These aspects are addressed in Chapter V which develops high-performance ferroelectric-assisted TENGs using electrospun fibrous surfaces based on P(VDF-TrFE) with dispersed BTO nanofillers in either cubic (CBTO) or tetragonal (TBTO) form.

The need to properly apply these high-performance TENGs in applications was also touched upon in the literature review. This means integrating with suitable energy storage and also designing novel TENG based sensors. An overview of the advances in TENG-based self-powered/charging electronics/system applications and its future challenges have been presented. In the present work, the advances in Chapters IV and V lead to the rapid charging TENG based super-capacitor system developed at the end of Chapter V and the wide-range pressure sensors developed and adapted to key sensing applications in Chapter VI. In conclusion, despite the plethora of challenges in optimizing TENG performance, high performance TENGs hold great promise for advances in many areas where renewable energy, self-powered sensors or self-charging system are needed. The review hints at a number of approaches that might be taken to further boosting output and these are explored in the subsequent research chapters.

Chapter III.

Modelling, simulation and optimization for contact and separation mode triboelectric nanogenerators

3.1 Introduction

The triboelectric nanogenerator (TENG) has emerged as an exciting new technology for localized electricity production. It simply utilizes the mechanical rubbing of certain surface pairs to produce electricity and has applications in harvesting energy from several sources [12]. The first significant paper on the topic of contact and separation triboelectric nanogenerator (CS-TENG) was published as recently as 2012 by Fan *et al* [66]. The power generation of CS-TENGs depends on the principle of contact electrification and electrostatic induction. The tribo-charge density, which is key to power generation, as well as, driving charge flow in TENGs, (Fig. 2.3) depends on the strength of the triboelectric effect generated by a particular interface pair [12, 57-59]. Based on the distributions of intrinsic electric field distributions during the power generation, a recent numerical model of CS-TENG operation has been developed by Niu *et al* [57]. The energy source (i.e. tribo-charges) is uniformly distributed over infinite plates in Niu *et al*; however, this model does not account for the fact that real TENGs consist of finitely sized plates and it leads to the artificial result of voltage indefinitely increasing with separation distance between the plates (Fig. 2.5(g) in [59]). The distance-dependent electric field (DDEF) model addresses this issue [59] and accounts for finitely sized plates – this gives a voltage which saturates beyond a certain separation distance. Xu *et al.* [147] improved the DDEF model by considering the theoretical influence from contact area due to the surface roughness on the contact surfaces and established the so-called load-dependent model (LDM). These fundamental numerical models were important steps in the development of our understanding of how TENGs work. They also allow simulation of the effect of various parameters on TENG performance (Section 3.2). This thesis studies these theoretical models initially to understand the working principles of the CS-TENG.

However, these numerical models say nothing about the generation of tribo-charge

density. Rather, they depend on an experimental value being input for tribocharge density. The surface tribo-charge density is one of the most important parameters, because it serves as the energy source for TENGs [12]. Therefore, the energy band approach was recommended to understand the surface charge transfer and the effected parameters of the contact materials [58, 60]. The surface tribo-charge transfer depends on balancing the differences in the contact materials band gap [60]. For the metals, they are characterized by their Fermi level (E_f), in which all the states are occupied below it. The states are empty above the Fermi level. For the dielectric, the molecular structure characteristics of its surface and bulk are different [60, 63]. The dielectric surface can be characterized by its conduction band (CB) and valence band (VB); however, the presence of surface/defect states in the bandgap should be assumed, owing to breaking the symmetry at the surface [63]. Some of the surface states in the bandgap (E_g) with energy below E_f could be filled up by electrons transferred from the metal into the dielectric surface during contact between the metal and dielectric. This is because the edge level of the valence band of the dielectric is lower than the Fermi level of the metal [58, 60]. It should be noted that this results in a dielectric surface with negative charges. The tribo-charge generation procedures and the calculation of surface tribo-charge density are discussed using the energy band approach in Section 3.3. The transfer of surface tribo-charges can simply be explained by the energy band theory. Additionally, the parameters, which affect surface tribo-charge generation, will also be highlighted from the tribo-charge density calculation. This modelling will establish the foundation for selecting the triboelectric interface pair and designing the triboelectric composites in the future TENG research.

Finally, this chapter presents a study on optimizing a low permittivity substrate below the tribo-contact surface so that gains from both strong triboelectric effect and low permittivity can be harnessed in a single device architecture. A simulation-based study is presented to investigate the effects of varying substrate relative permittivity upon TENG outputs such as open circuit voltage, short circuit charge density and short circuit current density. In addition to further in-depth simulation, two TENG devices fabricated with polyethylene terephthalate (PET) and polytetrafluoroethylene (PTFE) substrates

are tested to verify the simulation results. In order to assess the influence of substrate permittivity only, the tribo-contact materials are fixed as PET and PDMS films in both the simulations and experiments in Section 3.4. Therefore, the tribo-charge density of the devices can be considered constant. Other factors affecting the output parameters where also fixed to enable comparison including separation distance, frequency and applied force.

This chapter primarily discusses the following points:

- Introduction of the working principles of a CS-TENG by MATLAB simulation and summary of the impacted parameters from the device architecture.
- Analysis of the tribo-charge generation behavior by the energy band theory between the interface pair materials.
- A study on optimizing CS-TENG performance via a low permittivity substrate by both simulations and experiments.

3.2 Model of the working principle of contact and separation mode TENGs

The tribo-charges are the power source that drives TENGs to produce the free charges on the electrodes. In CS-TENGs, coupling of contact electrification and electrostatic induction define the operating principle. The transfer of opposite and equal tribo-charges occurs on each contact surface, owing to the difference in the triboelectric property of the contacting materials. The working principle applying to the open circuit voltage and short circuit current condition for a CS-TENG is shown schematically in Fig. 2.3 in Chapter II. The output performance of a TENG is actually dependent upon many factors, including surface roughness, thicknesses, separation distance and contact material properties. The open circuit voltage is created by the difference in potential between the electrodes as separation occurs. Simultaneously, these built-in electric fields cause the polarization of the dielectric material and produce the induced charges on the electrodes. In a short circuit mode, the charge is transferred from one electrode to the other. Therein, the separation distance between the interface pairs is one of most important parameters. Different open circuit voltages will be developed with different separations. The building of potential on the electrodes is also related to the intensity

of the internal electric field of TENGs. This depends on both the tribo-charge density σ_T and the permittivity ε as [59]:

$$E = \frac{\sigma_T}{2\varepsilon} \quad (3.1)$$

where, E is the electric field perpendicular to the charged surface, σ_T is tribo-charge density and ε is the permittivity of the medium. However, this electric field model is appropriate to a conventional capacitor rather than a CS-TENG, because the conventional parallel capacitor model assumes infinitely large charged planes. Hence, this model cannot explain the polarization of the dielectrics or the induction of free charges on the electrodes of a TENG completely. Therefore, the distance-dependent electric field (DDFE) model has been proposed to complete the explanation of the electric field variations of oppositely charged finite plates in relation to their contact-separation movement [59].

$$E_z = \frac{\sigma_T}{\pi\varepsilon} f(z) \quad (3.2)$$

$$f(x) = \arctan\left(\frac{\frac{L}{W}}{\frac{2z}{W}\sqrt{4\left(\frac{z}{W}\right)^2 + \left(\frac{L}{W}\right)^2 + 1}}\right) \quad (3.3)$$

where, L and W are the length and width of contact surface and z is the distance from point to the contact surface. Because the equivalent and opposite tribo-charges are located on two sides of the contact surfaces, the total overlapped electric field intensity on one side electrode can be presented as:

$$E_{total} = \frac{\sigma_T}{\pi\varepsilon_0} (f(x) - f(x + z)) \quad (3.4)$$

where, x is the distance from material surface to the electrode surface (i.e., the thickness of the tribo-layer). The electric potential can be described by the relationship between the distance and the total overlapped across the electrode as:

$$\varphi_1 = \frac{\sigma_T}{\pi\varepsilon_1} \left(\int_{x_1}^{\infty} f(x) dx - \int_{x_1+z}^{\infty} f(x) dx \right) \quad (3.5.1)$$

$$\varphi_2 = \frac{-\sigma_T}{\pi\varepsilon_2} \left(\int_{x_2}^{\infty} f(x) dx - \int_{x_2+z}^{\infty} f(x) dx \right) \quad (3.5.2)$$

They can be simplified as:

$$\varphi_1 = \frac{\sigma_T}{\pi\varepsilon_1} \left(\int_{x_1}^{x_1+z} f(x) dx \right) \quad (3.5.3)$$

$$\varphi_2 = \frac{-\sigma_T}{\pi\varepsilon_2} \left(\int_{x_2}^{x_2+z} f(x) dx \right) \quad (3.5.4)$$

where, $\varphi_{1,2}$ are the potential of two electrodes, $x_{1,2}$ are the thickness of the tribo-layers and $\varepsilon_{1,2}$ are the permittivities of the dielectric materials. Because there is not induced free charges on the electrodes, the electric potential of the electrodes can neglect the influences from the induced free charges. The open circuit voltage (V_{oc}) can be calculated as:

$$V_{oc} = \varphi_1 - \varphi_2 \quad (3.6)$$

Additionally, if the device is considered working at short circuit condition, the induced free charges on the electrodes will affect the potential of the electrodes. Thus, the potential of the electrodes could be described as:

$$\varphi_1 = \frac{-\sigma_U}{\pi\varepsilon_1} \left(\int_0^{x_1+x_2+z} f(x) dx \right) + \frac{\sigma_T}{\pi\varepsilon_1} \left(\int_{x_1}^{x_1+z} f(x) dx \right) \quad (3.7.1)$$

$$\varphi_2 = \frac{-\sigma_U}{\pi\varepsilon_2} \left(\int_0^{x_1+x_2+z} f(x) dx \right) + \frac{\sigma_T}{\pi\varepsilon_2} \left(\int_{x_2}^{x_2+z} f(x) dx \right) \quad (3.7.2)$$

where, σ_U is the induced free charge density on the electrodes

Because of the short circuit condition, $\varphi_1 - \varphi_2 = 0$

Therefore, the induced free charge density can be calculated as:

$$\sigma_U = \frac{\sigma_T \left(\frac{1}{\varepsilon_1} \int_{x_1}^{x_1+z} f(x) dx + \frac{1}{\varepsilon_2} \int_{x_2}^{x_2+z} f(x) dx \right)}{\left(\frac{1}{\varepsilon_1} + \frac{1}{\varepsilon_2} \right) \int_0^{x_1+x_2+z} f(x) dx} \quad (3.8)$$

The short circuit current (I_{sc}) can be evaluated as:

$$I_{sc} = A \frac{d\sigma_U}{dt}, \quad (3.9)$$

where A is the device area. The separation distance (z) is holding on a sinusoidal function for the device operation, as:

$$z = H \sin \left(2\pi ft + \frac{3\pi}{2} \right) + H \quad (3.10)$$

From the Eq. (3.5.1-3.6) and (3.8-3.9), the key parameters influencing CS-TENG output performance are tribo-charge density, separation distance, thickness of the tribo-layer and contact area. The tribo-charge density is a constant which is related to the contact materials. A dielectric-dielectric CS-TENG, which is using PDMS and PET as the interface pair, was selected for the numerical simulation in Fig.3.1. PDMS and PET films with $20\mu m$ and $200\mu m$ thickness, and another PET sheet with $100\mu m$ was

adopted as the substrate under PDMS film. Moreover, the relative permittivity of PDMS and PET was 2.72 and 3.3, respectively. Note, the relative permittivity of the top tribolayer can be calculated as 3.24 by the parallel capacitor model [43]. The tribo-charge density used was $40.7\mu\text{C}/\text{m}^2$ from [82]. Fig. 3.2(a) plots the result of open circuit voltage vs separation distance. The open circuit voltage is increasing linearly when the separation distance is under 18mm. Additionally, the growth rate of open circuit voltage is decreasing after the separation distance is over 18mm. Therefore, the separation distance is one of the important parameters for improving the open circuit voltage of CS-TENGs. However, the free charges can flow between two electrodes to counteract the difference in potential of two electrodes at short circuit current stage, as shown in Fig. 2.3 in Chapter II. Additionally, Fig.3.2(b-c) shows that the free charge and short circuit current density increase with rising separation distances. The output charge density can increase from 33.5 to $38.6\mu\text{C}/\text{m}^2$, when the separation distance increases from 1 to 10mm. In addition, the short circuit current density is improved 3.4 times, after the separation distances rise to 10mm. Thus, based on the simulation results and formula analysis, the increasing separation distance of CS-TENGs can influence the outputs as indicated.

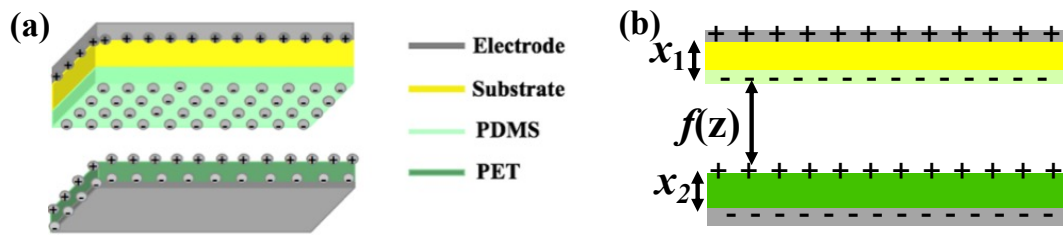


Fig. 3.1: Schematic of the CS-TENG used for numerical study by (a) 2D (b) 3D version [42].

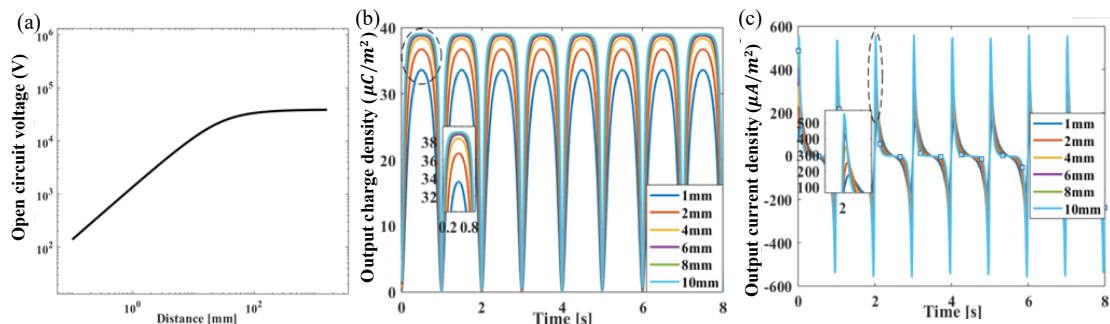


Fig. 3.2: Output performance with separation distance (a) open circuit voltage (b) output charge density and (c) short circuit current density.

The effect from the thickness of the tribo-layers for the device output performances was also investigated by the MATLAB simulation. The thickness of PET sheet is fixed at $100\mu m$ as well as the thickness of PDMS film are defined as 120, 80, 40 and $20\mu m$. Fig. 3.3(a-c) shows the simulation outputs (open circuit voltage vs separation distance, short circuit charge density vs time and short circuit current density vs time) of the device with different thickness of PDMS films. Simultaneously, Fig. 3.3 then illustrates these outputs against the thickness of PDMS. The open circuit voltage is increased with reducing thickness of PDMS, as shown in both Fig. 3(a) and (d). Herein, the open circuit voltage is raised from 1368V to 1371V under a fixed 1mm separation distance, after decrease the PDMS thickness from 120 to $20\mu m$. Moreover, the short circuit current density and short circuit charge density decline with the growing thickness of PDMS from Fig 3.3(b) and (e). Also when the thickness of PDMS film is enhanced from $20\mu m$ to $120\mu m$, the short circuit current density decreases from 174.6 to $155.4\mu A/m^2$ (i.e., 12.3% reduce). This enhancement with $20\mu m$ thickness PDMS film can be 1.12 times the output of short circuit current density from the device with $120\mu m$ PDMS as the negative triboelectric interface. A similar trend is observed with short circuit charge density in which it increases from 32.28 to $33.63\mu C/m^2$ over the range of thickness of PDMS and 1mm separation distance, as depicted in Figs. 3.3(c) and (f). Therefore, depending on the investigations of the outputs from the devices with different thickness of the contact material, a low thickness tribo-layer can increase the output performances of CS-TENGs.

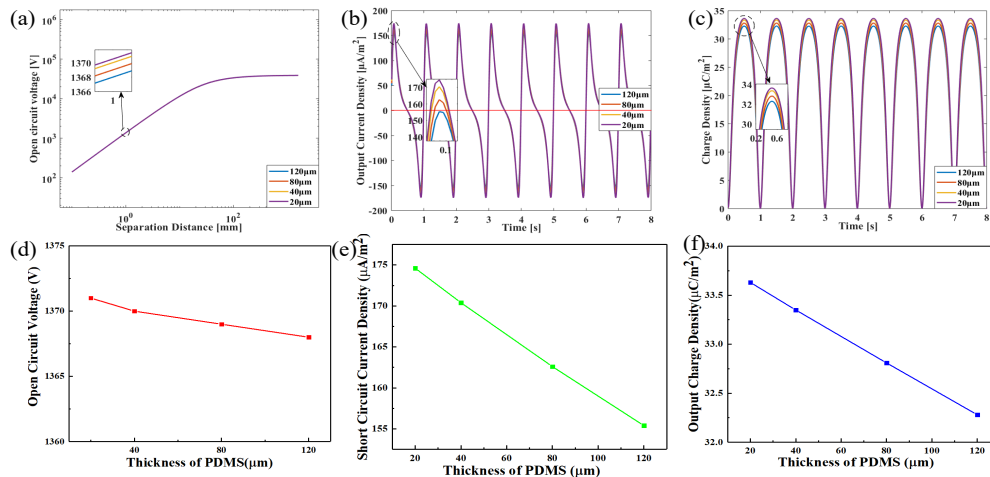


Fig. 3.3: The simulation results of (a) open circuit voltage (b) short circuit current density and (c) output

charge density. The effects for the output performances with thickness of PDMS (d) open circuit voltage, (e) output charge density and (f) short circuit current density.

Because of the inevitable presence of surface roughness, the contact area between the interface pair cannot achieve 100% contact (Chapter V) and, in many cases will be very much less. Simultaneously it is reasonable to assume that the tribo-charges can only be generated by *real* contact of the materials (i.e. atomic interaction). The contact area (S) in Eq. (2.1) in section II is inapplicable to the CS-TENG theoretical model, because tribo-charges can only be generated in the real contact area. Increased applied force induces growth of the real contact area between the contacting surfaces so that the total generated tribo-charge is likely to be increased. Depending on this hypothesis, a model of CS-TENG principle (load-dependent model) has been proposed by Yang *et al* (2020) [147]. The model essentially applies the concept of a load-dependent real contact area from the tribology literature on rough surface contact. The core of the argument in this model is that the tribo-charge density is redefined as:

$$\sigma_T = \frac{Q_T}{A_r} \quad (3.11)$$

where, the Q_T is the quantity of generated tribo-charges on the contact surfaces, but A_r is the *real* contact area between the interface pair. Secondly, the surface roughness was characterized by Persson's contact theory to determine the load-dependent contact area (Persson's contact theory gives a reasonable estimation of real contact area up to complete contact provided the deformation remains linearly elastic.). An error function of the normal force expresses the real contact area (A_r) in Persson's contact theory as [147]:

$$\frac{A_r}{A_n} = \operatorname{erf}\left(\frac{F}{A_n E^*} \sqrt{\frac{2}{|\nabla h_1|^2 + |\nabla h_2|^2}}\right) \quad (3.12)$$

Where $h_1(x, y)$ and $h_2(x, y)$ are the heights of two contact surfaces roughness and E^* is the composite modulus which can be calculated by:

$$\frac{1}{E^*} = \frac{1-v_1^2}{E_1} + \frac{1-v_2^2}{E_2} \quad (3.13)$$

where $E_{1,2}$ and $v_{1,2}$ are the Young's modulus and the Poisson's ratio of two tribo-contact layers, respectively. According to Eq. (3.12), the A_r is varying with contact force. The generated tribo-charges are distributing in the locations of real contact, and the

intensity of the formed electric field also depends on the A_r . The distance-dependent electric field expression in Eq. (3.3) can be improved as:

$$E_z = \frac{\sigma_T}{\pi} f(z) \quad (3.14)$$

Therein [147],

$$f(z) = \frac{\pi}{2} \left(-\frac{z}{\sqrt{\frac{A_r}{\pi} + (z)^2}} + 1 \right) \left(\frac{A_r}{A_n} \right)^2 \quad (3.15)$$

After integrating the E_z into Eq. (3.5.1 to 3.6) and (3.7.3 to 3.9), the characteristics of the CS-TENG depending on the contact force (or pressure) can be investigated, including open circuit voltage, short circuit current and transfer charge density in Table 3.1.

As a conclusion to the above-discussed formulas, it should be noted that the DDEF model has been established to improve the conventional CS-TENG, as tribo-charges are distributing on finitely sized charged planes. The DDEF model is more accurate in explaining the principle of a CS-TENG depending on Maxwell's equation, because this model shows the polarization of the dielectrics or the induction of free charges on the electrodes of a TENG. The key underpinning equations describing the operation of the CS-TENG are summarized below in Table 3.1.

Table 3.1. Summary table of the key theoretical formulas describing CS-TENG operation.

Electric field	V_{oc}	Q_{sc}	Ref.
$E_1 = \frac{Q_T}{S\epsilon_0\epsilon_1}$ $E_{air} = \frac{-\frac{Q_T}{S} + \sigma(t)}{\epsilon_0}$ $E_2 = \frac{Q_T}{S\epsilon_0\epsilon_2}$	$V_{oc} = \frac{S\sigma_T}{c_{air}} = \frac{\sigma_T x(t)}{\epsilon_0}$	$Q_{sc} = \frac{S\sigma_T}{c_{air}c_{total}} = \frac{S\sigma_T x(t)}{d_0+x(t)}$	Niu's model [57]
$E_z = \frac{\sigma_T}{\pi\epsilon} f(z)$ $f(z) = \arctan\left(\frac{\frac{L}{W}}{\frac{2z}{W}\sqrt{4\left(\frac{z}{W}\right)^2 + \left(\frac{L}{W}\right)^2 + 1}}\right)$	$V_{oc} = \varphi_1 - \varphi_2$ $\varphi_1 = \frac{\sigma_T}{\pi\epsilon_1} \left(\int_{x_1}^{x_1+z} f(x) dx \right)$ $\varphi_2 = \frac{-\sigma_T}{\pi\epsilon_2} \left(\int_{x_2}^{x_2+z} f(x) dx \right)$	$\sigma_{sc} = \frac{\sigma_T \left(\frac{1}{\epsilon_1} \int_{x_1}^{x_1+z} f(x) dx + \frac{1}{\epsilon_2} \int_{x_2}^{x_2+z} f(x) dx \right)}{\left(\frac{1}{\epsilon_1} + \frac{1}{\epsilon_2} \right) \int_0^{x_1+x_2+z} f(x) dx}$	DDFE model [59]
$E_z = \frac{\sigma_T}{\pi} f(z)$ $f(z) = \frac{\pi}{2} \left(-\frac{z}{\sqrt{\frac{A_r}{\pi} + z^2}} + 1 \right) \left(\frac{A_r}{A_n} \right)^2$	$V_{oc} = \frac{\sigma_T}{\pi} \left(2\epsilon_0^{-1} \int_0^{z(t)} f(z) dz + \epsilon_1^{-1} \left(\int_{z(t)}^{z(t)+x_1} f(z) dz - \int_0^{x_1} f(z) dz \right) + \epsilon_2^{-1} \left(\int_{z(t)}^{z(t)+x_2} f(z) dz - \int_0^{x_2} f(z) dz \right) \right)$	$Q_{sc} = V_{oc} C_{TENG}$ $C_{TENG} = \frac{A_n \pi}{\epsilon_0^{-1} \left(\int_{x_1}^{z(t)+x_1} f(z) dz + \int_{x_2}^{z(t)+x_2} f(z) dz \right) + \epsilon_1^{-1} \left(\int_{z(t)+x_2}^{z(t)+x_1+x_2} f(z) dz - \int_0^{x_1} f(z) dz \right) + \epsilon_2^{-1} \left(\int_{z(t)+x_1}^{z(t)+x_2+x_1} f(z) dz - \int_0^{x_2} f(z) dz \right)}$	Load-dependent model [147]

3.3 Modelling of surface tribo-charge transfer

In the previous sections, the parameters which influence the CS-TENG performance have been discussed separately except the generation of surface tribo-charge density. The tribo-charge generation is related to the contact electrification via tunneling effect between the contact materials [58]. Contact electrification depends on the charge transfer from the contacting particles (e.g. atoms or molecules) on the contact material's surface [20, 63]. Because of the dangling chains on the material surface (as the surface defects), a temporary bond between the contact particles will form [61, 62]. The

negative charges can be transferred onto the tribo-negative material surface, due to the high electron affinity. Additionally, the holes (positive charges) are left on the tribo-positive material surface. The large differences in the tribo-properties of the interface pair exist so that they can generate more tribo-charges on the contact material's surface. The basic materials for the interface pair are usually selected as a pair of materials with large difference in location in the triboelectric series (see Section 2.3). However, although the triboelectric series is a respectable reference for the contact material selection, it cannot explain the mechanism of surface tribo-charge transfer or the influential parameters involved in charge generation. Thus, according to the mechanism of the tribo-charge generation, the energy band for illuminating the charge transfer has been applied to explain these questions explicitly. In terms of contacting materials, there are two key types for TENGs: metal-dielectric and dielectric-dielectric. Next, tribo-charge generation in each of these two modes is explained.

3.3.1 Metal-Dielectric Mode

The energy band diagrams for the interface materials representing charge transfer are shown in Fig. 3.4 [58]. Owing to the differences in work function and electron affinity between the metal and dielectric, electrons will be transferred from the surface of the metal to the dielectric [59, 139, 204]. As the work function of the dielectric is generally larger than for a metal, the electrons from the top metal will be injected into the surface of the dielectric during the procedure of contact and separation until the surface states of the dielectric are as high as the Fermi level of the metal [58]. Moreover, there is a built-up electric field in the TENG. Also, the source of the electric field is from the tribo-charges when the interface pairs are separated. Due to electrostatic induction, the top and bottom electrodes are induced with the free charges (the charge density on the top and bottom electrode are σ_1 and σ_2 respectively, as shown in Fig. 3.4(a.)) [58]. Owing to the free charges on the top (σ_1) and bottom (σ_2) electrode that were induced by the tribo-charges (σ_T) on the surface of the dielectric, the relationship between tribo-charge density and induced charge density is [58]:

$$\sigma_T + \sigma_1 + \sigma_2 = 0 \quad (3.15)$$

(3.16)

Besides, because of losing electrons and built-in electric field for the metallic surface, the metallic vacuum energy level reduced by ΔE_{vcc} , which compares with the dielectric surface in Fig. 3.4. Thus, the ΔE_{vcc} can be calculated as:

$$\Delta E_{vcc} = \frac{\sigma_1 x e}{\varepsilon_0} \quad (3.17)$$

where x is a critical tunneling distance, e is the elementary charge and ε_0 is the permittivity of air. Moreover, the surface states of the dielectric should be the same as the metallic Fermi energy level after contact, owing to the equilibrium of the system.

Hence,

$$\sigma_T = -e \int_{E_0}^{E_0 + \Delta E_s} N_s(E) dE \quad (3.18)$$

where, $N_s(E)$ is the surface density of states, ΔE_s is the range of filled surface.

Therefore, the average of surface density of states can be described as:

$$\overline{N_s(E)} = \frac{\int_{E_0}^{E_0 + \Delta E_s} N_s(E) dE}{\Delta E_s} \quad (3.19)$$

Thus, simplifying the ΔE_s gives:

$$\Delta E_s = \frac{-\sigma_T}{\overline{N_s(E)} e} \quad (3.20)$$

From Fig. 3.4, the function between the energy of metallic and dielectric surface can be defined in Eq. (3.21), depending on the energy conservation as:

$$\varphi_1 + \Delta E_{vcc} = \varphi_2 - \Delta E_s \quad (3.21)$$

Simultaneously, the differential potential between two electrodes is:

$$V = \frac{\sigma_1}{\varepsilon_0} x - \frac{\sigma_2}{\varepsilon_1 \varepsilon_0} d \quad (3.22)$$

where the ε_1 is the permittivity of the dielectric. Therefore, the tribo-charge density can be calculated as:

$$\sigma_T = \frac{V + \left(\frac{\varphi_1 - \varphi_2}{e}\right) \times \left(1 + \frac{d}{\varepsilon_1 x}\right)}{\frac{d}{\varepsilon_1 \varepsilon_0} + \left(\frac{1}{\overline{N_s(E)} e^2}\right) \left(1 + \frac{d}{\varepsilon_1 x}\right)} \quad (3.23)$$

And at the open circuit condition as:

$$\sigma_T = \frac{\left(\frac{\varphi_1 - \varphi_2}{e}\right) \times \left(1 + \frac{d}{\varepsilon_1 x}\right)}{\frac{d}{\varepsilon_1 \varepsilon_0} + \left(\frac{1}{\overline{N_s(E)} e^2}\right) \left(1 + \frac{d}{\varepsilon_1 x}\right)} \quad (3.24)$$

Consequently, the tribo-charge density is related to the difference in work functions between two contact materials and the surface density of states in Eq, (3.24). However,

the tribo-charge transfer between the dielectric-dielectric materials is different from the metal-dielectric mode, because dielectric-dielectric mode depends on the different VB and CB structures of two contact dielectric materials [63]. The energy band analysis for the tribo-charge transfer of the dielectric-dielectric mode is depicted in Section 3.3.2.

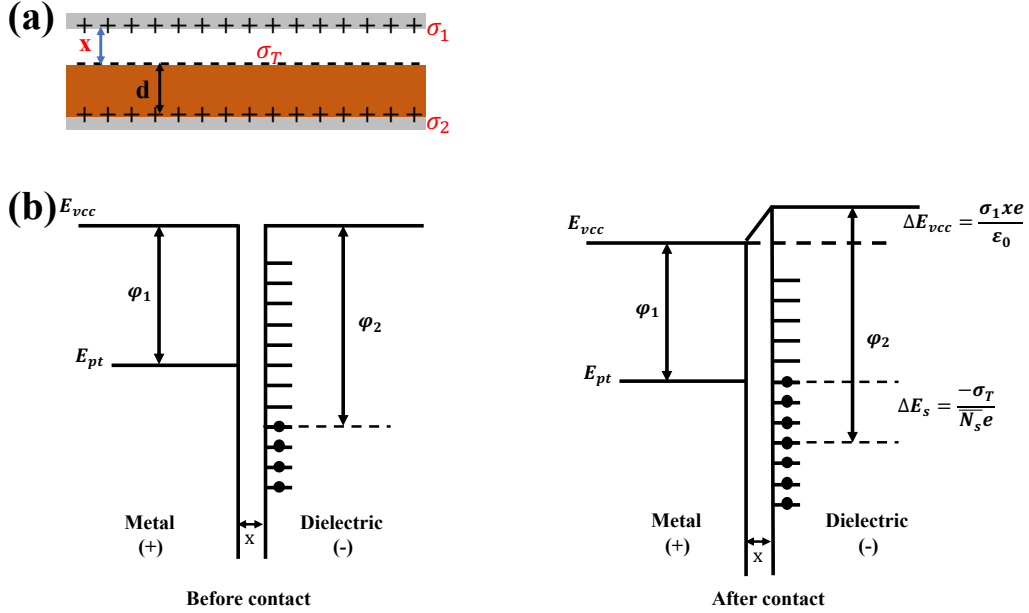


Fig. 3.4: (a) Schematic and device structure information of a metal-dielectric mode CS-TENG and (b) the energy band diagram for surface tribo-charge transfer at before contact and after contact status.

3.3.2 Dielectric-Dielectric Mode

Comparing the contact electrification of metal-dielectric and dielectric-dielectric materials, the free charges on the top electrode are induced by the tribo-charges on two sides of dielectric material surfaces rather than the single dielectric material surface, as shown in Fig.3.5. Simultaneously, after the equal and opposite tribo-charges on two dielectric surfaces appear, the generated tribo-charges are fixed on the material surfaces. Also, the transferred charge density should be satisfied by $|\sigma_1| = |\sigma_2| = |\sigma|$ [139]. Where σ_1 and σ_2 are the induced charge density on the top and bottom electrodes respectively in Fig. 3.5 and the σ is the transferred charge density. In order to balance the differences in VB and CB structures of two contact dielectric materials, the charges will transfer from one dielectric to another dielectric surface during the contact [60]. Due to the charge transfer, the variations of the Fermi level (compared with the original Fermi level) are presented as ΔE_{s1} and ΔE_{s2} . ΔE_{s1} and ΔE_{s2} are also related to the

surface density of states [60] as.

$$\Delta E_{s1} = \frac{\sigma_T}{\overline{N_{s1}(E)}e} \quad (3.25.2)$$

$$\Delta E_{s2} = \frac{-\sigma_T}{\overline{N_{s2}(E)}e} \quad (3.25.1)$$

where $\overline{N_{s1}(E)}$ and $\overline{N_{s2}(E)}$ are the surface density of states for Dielectric 1 and 2. Furthermore, owing to the opposite tribo-charges on each dielectric surface, the differential potential between two interface surfaces can be determined as:

$$V_{gap} = e \frac{\sigma_1 + \sigma_2}{\varepsilon_0} x = e \Delta E_{gap} x \quad (3.26)$$

where x is a critical tunneling distance, e is the elementary charge and ε_0 is the permittivity of air. Also, depending on the energy band diagram, the function can be presented by [60]

$$\varphi_1 + \Delta E_{gap} x + \frac{\sigma_T}{\overline{N_{s1}(E)}e} = \varphi_2 - \left(-\frac{\sigma_T}{\overline{N_{s2}(E)}e} \right) \quad (3.27)$$

Thus, based on Eqs. (3.25 - 3.27), the tribo-charge density can be calculated by [50]

$$\sigma_T = (e(\varphi_2 - \varphi_1) - \frac{2\sigma e^2 x}{\varepsilon_0}) \times \left(\frac{\overline{N_{s1}(E)} \times \overline{N_{s2}(E)}}{\overline{N_{s1}(E)} + \overline{N_{s2}(E)}} \right) \quad (3.28)$$

$$\sigma_T = \frac{e(\varphi_2 - \varphi_1)}{\frac{1}{\overline{N_{s1}(E)}} + \frac{1}{\overline{N_{s2}(E)}} + \frac{2e^2 x_0}{\varepsilon_0}} \quad (3.29)$$

Consequently, the equations of both metal-dielectric and dielectric-dielectric mode tribo-charge density have been calculated by analysing their energy band diagrams for surface tribo-charge transfer. From Eqs. (3.24) and (3.29), the key parameters governing tribocharge density are clear for both metal-dielectric and dielectric-dielectric modes. These are the differences in work function of the contacting materials, the surface states of the contacting materials and the permittivity of the materials. The difference in work function means the edge of the tribo-negative material Fermi level is lower than the tribo-positive material Fermi level. Thus, there are empty surface states that can be filled in the electrons from the tribo-positive materials. The number of the empty surface states is as high as the large differences in the work function of the interface pair. Contact materials surface states and permittivity are the key parameters to improve the tribo-charges density in Eq. (3.24) and (3.29). This result is helpful in approaching tribo-materials design for high performance TENG devices. For example, designing composites can increase the contact surface permittivity. Additionally, the

poling process on the contact material surface can be attempted, because the external voltage bias can shift the dielectric surface states. It should be noted that the material surface potential is the parameter to evaluate the shifting of the dielectric surface states [58, 63]. This aspect is explored in detail in Chapter V.

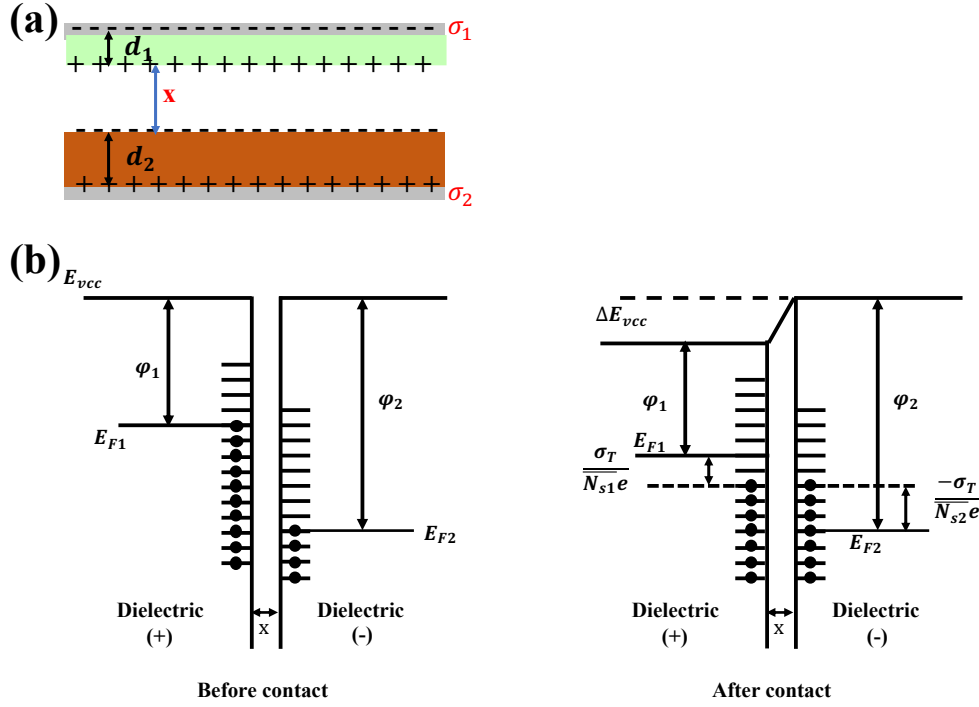


Fig. 3.5: (a) Schematic and device structure information for a dielectric-dielectric mode CS-TENG and (b) the energy band diagram for surface tribo-charge transfer at before contact and after contact status.

3.4 Optimizing CS-TENG performance via a low permittivity substrate

According to the numerical study in Section 3.2, the output performance of a CS-TENG has been simulated by MATLAB. Firstly, the simulation-based study is used to investigate the effects of varying substrate relative permittivity upon TENG outputs such as open circuit voltage, short circuit charge density and short circuit current density. In addition to further in-depth simulation, two TENG devices were fabricated and tested with polyethylene terephthalate (PET) and polytetrafluoroethylene (PTFE) substrates to verify the simulation results. In order to assess the influence of substrate permittivity only, the tribo-contact materials are fixed as PET and PDMS films (see Fig. 3.1) in both the simulations and experiments. Therefore, the tribo-charge density of the devices can be considered constant. Other factors affecting the output parameters were also fixed to enable comparison including separation distance, frequency and applied force.

Because of the same fabrication for the PDMS thin film, the contact area is also fixed by using the same applied force value.

3.4.1 Simulation and fabrication

A . Simulation

Using the distance-dependent electric field model of CS-TENGs in Section 3.2 [26, 38], the open circuit voltage and short circuit current was simulated (using MATLAB) for different substrate relative permittivity. The simulated TENG consists of two contacting layers which can be thought of as a parallel plate capacitor (Fig. 3.1). The ‘top tribo-layer’ is comprised of the tribo-contact material, the substrate and the electrode while the ‘bottom tribo-layer’ comprises just the partner tribo-contact material and its electrode. The interface pair (i.e. the tribo-contact material pair) was nominally selected as PDMS and PET (as in Fig. 3.1) to allow direct comparison with results from [59].

Accordingly, a tribo-charge density of $40.7 \mu\text{C}/\text{m}^2$ was used as in [59]. First, TENG operation was simulated for a selection of substrate materials and an optimum material was chosen based on optimum permittivity. The total equivalent permittivity of the top tribo-layer can be calculated by the parallel plate capacitor model. The capacitance of the substrate layer (in the top tribo-layer) is given by $C = \epsilon A / d$ [205], where C is capacitance, ϵ is permittivity, d is thickness of medium and A is the in-plane area. If the capacitance of the top layer is supposed as two dielectrics in one capacitor, the equivalent capacitance of the two materials comprising the top tribo-layer can be presented as:

$$\frac{1}{C_{eq}} = \frac{1}{C_1} + \frac{1}{C_2} \quad (3.30)$$

where, C_1 and C_2 are the capacitances of PDMS and the substrate, respectively. Combining Eq. (3.30) and the formula for capacitance above, the total relative permittivity of the ‘top tribo-layer’ can be calculated by [205] as:

$$\epsilon_{r,eq} = \frac{\epsilon_{r,PDMS}\epsilon_{r,Substrate}(d_{PDMS}+d_{substrate})}{d_{PDMS}\epsilon_{r,Substrate}+d_{Substrate}\epsilon_{r,PDMS}} \quad (3.31)$$

Where, the $\epsilon_{r,PDMS}$ and $\epsilon_{r,Substrate}$ are the relative permittivity values of PDMS and the

substrate, respectively and d_{PDMS} and $d_{substrate}$ are the thicknesses of PDMS and the substrate film (the ‘yellow’ layer in Fig. 3.1).

Table 3.2. Parameters for ‘top tribo-layer’ [42].

Substrate (PTFE, PET, Paper, Bakelite, Neoprene rubber, PVDF)	Contact Material (PDMS)
Thickness = 100 μ m	Thickness = 20 μ m
Relative Permittivity (ϵ_{r1}) varying (depending on type of substrate)	Relative Permittivity ($\epsilon_{r2} = 2.7$)
Size: 2cm \times 2cm	Size: 2cm \times 2cm

Table 3.3. Substrate relative material permittivity ϵ_r , ‘top tribo-layer’ relative equivalent permittivities $\epsilon_{r,eq}$ and ‘top tribo-layer’ absolute equivalent permittivities ϵ_{eq} [42].

Substrate Materials	ϵ_r of substrate materials	$\epsilon_{r,eq}$ of top tribo-layer	ϵ_{eq} of top tribo-layer $\times 10^{-12}$ F/m
PTFE (Teflon)	2.1	2.2	19.3
PET	3.3	3.2	28.2
Paper	3.7	3.5	30.9
Bakelite	4.9	4.3	38.3
Neoprene Rubber	6.7	5.4	47.7
$\alpha - phase$ PVDF	7.5	5.8	51.3

Using the relative permittivity for PDMS (Table 3.2) together with the substrate relative permittivity values in Table 3.3 (first column), the equivalent relative permittivity of the top tribo-layer was calculated using Eq. 3.31 for a range of substrate materials (PTFE, PET, Paper, Bakelite, Neoprene rubber and $\alpha - phase$ PVDF). These are listed as the second column in Table 3.3. The third column in Table 3.3 gives the equivalent absolute permittivity of the ‘top tribo-layer’. These materials represent a relatively wide range of permittivity values. Therefore, the relationship between substrate permittivity and TENG output (i.e. open circuit voltage, short circuit charge density and short circuit current density) can be summarized by simulating TENGs having these substrate materials. This essentially allows determination of an optimum substrate material. In the first part of the simulation work, the effect of substrate material relative permittivity on TENG output performance was studied using the same dimensions as in previous

literature [26], including the nominal contact area of $5\text{cm} \times 5\text{cm}$ and the thickness of the interface pairs (PDMS and PET) of 20 and $200\mu\text{m}$. This was done to allow direct comparison with the result in [26] where a PET substrate was used. Subsequently, the thicknesses of the PDMS and PET were altered to $20\mu\text{m}$ and $127\mu\text{m}$ and the nominal contact area was altered to $2\text{cm} \times 2\text{cm}$ (see Table 3.4) in order to match the devices fabricated in this work. Moreover, the thickness of the substrates was fixed at $100\mu\text{m}$. The relationship between substrate permittivity and TENG output was simulated by these parameters to compare the simulation and experimental results. Note, that the substrate is implanted under the negative triboelectric interface (PDMS). Based on these parameters, the open circuit voltage, short circuit current and charge have been simulated and results are discussed in Section 3.4.2.

Table 3.4: Comparison of fabricated TENG devices and test parameters [42].

Device 1	Device 2
Sample Size = $2\text{ cm} \times 2\text{ cm}$	Sample Size = $2\text{ cm} \times 2\text{ cm}$
Negative Contact Material – PDMS ($20\mu\text{m}$ thickness, $\epsilon_{PDMS} = 2.7$)	Negative Contact Material – PDMS ($20\mu\text{m}$ thickness, $\epsilon_{PDMS} = 2.7$)
Positive Contact Material – ITO coated PET film ($127\mu\text{m}$ thickness, $\epsilon_{PET} = 3.3$)	Positive Contact Material – ITO coated PET film ($127\mu\text{m}$ thickness, $\epsilon_{PET} = 3.3$)
Substrate Material – PET film ($100\mu\text{m}$ thickness, $\epsilon_{PET} = 3.3$)	Substrate Material – PTFE film ($100\mu\text{m}$ thickness, $\epsilon_{PTFE} = 2.1$)
4Hz Operation frequency	4Hz Operation frequency
8N applied force	8N applied force
1mm separation distance	1mm separation distance

B . Fabrication

For the experimental aspect of the work, two types of devices were fabricated based on two substrate materials having sufficiently different permittivity values (PTFE and PET - see Table 3.4 for comparison). The overall approach to device structure and fabrication is somewhat similar to that employed by Dharmasena *et al.* [59] with some differences. The bottom half of the TENG was fabricated simply as ITO coated PET film (sheet resistivity = $60\Omega/\text{sq}$, thickness 0.127mm , Sigma Aldrich, UK). The top half consisted of PDMS, the substrate material (either PET or PTFE) and a gold coating as the

electrode. PDMS is the negative contact layer and PET is the positive contact layer. To create the PDMS layer, PDMS cross-linker was mixed with its elastomer by a 1:10 ratio and degassed under vacuum for 45 min. Subsequently, the PDMS was spin-coated on a silicon wafer symmetrically at 3800 rpm for 60 seconds to obtain a 20 μ m thickness. In this experiment, the negative contact material (PDMS) and the positive contact layer material (PET) were fixed in order to ensure the same tribo-charge density generation for each device. A substrate sheet (100 μ m thickness of either PET or PTFE) with 2cm \times 2cm size was attached on the previous PDMS layer and cured at 70 $^{\circ}$ C for 2hrs. Finally, the gold film was deposited. The fabrication steps for the top triboelectric layer are shown Fig. 3.6. A layer of Kapton tape was required on each electrode for sufficient isolation. The mechanical energy supply for the TENGs was supplied by an oscillating force (maximum 8 N with frequency 4 Hz) using a TIRA shaker. The separation distance was fixed at 1mm and the open circuit voltage was recorded by an oscilloscope (KETSIGHT, MSO-X 4154A). The oscilloscope was connected with a voltage separation circuit comprising a $R_1=1\text{GOhm}$ and a $R_2=10\text{MOhm}$ resistor as shown schematically in Fig. 3.7. This was done to ensure that the impedance of the voltage meter setup was much larger than the TENG internal impedance.

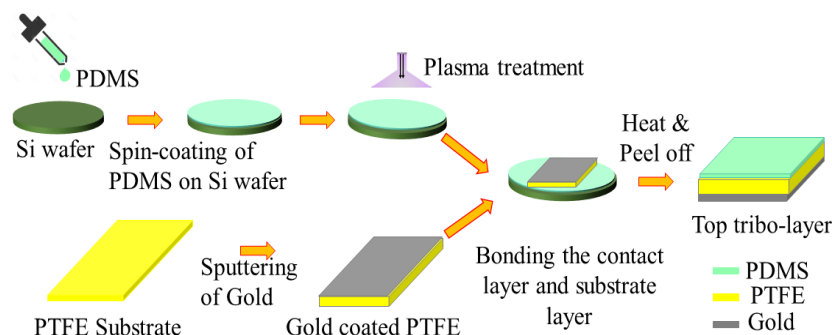


Fig. 3.6. Fabrication steps for the 'top tribo-layer' [42].

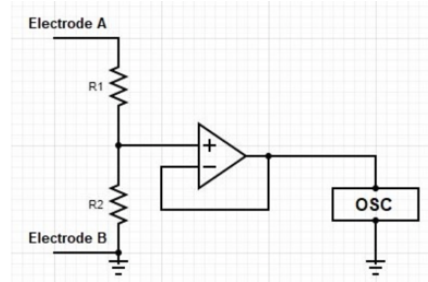


Fig. 3.7. Schematic of equivalent circuit for open circuit voltage measurements [49].

3.4.2 Results and discussion

A. Simulation results

Fig. 3.8(a) presents the device's outputs (open circuit voltage vs separation distance) for device dimensions of $2\text{cm} \times 2\text{cm}$. Fig. 3.8(b-d) reports the device output (open circuit voltage vs separation distance, short circuit charge density vs time and short circuit current density vs time) for a device having the same dimensions as the experimental devices (i.e. $2\text{ cm} \times 2\text{ cm}$). Fig. 3.8(e-f) then plots these outputs ($2\text{ cm} \times 2\text{ cm}$ area) explicitly against relative permittivity. Note, the results in Fig. 3.8(c-f) are for a 1 mm separation distance. It is clear from Fig. 3.8(a) that open circuit voltage increases significantly as the relative permittivity of the 'top tribo-layer' is reduced. Unsurprisingly, the trend in Figs. 3.8(a) and 3.8(b) is similar as only the device area and layer thicknesses have changed. In Fig. 3.8(e), the open circuit voltage increases from 1032 V to 1643 V (i.e. 1.6 times), when the substrate material changes from PVDF to PTFE (i.e. relative permittivity of substrate reduced from 7.5 to 2.1). The improvement with PTFE is 1.23 times the output reported in [26] with PET ($\epsilon_r = 3.3$) as the substrate material (the result from [26] is identical to the orange line in Fig. 3.8(a)). Hence, open circuit voltage can be enhanced by embedding a substrate with lower relative permittivity than the original triboelectric contact material to reduce the relative equivalent permittivity of the overall top triboelectric layer in Fig. 3.1. Although Fig. 3.8(c-d) shows short circuit charge and current density declining somewhat with increasing relative permittivity, Fig. 3.8(f) shows that the change is insignificant relative to the magnitudes of these outputs. Over the range of relative permittivity, they are approximately fixed at about $36.2\ \mu\text{C}/\text{m}^2$ and $229.2\ \mu\text{A}/\text{m}^2$ respectively. Hence, by choosing PTFE as the optimum substrate material, we can obtain useful increases in

open circuit voltage while not affecting current and charge density very much. In summary, the simulation results have indicated that open circuit voltage can be significantly improved, while short circuit charge density and short circuit current density are only very slightly increased by implanting a low permittivity material under the negative triboelectric interface.

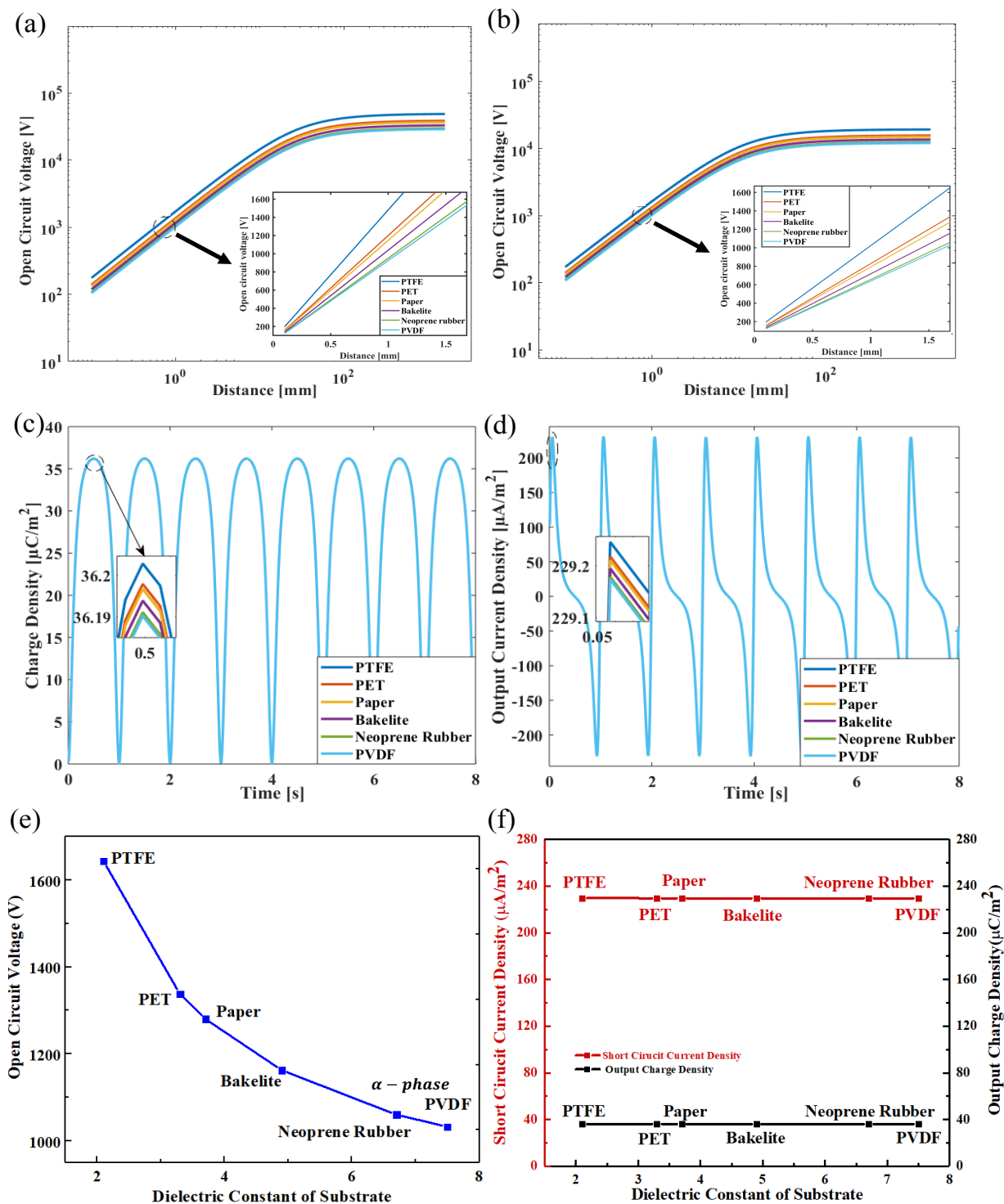


Fig. 3.8: Simulation results: (a) Open circuit voltage vs separation distance with 5cm×5cm areas and

200 μm thickness substrate, (b) Open circuit voltage vs separation distance with 2cm \times 2cm areas and 100 μm thickness substrate, (c) Short circuit charge density vs time, and (d) Short circuit current density vs time with substrate materials having a range of permittivity values (at 1mm separation distance for c and d), (e)–(f) Open circuit voltage, short circuit current density and short circuit charge density versus relative permittivity for different substrate materials (at 1mm separation) [42].

B. Experimental results

In order to provide a preliminary check on the validity of the simulation predictions, two materials from Table 3.4 (PET and PTFE – the best performing substrate materials in Fig. 3.8(e)) were chosen as the substrate material and two corresponding TENG devices were fabricated (described above) and tested. The devices were fabricated identically – the only difference being the relative permittivity of the substrate material reduces from 3.3 to 2.1 in going from a PET to PTFE substrate. Identical interface materials ensure that both devices generate the same tribo-charge density. Test conditions were also identical for both devices: a frequency of 4 Hz, a max load of 8 N and a 1 mm separation distance. The substrate thickness was 100 μm for both devices. A 5 min pre-charge time was employed before each set of measurements to ensure equilibrium of tribo-charge generation. Table 3.4 summarizes the device and test specifications. Fig. 3.9 plots the output open circuit voltage signal from both devices. The max output voltage increased from 29.5 to 39.4 V (i.e. 1.3 times) and the peak-to-peak value from 46.5 to 61.4 V (i.e. 1.3 times). These increases are very much in line with the simulation prediction from Fig. 3(e) where the simulated open circuit voltage increased by 1.3 times between PET and PTFE. Note, that the voltage magnitudes between simulation (Fig. 3e) and experiment (Fig. 6) are quite different however. A key reason for this is likely to be because the simulation results are based on a perfect contact interface; whereas, the amount of ‘real contact area’ in the experimental device (at these loads) is likely to be only a fraction of the nominal contact area. A lower experimental ‘real contact area’ would be likely to generate a reduced tribo-charge density at the interface and therefore, a reduced open circuit voltage output. Nevertheless, contrasting the relative voltage increase represents a valid comparison

and results suggest that the experimental check is in-line with the simulation prediction (as both predict an increase in open circuit voltage of roughly 1.3 for the move from PET to PTFE). Finally, the experimental results showed no appreciable difference in short circuit current density in moving from PET to PTFE substrates as predicted by the simulation result in Fig. 3.8(f).

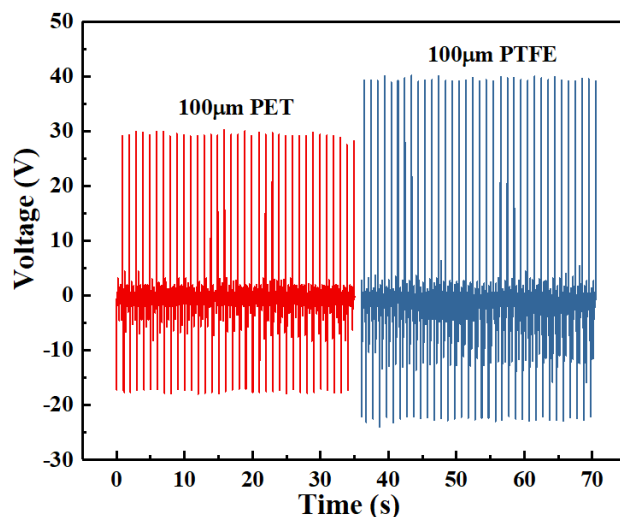


Fig. 3.9: Comparison of open circuit voltage signals for the devices with PTFE and PET substrates [42].

3.4.3 Application in a self-powered system by integration with a stretchable photodetector.

In this section, the fabricated CS-TENG is used to power an energy autonomous UV photodetection sensor. Before the demo, the high flexibility/conformability of the fabricated TENGs and photodetectors (PDs) were tested by placing them over human fingers and glass vials in Fig. 3.10. This qualitatively confirms the suitability of the fabricated devices for wearable applications.

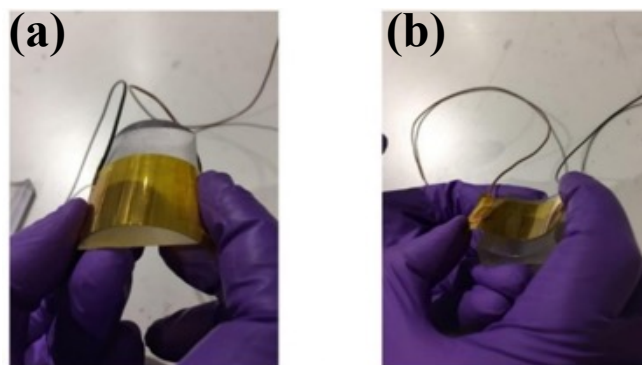


Fig. 3.10: Bending stability test for TENG devices: (a) Optical image while convex bending, (b) Optical image while concave bending [50].

Figure 0.1 Fig. 3.10: Bending stability test for TENG devices: (a) Optical image while convex bending, (b) Optical image while concave bending [50].

Accordingly, a self-powered UV PD concept was implemented by integrating a PD with the TENG through a rectifier bridge circuit. It was operated by applying an 8N force at 4Hz. A LED was connected in series with the PD, in other words, one terminal of the PD was connected to the TENG through the bridge rectifier circuit and the other end was connected to the LED light. The setup and the working demo of the self-powered PD are given in Fig. 3.11a. Without UV radiation, the resistance of the UV detector remains high so there is no current flow. As a result, the LED was in an ‘off’ state (Fig. 3.11b(iii)). When PD2 was exposed to UV radiation, the resistance of the PD decreased, allowing the current to flow through the PD and hence the LED started glowing, as shown in Fig. 3.11b(iv). Further, the harsh deformations (stretching, bending, and twisting) do not affect the ability of PD to detect the UV radiation (Fig. 3.11b(v and vi)). Thus, the presented self-powered stretchable PD can be attached to any curvilinear surfaces, such as fabric and skin, for real-time detection of UV radiation for health and environmental monitoring.

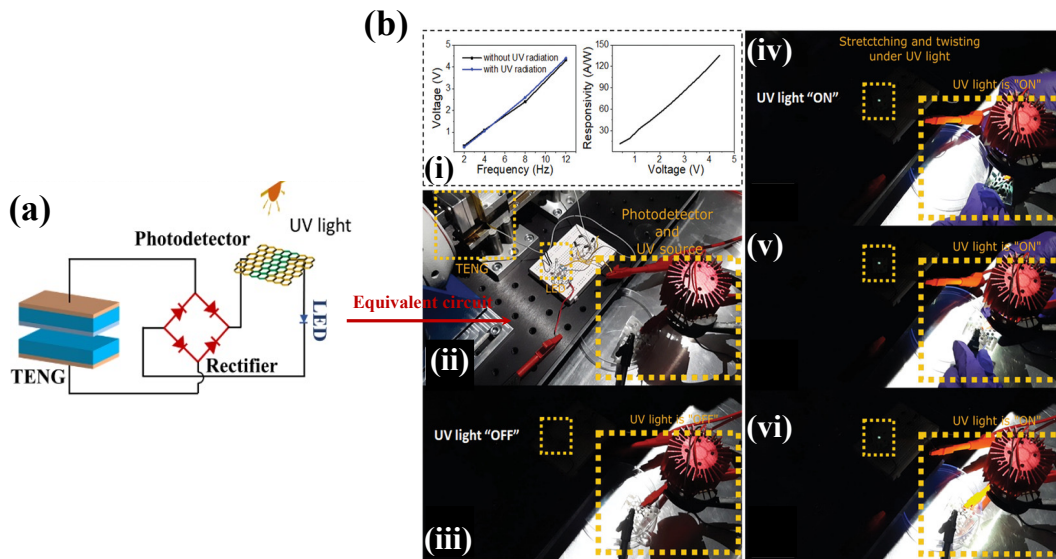


Fig. 3.11: (a) Equivalent circuit for TENG-PD based self-powered system, (b) Integration of stretchable PD with TENG: Output voltage of TENG at different frequency across PD irradiated with and without UV light and their respective responsivity at generated voltage. Photographic demo showing the connection of LED in series with self-powered photodetector for real-time UV detection [50]. (Courtesy: the photodetector was designed and fabricated by Dr. Yogeenth Kumaresan)

3.4.4 Summary on low permittivity substrate work

Materials with strong triboelectric effect and low permittivity are among the requirements for improving triboelectric nanogenerator (TENG) performance. These features are not always possible in the same material, so this work has outlined the idea of optimising a low permittivity substrate material underneath the tribo-contact layer so that both optimum triboelectric effect and low permittivity can be incorporated in the same TENG. Results (simulated using a distance-dependent electric field model) show that open circuit voltage increases with reducing substrate permittivity. Going from PVDF ($\epsilon_r = 7.5$) to PTFE ($\epsilon_r = 2.1$), open circuit voltage increased by a factor of 1.6. Therefore, PTFE was selected as a suitable substrate material. Therefore, simulation results show that low permittivity can be used to boost TENG performance. A preliminary check on the simulation results was provided by fabricating and testing two TENG devices having different substrate permittivity values. PET and PTFE substrates of 100 μm thickness were incorporated in otherwise identical devices. In moving from PET to PTFE substrates ($\epsilon_r = 3.3$ to $\epsilon_r = 2.1$), the experiments predicted almost the same increase in open circuit voltage as the simulations (roughly 1.3 times). Experiments also confirmed little increase in short circuit current density with substrate permittivity as predicted by the simulations. The conclusion is that low permittivity substrates can be used to enhance the open circuit voltage of TENGs. Current work is concentrating on looking at this effect over a wider range of substrate materials. In future, we will focus on demonstrating the further significant gains predicted by further reducing the substrate thickness. Finally, TENGs are currently being considered as a viable autonomous energy supply source for a host of self-powered sensor technologies and the advances discussed here in terms of enhancing output will be directly useful in those sensor applications.

3.5 Conclusions

This chapter initiates the task of attempting to optimize the output performance of the CS-TENG. First, the evolution of the key models describing CS-TENG operation were analyzed as a means of discovering the key parameters governing CS-TENG output. Models have evolved from the simple infinite parallel plate capacitor model of Niu et

al. [57] to the distance-dependent electric field (DDEF) model of Dharmasena et al. [59] which accounts for the important reality that TENGs are based on finitely sized plates. From the DDEF model, it can be noted that the key parameters for designing a CS-TENG are tribo-charge density, separation distance, thickness of the tribo-layers and material permittivity. The DDEF simulation results show that the output performance increases with increasing separation distance (up to a saturation distance) and decreasing permittivity of the tribo-materials. Analysis of the model also indicates that decreasing the thickness of the tribo-layers is a potential route to boosting CS-TENG performance. The load dependent model (LDM) by Xu et al. [147] then added consideration of surface roughness resulting in the contact force dependent TENG results that have been observed in experiments. The numerical studies for investigating the mechanism of tribo-charge transfer by energy bands for both metal-dielectric and dielectric-dielectric mode material selection were also discussed. The equations for two mode types have been calculated to obtain the key parameters governing tribo-charge transfer. These suggest that the important parameters for tribo-charge transfer are: permittivity of contact materials, material surface states and the differences in material work function. Therefore, among the factors that confer higher TENG performance are materials with a strong triboelectric effect together with low permittivity, but it is challenging to optimize both within a single material. This chapter presented a solution to this challenge by optimizing a low permittivity substrate beneath the tribo-contact layer. Using simulations based on the DDEF model, an optimization scheme has been presented allowing prediction of TENG output for substrates having varying permittivities. Results were simulated over a range of substrate permittivities. The open circuit voltage was found to increase by a factor of 1.6 in moving from PVDF to the lower permittivity PTFE. Two TENG devices have been fabricated with 100 μ m PET and PTFE substrates to compare performance. The experiments confirm that lowering the substrate dielectric constant (i.e. PET to PTFE) raises the open circuit voltage in line with simulation predictions. Finally, an application using the same CS-TENG device to power a LED and switching by a photodetector has been demonstrated.

Chapter IV.

Origin of the contact force-dependent response of triboelectric nanogenerators

4.1 Introduction

Chapter II has reviewed several methods to optimize triboelectric nanogenerator performance. Most of the focus has been on optimizing the material selections [43] and engineering the contact surfaces [137, 206] and most of the work conducted to date has involved relatively low contact forces/pressures (such as with wearables). Output performance depends on a number of factors: materials, contact pressure, surface topography, frequency and separation distance. Surprisingly, the role of some of these aspects is still rather poorly characterized and understood in TENG design. One such example is the role of contact pressure. This chapter investigates exactly why TENG output increases with contact pressure. For the first time, the work characterizes both the electrical and *real* contact area response for a TENG based on random rough surfaces in the high contact pressure regime as well as at low pressures. Surface roughness is known to effect aspects such as the frictional response of surfaces [134], the failure behaviour of materials [135] or the contact stiffness of interfaces [136], but here, we demonstrate how it governs the contact pressure dependent output of TENGs via its influence on the real contact area. The results lead to interesting implications including the ability to use large contact pressures to boost performance without the need for costly surface engineering. A number of publications (Section 2.4) have pointed to the contact pressure dependent response, but its origin is yet to be established. Herein, this chapter investigates the physical mechanism underpinning this behaviour via customised experiments designed to probe the behaviour.

This chapter primarily discusses the following points:

- Origin of the contact force-dependent performance of TENGs
- Concurrent real contact area & electrical output measurement over wide contact pressure range
- Implications for definition & measurement of tribo-charge density and
- Applications of load-dependent behaviour

4.2 Fabrication and experiments

Device fabrication and surface characterization is described in Section 4.2.1. Then two separate tests are described: one to measure TENG electrical output versus contact force (Section 4.2.2) and one to measure TENG real contact area versus contact force (Section 4.2.3).

4.2.1 TENG fabrication and surface characterization

The device used for this study was a conductor-to-dielectric TENG in vertical contact separation mode. Fig. 4.1 shows a schematic. The TENG tribo-contact layers were copper sheet (100% Cu, thickness $50\mu\text{m}$) in contact with polyethylene terephthalate (PET) sheet (thickness $127\mu\text{m}$). The PET is coated with indium tin oxide (ITO) (resistivity $60\ \Omega/\text{sq}$, thickness $0.130\mu\text{m}$, Sigma Aldrich, UK) to form the electrode on the PET side. Device dimensions (active tribo-contact surface) were $2.5\ \text{cm} \times 2.5\ \text{cm}$. Since the study is focused on the role of TENG real contact area, some additional measures were taken to ensure uniform contact conformity between the upper and lower tribo-contact layers. The upper and lower parts of the TENG were both fixed to optical glass plates (using double sided tape). Float glass plates possess both low flatness and low surface roughness ($<0.05\mu\text{m}$). This measure is designed to eliminate any unwanted perturbances arising from substrate roughness and facilitate parallel contact of the tribo-layers. In addition, the lead wires were attached to the electrodes outside the active device area to avoid a bulge affecting the contact area.

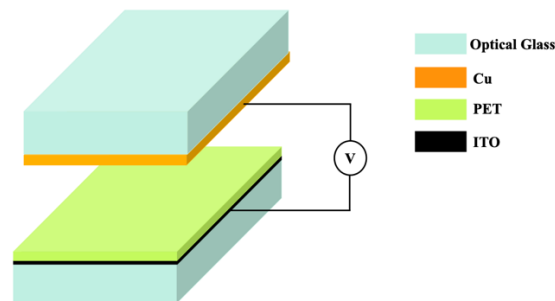


Fig. 4.1. Schematic of the contact separation mode TENG having copper (Cu) in contact with polyethylene terephthalate (PET) [152].

The surface topography of both the Cu and PET surfaces was measured prior to testing

(i.e. pristine surfaces were measured). The Cu surface was scanned using an optical 3D surface profilometer (Alicona InfiniteFocus) and the PET was scanned using an atomic force microscope (AFM) (Dimension Icon, Bruker). The roughness scans for both Cu and PET are shown in Fig. 4.2 and Table 1 reports center-line average roughness, Root Mean Square (RMS) roughness and RMS surface gradient (see Appendix A for explanation of these parameters). Note that the Cu surface is nearly three orders of magnitude rougher than the PET. PET film is transparent, and its root mean square (rms) roughness is in the nano-scale. These two factors make it nearly impossible for the optical profiler to determine accurate roughness measurements. Hence an AFM was used to measure the PET surface.

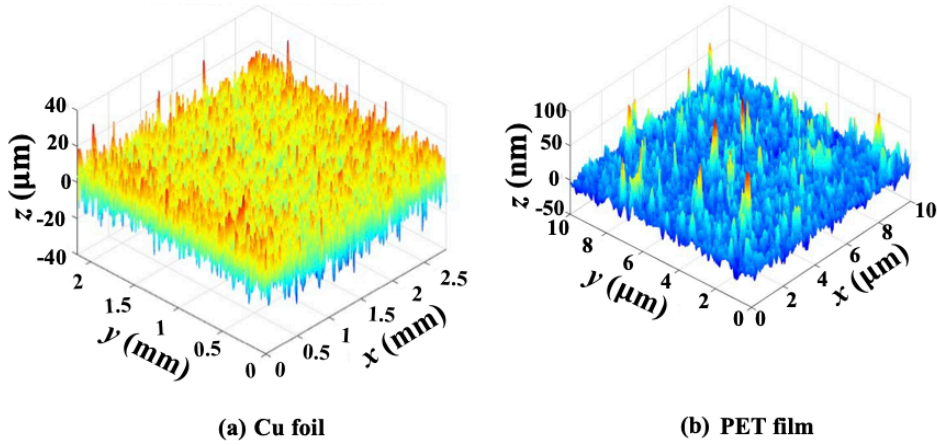


Fig. 4.2. TENG surface topography (a) Cu foil and (b) PET film. Note: the z-axis is in micrometers for Cu and nanometer for PET due to the roughness difference [152].

Table 4.1: Areal surface topography parameters of TENG tribo-contact surfaces (see Appendix A for information on parameters used) [152].

Contact material	Center line average (S_a) (μm)	RMS roughness (S_q) (μm)	RMS surface gradient
Cu foil	4.8	6.1	0.84
PET film	0.0067	0.0095	0.17

4.2.2 TENG Electrical measurements

The setup in Fig. 4.1 (TENG with glass backing plates) was then installed in a custom designed self-aligning test rig as shown in Fig. 4.3a. Fig. 4.3b shows the key detail via a sectional view. The device in Fig. 4.1. (TENG (1) with glass backing plates (2)) is

attached to upper and lower smooth ground metal platforms (3 and 4). Again, because the focus is on contact area, it is critical that the rig is designed to enable parallel contact of the upper and lower TENG tribo-contact surfaces. Indeed, Hong *et al* (2018) [207] found that open circuit voltage dropped by nearly 75% in their study for a misalignment of only 1°. In the rig in this study, rotation of the upper platform (3) is fixed, but the lower platform (4) is free to rotate on a spherical bearing ball (5). Prior to testing, a pre-load is applied to make contact and self-align the surfaces. The alignment is then ‘locked-in’ by tightening the lock screws (6).

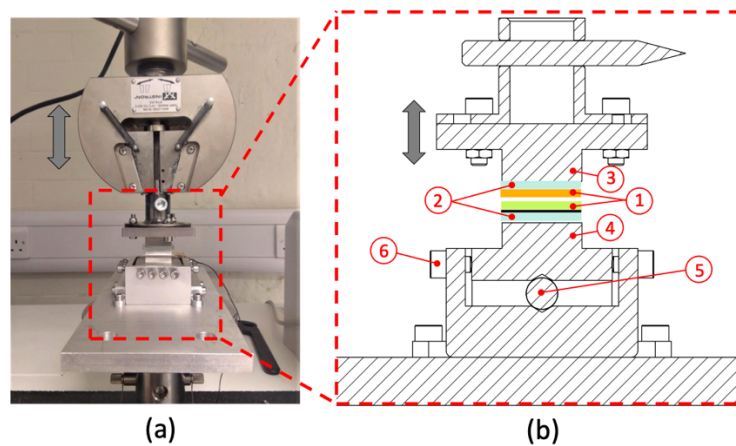


Fig. 4.3. TENG self-aligning test setup: (a) Photo of test rig in mechanical test machine and (b) Sectional view of the test rig. The numbered parts are (1) TENG device (Cu and PET), (2) Glass plates, (3) Upper rig platform, (4) Lower rig platform, (5) Spherical bearing ball and (6) Locking screws [152].

Mechanical oscillation was supplied at 0.5 Hz via a mechanical testing frame (Instron 3367, USA) for contact loads ranging from 20 to 930 N. Note, a low operation frequency ensures the load cell can correctly resolve the peak contact force. This is an important consideration since we are studying the effect of contact force. At high frequencies, it would be important to ensure a given load cell and data acquisition system has the temporal resolution to capture the peak contact force. A key element of the study to be able to characterize the force-dependent response over a sufficiency wide range of applied forces: specifically, from very low forces up to forces required for potential saturation of TENG electrical output. Therefore, for low forces (2–10N), mechanical oscillation was supplied by an electrodynamic shaker system (TIRA, TV 50018, Germany) with a 20 N load cell capacity.

Separation distance was fixed at 2 mm and the open circuit voltage was recorded by an oscilloscope (MSO-X 4154 A, KEYSIGHT, USA). The oscilloscope was connected with an operational amplifier and a voltage divider circuit (resistances of 1 G Ω and 6 G Ω) to ensure that the impedance of the voltage meter setup was much larger than the TENG internal impedance in Fig. 4.4(a) [141]. Details of the short circuit current measurement approach are given in Fig. 4.4(b). Both tribo-contact surfaces were cleaned prior to testing (using acetone and isopropanol initially, then rinsing in RO water and finally blow dried using a nitrogen gun). During the test, the contact load was progressively increased and, at each load value, TENG open circuit voltage and short circuit current was measured after a TENG operation period of 250 cycles in order to ensure equilibrium of tribo-charge generation.

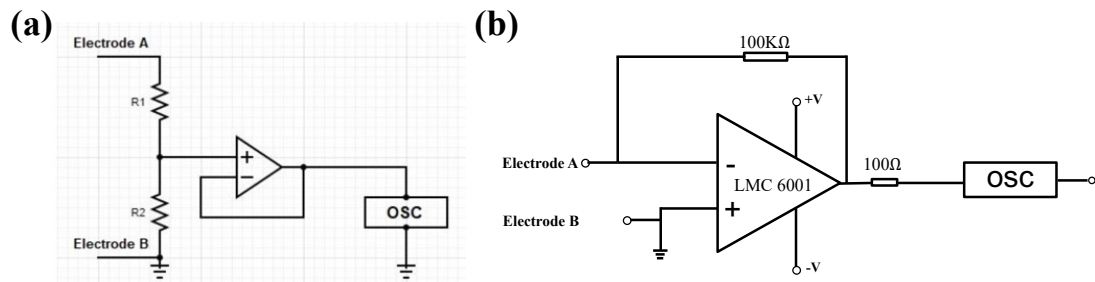


Fig. 4.4: Schematic of equivalent circuit for (a) open circuit voltage measurements, and (b) short circuit current measurements [152].

4.2.3 TENG Contact area measurements

Pressure sensitive film (SPF-A, Pressure Sensors Inc., USA) was used to determine the TENG real contact area. The contact area measurement technique is outlined schematically in Fig. 4.5. The film is placed between the TENG tribo-contact layers (Fig. 4.5a) and contact force is applied via the test rig (Fig. 4.5b). The pressure sensitive film consists of two PET layers: a donor layer and a receiver layer. Both donor and receiver films were cut to 3 cm \times 3 cm (larger than the 2.5 cm \times 2.5 cm TENG area to avoid edge effects). The donor film is coated with a thin layer of micro-capsules and a colour developing layer is coated onto the receiver. Once the local contact pressure exceeds a threshold value, the micro-capsules at these locations break and the capsuled ink transfers to the receiver surface where it reacts with the developer layer to produce

red spots in areas of contact (see Fig. 4.5c). A sample of a tested film is shown in Fig. 4.5d. The lateral resolution of the measurement ($2.6\mu\text{m}$) is determined by the capsule size (specifications for the pressure sensitive film are given in [133]). Following testing, the film is scanned (with 1200 dpi resolution) to produce a digital image for analysis. A MATLAB code is then used to threshold the image to generate binary images and the total area of contact is calculated. The contact area test had to be carried out separately to the electrical measurement test (as the pressure sensitive film will grossly alter the electrical properties of the device). The surfaces were cleaned and aligned (for parallelism) prior to testing. Load was then increased monotonically up to the same load points as for the electrical measurements (i.e. there is no oscillation in the contact area test). At each load point, the pressure sensitive film is removed and a new one is inserted before proceeding to the next load point.

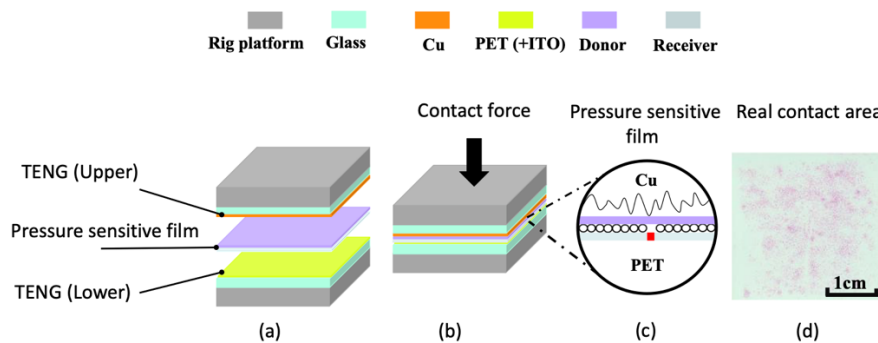


Fig. 4.5: Real contact area measurement using pressure sensitive film: (a) Pressure sensitive film sandwiched between tribo-layers, (b) Compression of layers under contact force, (c) Pressure sensitive film operation and (d) Sample tested film showing areas of contact in red/pink [152].

4.3 Results: electrical output and contact area

Fig. 4.6(a) plots the TENG open circuit voltage signals used for device characterization. A signal is shown for 12 contact forces between 20 and 930 N corresponding to nominal contact pressures of 32–1488 kPa. Note that, since the nominal contact area varies in the TENG literature, it is necessary to use nominal contact pressure (i.e. force/nominal area) to enable comparison. For a given contact force, the peak voltages in Fig. 4.6(a) are almost constant indicating equilibrium of TENG operation. The peak positive voltages are then taken from Fig. 4.6(a) and plotted (together with short circuit current) against contact pressure (and force) in Fig. 4.6(b). In Fig. 4.6(b), open circuit voltage

increases with contact pressure and the upper end of the pressure range here is also sufficient to saturate the open circuit voltage: i.e. beyond about 1176 kPa (753 N), the voltage levels off at around 88 V. This is in-line with previous studies [137, 138, 141, 142] who have noted a similar response. Fig. 4.6(b) also indicates a very similar response for short circuit current. What has not, so far, been elucidated very clearly is exactly why electrical output increases with contact pressure. To answer this question, we turn our attention to the real contact area at the interface.

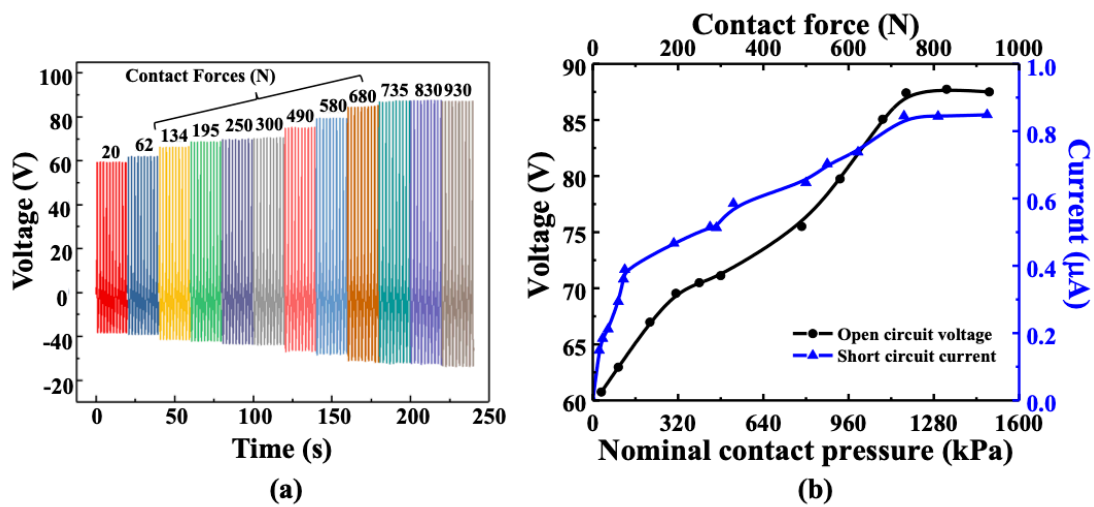


Fig. 4.6. (a) Sample of TENG open circuit voltage signals for increasing contact force and (b) Peak open circuit voltage and peak short circuit current versus nominal contact pressure (and force) [152].

Fig. 4.7(a) shows a sample of the pressure sensitive film results for the 32–1488 kPa contact pressure range. The images on the left are the as-scanned images with the pink spots representing real contact at the TENG interface. The images on the right are the binary images with white representing real contact. The total real contact area A_r is simply the sum of the white areas and the contact area ratio is defined as (A_r/A_n) where A_n is the nominal device contact area of $2.5 \times 2.5 = 6.25 \text{ cm}^2$. Note from Fig. 4.7(a) that contact is spread relatively evenly over the nominal area and not biased towards any particular edge or corner. This is a good indication that the careful measures taken to ensure parallelism of the tribo-contact surfaces in Section 4.1.2 (i.e. glass backing plates and self-aligning contact) have been successful. When the contact pressure is low (32 kPa case in Fig. 4.7(a)), only a few points evenly distributed over the nominal contact area are found to be in solid contact. As the pressure is increased, the area of solid

contact grows. The pressure sensitive film result for the maximum contact pressure case in Fig. 4.7(a) (1488 kPa) is notably different to the 32 kPa result – here a rather large amount of area is in contact. The increase is quantified in Fig. 4.7(b) where contact area ratio is plotted against contact pressure. Notice just how small the real contact area is at low contact pressures: at 32 kPa, the contact area ratio is only 0.0029 (i.e. 0.29%) and, at 99 kPa, only 0.073 (i.e. 7.3%). This is important to bear in mind when we consider that the vast majority of published work on TENGs has been carried out at relatively low contact pressures.

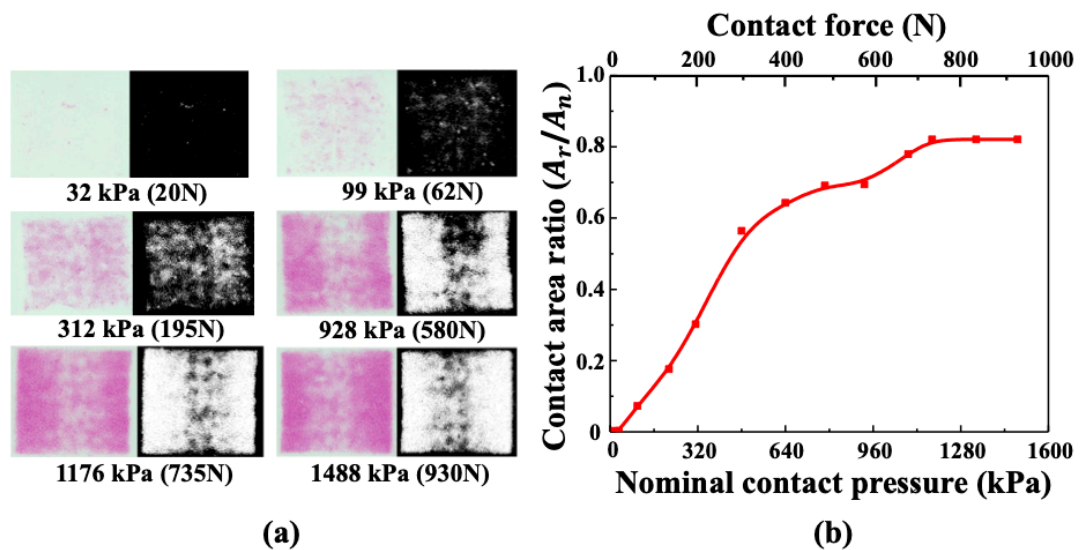


Fig. 4.7: (a) Real contact area as detected by pressure sensitive film with increasing contact pressure showing as-scanned film with pink indicating solid contact (left) and binarized image with white indicating solid contact (right) and (b) Contact area ratio (A_r/A_n) versus nominal contact pressure (and force). Note: the nominal contact patch size in (a) is $2.5 \text{ cm} \times 2.5 \text{ cm}$ [152].

Table 4.2 compares the nominal contact pressure ranges used across a representative selection of studies on contact-separation mode TENGs (with both engineered and non-engineered surface topographies). All of the previous studies in Table 4.2 were conducted at contact pressures below 200 kPa. This means that only the first two cases (32 & 99 kPa) in Fig. 4.7(a) are within this range and we can see from the pressure sensitive film that contact is still rather sparse at these pressures (for the material pair here). Indeed, many of the prevalent TENG applications are only capable of applying very small contact pressures (normal pressures in worn clothing are generally less than

10 kPa [208, 209]) and, although reasonable to a tribologist, it is likely that the TENG community will not have been aware of just how little true contact area is generated under these pressures.

In this work, we go beyond the 0–200 kPa range depicted in Table 4.2 and characterize performance up to a contact pressure of 1488 kPa. To our knowledge, this is the first time a TENG has been characterized over such a wide pressure range covering both low and high pressures. Referring back to Fig. 4.7, we see that contact area grows approximately linearly in the lower pressure regime and then tapers off at higher pressures. Beyond about 1176 kPa (735 N), the contact area ratio saturates at about 0.82. This kind of general evolution of real contact area versus contact pressure has been well observed in the tribology literature [210, 211] and results essentially from the inevitable presence of roughness on even the smoothest fabricated surfaces (i.e. only the extreme peaks of the roughness make contact at first, more peaks then come into contact as the contact pressure is increased until the number of new contact patches and the real contact area saturates – see the roughness scans in Fig. 4.2). However, what is particularly interesting here is the comparison of the contact area measurement with the open circuit voltage and short circuit current measurement.

Table 4.2: Typical nominal contact pressures (force/area) used in TENG studies compared with the present work (final row) [152].

Contact Materials	Surface topography	Contact force (N)	Nominal contact area (cm ²)	Nominal contact pressure (kPa)	Ref.
PDMS & Al/Ag CNF	Engineered	0.5 to 7	2.9	1.7 to 24	[138]
Ag & PDMS	Engineered	4 to 60	4.0	10 to 150	[137, 138]
Ag & PDMS	Engineered	200 to 700	36.0	56 to 194	[140]
PTFE & C-PUF	Engineered	1 to 12	36.0	0.3 to 3.3	[141]
Cu & PDMS	Engineered	18 to 90	9.0	20 to 90	[142]
Al & PDMS	Non-Engineered	40 to 220	25.0	16 to 88	[212]
Glass & PDMS	Non-Engineered	10 to 50	25.0	4 to 20	[213]
PET & PDMS	Non-Engineered	20	25.0	8	[59]
PI & Nylon	Non-Engineered	30 to 60	6.25	48 to 96	[214]
Al & PDMS	Non-Engineered	20 to 40	2.25	89 to 178	[215]
PET & PDMS	Non-Engineered	4.3 to 5.1	3.75	11 to 13.6	[139]
Al & PVDF	Non-Engineered	50	14.44	34.6	[216]
Cu & PET	Non-Engineered	2 to 930	6.25	3.2 to 1488	[133]

Fig. 4.8(a) plots both open circuit voltage and contact area ratio against contact pressure in the same graph. The max open circuit voltage increases from 14.9 V to 87.5 V as the contact area ratio increases from 0.0025 to 0.82. What is particularly interesting are the similarities in form between the two curves. In particular, both open circuit voltage and contact area ratio saturate at about the same value of contact pressure (i.e. around 1176 kPa). A similar trend is seen in Fig. 4.8(b) for short circuit current. This essentially suggests that the electrical output is governed by the real contact area. To gain an insight into how this happens, we recall that the open circuit voltage V_{oc} for the device (parallel plat capacitor model) is given by:

$$V_{OC} = \frac{Q_T x(t)}{A_n \epsilon_0} \quad (4.1)$$

where, $x(t)$ is separation distance, ϵ_0 is the permittivity of air and A_n is the nominal contact area. Now, since these parameters are constant in our experiment, we can conclude that the total tribo-charge Q_T is likely increasing with contact pressure. Assuming tribo-charges can only transfer through the real contact area A_r , and defining σ_T as the areal density of tribo-charge transfer through A_r , we can write:

$$Q_T = \sigma_T A_r \quad (4.2)$$

Taking σ_T as a constant for the material pair, Eqs. (1) and (2) suggest why V_{oc} is dependent on real contact area. The assumption that tribo-charges can only transfer at areas of real contact is reasonable as it has been demonstrated in recent work [63, 144] that contact electrification (via electron tunneling) requires the interatomic distance between atoms across an interface to be within the equilibrium bond distance (i.e. within the repulsive regime). Also, because we are dealing with dielectric materials, this charge should remain localized in the real contact areas. We established in Fig. 4.7 that real contact area in the TENG is highly contact pressure dependent. Thus, taking these two pieces of information together, it should follow that total tribo-charge, and hence TENG electrical output, should be dependent on contact pressure via the real contact area. Indeed, as we have seen, the results in Fig. 4.8 strongly point in this direction as V_{oc} and I_{sc} appear to follow the evolution of real contact area with pressure. Eq. (4.2), of course, assumes that tribo-charges are uniformly distributed and constant over areas of real contact. In fact, the distribution of charges within the real contact area is somewhat unknown and requires significant further study. However, a constant tribo-charge density has generally been assumed in the literature and, in any case, even if it is not constant, the σ_T in Eq. (4.2) can be considered as the net or equivalent value leading to the same total charge. The blue hatched regions in Fig. 4.8 encompass the pressure range (0–200 kPa) from previous literature as depicted in Table 4.2. We can see that a much wider pressure range has been investigated in the present work revealing significant scope for increasing output at higher pressures. For example, at 200 kPa (the max pressure in Table 4.2), the contact area ratio is still less than 0.2, but it reaches 0.82 beyond about 1168 kPa. Note: we have observed gains of 5.8 and 4.9 for V_{OC} and I_{SC} , respectively as A_r was increased from 0.25% to 82%. It is difficult to compare this directly with the effect of other TENG parameters due to the variety of material pairs etc. used across the literature. However, to provide some indicative perspective: It is less than the gains of 50 and 8.5 reported in [59] for V_{OC} and I_{SC} as separation distance was varied from 0.1 to 1 mm. On the other hand, the V_{OC} gain of 5.8 is comparable with V_{OC} gains of 2.6–8 reported with changes in tribo-layer thickness

(0.02–2 mm) in [125, 126], while the I_{SC} gain of 4.9 is of a similar order to I_{SC} gains of 2.4–6 reported with change in frequency (0.5–5 Hz) in [59, 127]. A detailed parametric study would be required to determine a rank order of the sensitivity of TENG output to the different parameters.

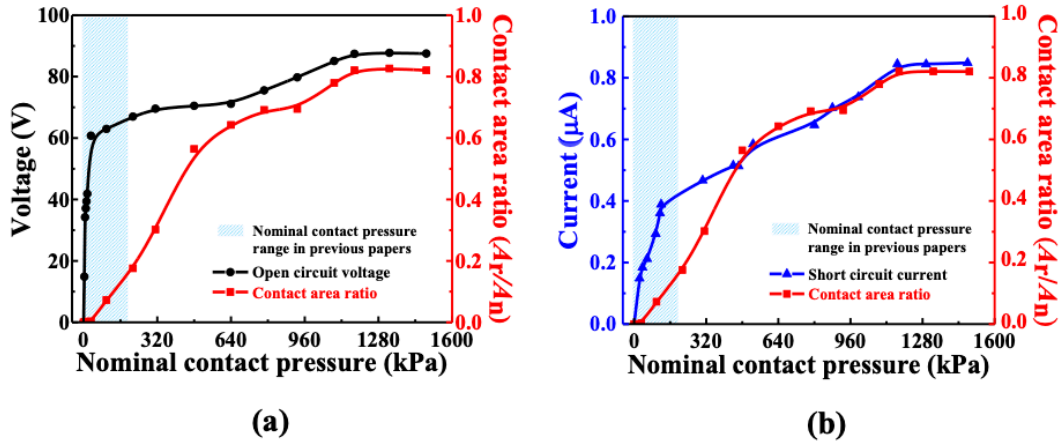


Fig. 4.8: (a) Open circuit voltage and contact area ratio (A_r/A_n) versus nominal contact pressure and (b) Short circuit current and contact area ratio (A_r/A_n) versus nominal contact pressure. The blue hatched regions represent the pressure range in previous literature (as depicted in Table 4.2) [152].

To provide a visual demonstration of the effect of increasing the real contact area (via the contact pressure), 21 LEDs forming the word ‘BEST’ were connected in series with the TENG as the power source (Fig. 4.9(b)). Contact pressure was then increased in the same steps as before and LED performance was imaged via a digital camera at each step. Fig. 4.9(a) illustrates how the LEDs get progressively brighter as the contact pressure (and contact area ratio) increase. Contact pressure increases the real contact area meaning that total charge can increase: this increases voltage and current, and hence, the LEDs become progressively brighter until saturating at points 3 and 4 in Fig. 4.9(a).

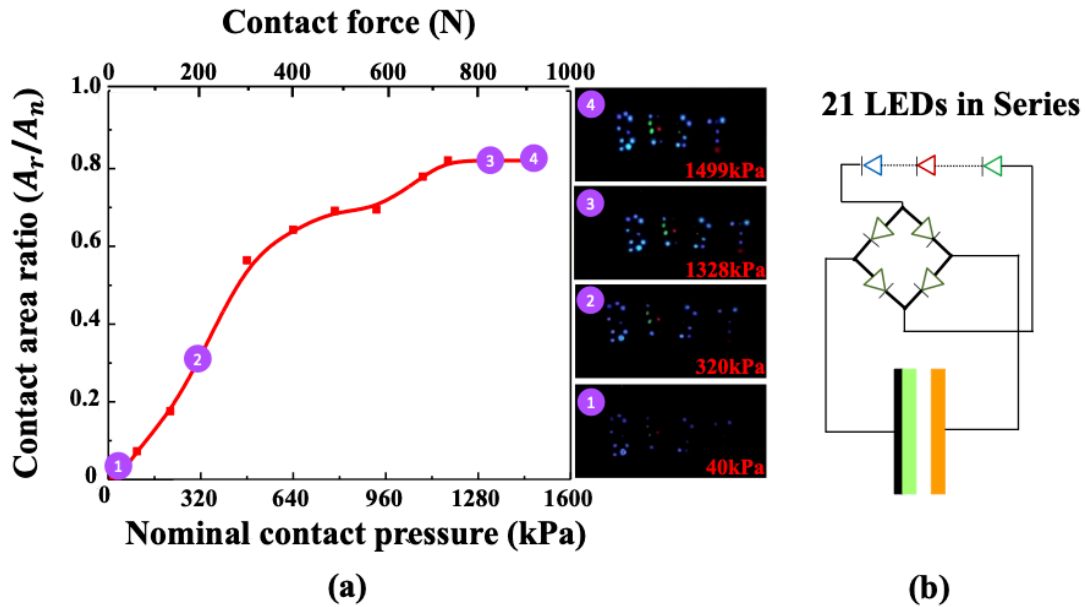


Fig. 4.9: (a) LED array performance versus nominal contact pressure and force (and contact area ratio) and (b) representative energy harvesting circuit. The LED array represents the word “BEST” – the LEDs become progressively brighter as the contact pressure (and contact area) is increased [152].

4.4 Implications and applications of pressure and area dependence

There are a number of important implications that follow from the idea that TENG electrical performance is dependent on a contact pressure-dependent real contact area. The first is that device designers need to carefully account for the real contact area dependence over the design range of contact pressures envisaged for a given device: failure to account for this is likely to result in inaccurate predictions of device performance. While the early TENG models [57, 59] did not account for contact pressure dependence, a recent model by Yang *et al* (2020) [147] accounts for the effect by including the rough surface contact mechanics governing the behavior in a unified TENG model. Material properties, surface topography and contact pressure all influence the real contact area and the model in Xu *et al* (2020) [147] uses input from each of these to predict real contact area, and by extension, electrical output.

The continued boosting of TENG output at higher pressures characterized in the present work also indicates possible new application areas for TENGs – what we might call ‘high pressure applications’. In fact, there are a number of sources of high-pressure cyclic loading in the world around us. Table 4.3 summarizes the typical contact pressures available with a selection of these sources. A particularly suitable and

abundant source is the vehicle wheel-on-surface interaction. For example, in trucks, a contact pressure in excess of 1700 kPa is available at the tyre-road interface (Table 4.3). Here, TENGs positioned either in the tyre or on the road surface could be used to power a variety of sensors for integration with either the truck’s electronic systems or the road infrastructure (e.g. traffic light sensors, warning lights etc.). Similar possibilities occur with automobiles, locomotives and construction & agriculture-based vehicles. Another suitable source is the repeating pressure available from sea waves. Here TENGs can be adapted to take advantage of the higher pressures available for the purpose of generating electricity. For example, pressures in excess of 100 kPa are available from wave interaction with a stationary surface and pressures of almost 9000 kPa have been observed for waves impacting a moving ship hull (Table 4.3).

Table 4.3: Typical contact pressures available in possible high load applications for TENGs [152].

High pressure application	Contact pressure range	Ref
Truck tire vs road	344 to 1723 kPa (range in central 8 cm)	[217]
Locomotive wheel vs rail	700 to 1600 MPa (Peak), 117 to 1167 MPa (Mean)	[218]
Automobile tire vs road	172 to 275 kPa (mean)	[219]
Wave vs tilted slope (1:4)	50 kPa (mean pressure at max peak wave loading)	[220]
Wave vs offshore vertical wall	110 kPa (mean pressure at max peak wave loading)	[221]
Wave vs moving ship hull ('slamming')	2068 to 8963 kPa (mean pressure at peak wave loading)	[222, 223]

Previous literature has focused on boosting TENG output by developing highly engineered surface topographies. Indeed, the present work helps to explain why so many authors [142, 206, 216, 224-226] have noted improvements in TENG performance based on modifications to surface topography – i.e. they were most likely increasing the real contact area. An interesting point to add to this is that, achieving a contact area ratio greater than unity is possible – imagine a hard-sawtooth type surface in contact with a soft counter-surface. The sawtooth surface clearly has an area greater than the nominal area and this can become the interfacial contact area when pressed

into a sufficiently soft counter-surface. However, the present work demonstrates that we can also boost TENG performance with simple non-engineered surfaces. In applications where sufficient pressure is available (Table 4.3), this is a far more cost-effective route. Where contact pressure is limited, softer materials can be easily be chosen so that contact area saturation occurs at lower pressures.

Another important implication relates to the definition and measurement of tribo-charge density. The fact that A_r is generally less than A_n (and especially so at low contact pressures) highlights an important distinction between the tribo-charge density as defined in Eq. (4.2) (i.e. Q_T/A_r) and the conventional definition as Q_T/A_n . It means that tribo-charge density defined as Q_T/A_n cannot be considered to be a fixed quantity (for a material pair), but will depend on the contact pressure and even the surface roughness (via the Q_T generated by the real contact area which is both pressure and roughness dependent). Therefore, there is a need for clarity in the measurement of tribo-charge density essentially to account for the important distinction between the contact pressure dependent A_r and the nominal device area A_n . Current literature does not account for this and there is, therefore, a strong need for further research focused on the measurement of tribo-charge density. Another important consideration here might be whether the interface materials are insulators or conductors. While tribo-charges will remain localized at areas of solid contact for dielectric materials, tribo-charges for a conductor (i.e. in a conductor-to-dielectric TENG) can be expected to distribute over the entire nominal device area. Yet another consideration is how the distribution of real contact area effects output – i.e. would identical real contact areas with differing spatial distribution produce similar electrical output? This question also requires further attention.

Finally, the results demonstrated in Section 4.2 mean that TENGs can be used as effective load and pressure sensors. A careful calibration of output voltage or current versus contact force (and operation within the elastic regime) is essentially all that would be required for a TENG system to report loads and/or pressures. Example applications include pressure/force measurement in vehicle weigh stations, road tyres, shoes and at contact interfaces in vibrating machinery.

4.5 Conclusions

This chapter has investigated the origin of the contact force-dependent performance of TENGs. Experiments were carried out where open circuit voltage and short circuit current were measured together with real contact area under increasing contact force/pressure with identical test conditions for a TENG involving two nominally flat surfaces (PET and Cu) in contact separation mode. Digitized pressure sensitive film was used to directly measure the real contact area – to the authors knowledge, this is the first-time both real contact area and electrical output have been measured between two nominally flat surfaces in a TENG device. Special precautions such as ultra-flat backing plates and a self-alignment facility were shown to ensure the required contact conformity at the interface. Results show that open circuit voltage, short circuit current and real contact area all increase with contact pressure. For low contact pressures, the amount of real contact area is tiny. For example, at 16 kPa (10 N on $25 \times 25 \text{ mm}^2$) the percentage of real contact was only 0.25% of the active device area. Voltage, current and contact area increase roughly linearly at first and later saturate to a converged value at higher contact pressures. Real contact area at saturation (beyond about 1168 kPa) was about 82% - this represents an enormous increase in contact area over the pressure range investigated. Critically, both open circuit voltage and short circuit current saturated at almost the same contact pressure as the real contact area suggesting that electrical output follows the evolution of the real contact area. Recourse to simple TENG theory reveals that, since the key TENG parameters (maximum separation distance, material properties etc.) were constant during the experiment, the total tribo-charge at the interface must have been increasing with contact pressure. The most likely explanation; therefore, is that tribo-charges require real (or solid) contact in order to transfer at an interface (a valid assumption given that recent work suggests that contact electrification can only occur for atom pairs within the equilibrium interatomic bond distance). Therefore, an increasing total tribo-charge (and hence electrical output) is to be expected if real contact area increases with contact pressure. The reason why real contact area increases with contact pressure is simply because nominally flat surfaces, however smooth, inevitably contain random multi-scale surface roughness and the

mechanics of rough surface contact essentially leads to a contact pressure-dependent contact area. Material properties, surface topography and contact pressure all influence the contact area response.

There are several implications of these observations for TENGs. The first is that TENG designers will need to account for pressure dependence over the design range of contact pressures experienced by a device – otherwise predictions of output performance may be inaccurate. This is especially important as most TENG devices operate in the low contact pressure regime where contact area (as we see here) can be a surprisingly small fraction of the nominal area even for very smooth surfaces (and is also very sensitive to contact pressure in this regime). The chapter also essentially explains why so many authors have been able to boost TENG performance by designing novel surface topographies – in most instances, the increase in output is likely due to an increase in real contact area. The distinction between real and nominal contact area leads to another important point relating to tribo-charge density and its measurement. There now needs to be clarity on whether tribo-charge density is calculated based on the real contact area or the nominal active device area and the approach needs to be justifiable for a given application. Pressure-dependence also means that (after a simple calibration) TENGs can be used as force and pressure sensors (e.g. pressure/ force measurement in vehicle weigh stations, road tyres, shoes or even at contact interfaces in vibrating machinery).

Finally, unlike in previous studies, the work characterizes the increasing TENG output well into the high contact pressure regime (up to 1488 kPa). This leads to the ability to use large contact pressures to boost performance without the need for costly surface engineering. In addition, the results demonstrated that a CS-TENG based self-powered pressure sensor can detect a wide range of pressure with high sensitivity, by using the effect of changing A_r between the interface pair with the increase of contact pressure. Note, the pressure sensitive film was used to quantify the A_r/A_n ratio. The findings in this chapter were the impetus to developing the wide range flexible self-powered pressure sensor in Chapter VI. The key outcome of this chapter is illustrated graphically in Fig. 4.10.

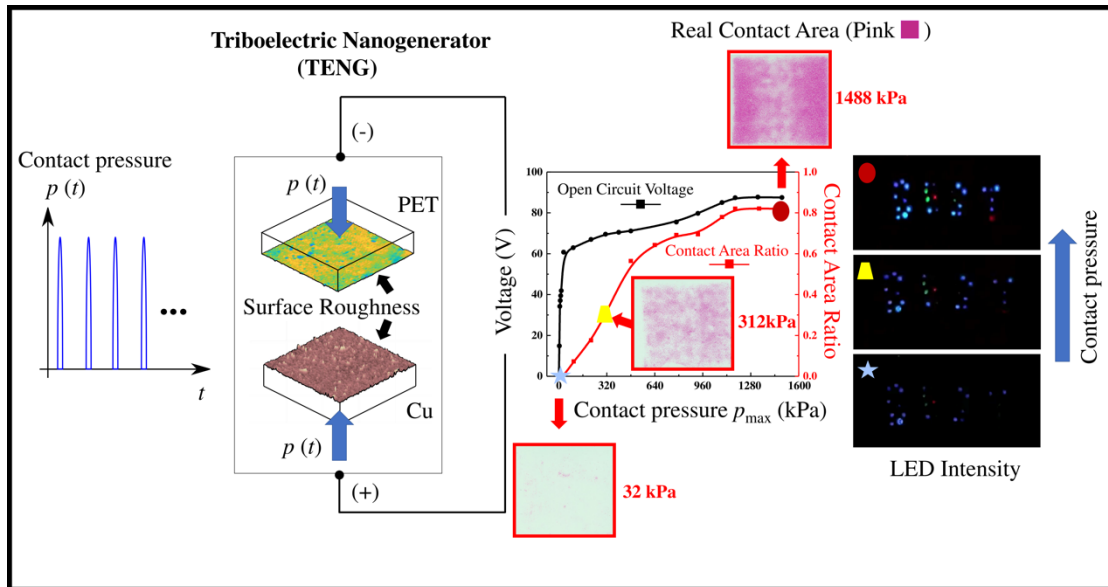


Fig. 4.10: Overall view of the relationship between CS-TENG output and contact pressure [152].

Chapter V

Ferroelectric-Assisted High-Performance Triboelectric Nanogenerators based on Electrospun P(VDF-TrFE) Composite Nanofibers with Barium Titanate Nanofillers

5.1 introduction

A sustainable future of wearable electronic systems depend on assistance from energy harvester and storage devices. Energy harvesters with flexible and/or stretchable form factors are key to the effective use of autonomous systems and have found application in a wide spectrum of areas such as: internet-of-things (IoT), wearable electronics, rehabilitation, respiration monitoring, actuation and motion sensing, air purification and gas sensing, and implantable biomedical devices [111, 150-153, 227-231]. As we have seen, TENGs are flexible, efficient, and cost-effective energy harvesters. Chapter II illustrated how TENGs have been explored in a wide range of applications, including self-powered wearable electronics/sensors, powering of flexible electronics and even for harvesting ocean wave/wind energy.

Chapter II has also reviewed the application of ferroelectric materials to enhance TENG performance. Firstly, the polar β -phase of ferroelectric (FE) (e.g. polymers polyvinylidene (PVDF) and copolymer poly(vinylidene fluoride-co-trifluoroethylene) (P(VDF-TrFE))) have received particular attention due to their permanent polarization of the tribo-contact surfaces. Secondly, to promote β -phase formation, electrospinning is ideal as it would seem to combine uniaxial stretching and electric field poling in a single step [108, 175, 232]. The presence of aligned dipoles in the β -phase of FE polymers results in the enhancement of the spontaneous polarization and hence the surface charge density [233]. High crystallinity can result in a higher dipole alignment in FE polymers. Thus, because PVDF can be treated with lower crystallinity than its copolymer under the same fabrication conditions, β -phase P(VDF-TrFE) was selected as the tribo-negative material in the following experiments. Note, the crystallinity of β -

phase P(VDF-TrFE) could be achieved at 90% by suitable pretreatment. Thirdly, the addition of filler material (e.g. BTO with formula BaTiO_3) into the FE polymer matrix can enhance the formation of a highly polar crystalline β -phase, because of the electrostatic interactions between the nanostructures and the highly aligned dipoles of the FE polymer chains [126, 128, 129, 170, 171]. Finally, as TENG output increases with real contact area (Chapter IV), there is another potential advantage to having a fibrous mat as one of the tribo-surfaces; namely, in certain cases, the flexible fibrous mat may be better able to conform to the topography of the opposing tribo-contact surface.

Therefore, this thesis develops high-performance ferroelectric-assisted TENGs using electrospun fibrous surfaces based on P(VDF-TrFE) with dispersed BaTiO_3 (BTO) nanofillers in either cubic (CBTO) or tetragonal (TBTO) form. TENGs with three types of tribo-negative surface (pristine P(VDF-TrFE), P(VDF-TrFE)/CBTO and P(VDF-TrFE)/TBTO) in contact with PET were investigated and the effect on output is explored. TENGs with P(VDF-TrFE)/BTO have been explored before [126, 128], but only using a spin coated film. Here we explore the potential additional boost to output in using electrospinning to develop a fibrous P(VDF-TrFE)/BTO mat. It is hypothesized that electrospinning might increase dipole alignment due to high applied voltages, but also encourage the formation of a highly oriented crystalline β -phase via uniaxial stretching. The mechanism by which BTO fillers boost output is also explored particularly by comparing the outcomes with CBTO and TBTO. Finally, the ferroelectric-assisted TENG was integrated with a flexible graphene electrode-based supercapacitor to produce a rapid self-charging system. The results demonstrated in this chapter show that this technology can be valuable particularly in wearable applications.

5.2 Experiments

5.2.1 Preparation of Materials

The fibrous (electronegative) surfaces were electrospun from three different solutions: pure P(VDF-TrFE) (Piezotech, France), P(VDF-TrFE) mixed with cubic BaTiO_3 (CBTO, Sigma-Aldrich, UK), and tetragonal BaTiO_3 (TBTO, Sigma-Aldrich, UK) powders. The fabrication steps for the P(VDF-TrFE), P(VDF-TrFE)/CBTO and

P(VDF-TrFE)/TBTO solutions are illustrated in Fig 5.1. A 15 wt% P(VDF-TrFE) solution was prepared by dissolving P(VDF-TrFE) powder in a DMF and acetone (Sigma-Aldrich, UK) mixed solvent (1:1 ratio) for 10h under stirring by a magnetic stir bar at 300rpm and 25C° (see Fig. 5.1(a)). The resulting solution was stirred until the solution was homogeneous and completely transparent. P(VDF-TrFE) and BTO composite solutions were prepared by mixing CBTO or TBTO with the resulting P(VDF-TrFE) solution at 3 wt% (Fig. 5.1(b-c)). Note, 3 wt% was chosen as this led to optimum voltage and current output (See Fig. 5.2). The nanocomposite solutions were then stirred at 300rpm at 25C° for 4hr to disperse the CBTO or TBTO in the P(VDF-TrFE) solution uniformly and form the P(VDF-TrFE)/CBTO and P(VDF-TrFE)/TBTO slurry.

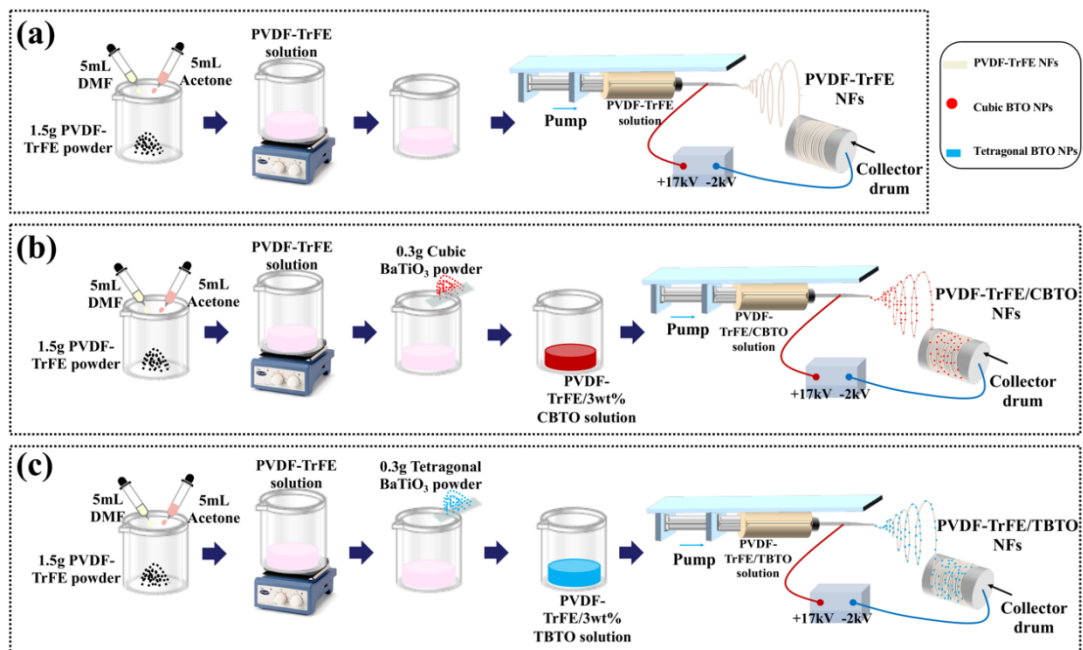


Fig. 5.1: Fabrication procedures for (a) P(VDF-TrFE), (b) P(VDF-TrFE)/CBTO and (c) P(VDF-TrFE)/TBTO NF mats by electrospinning [49].

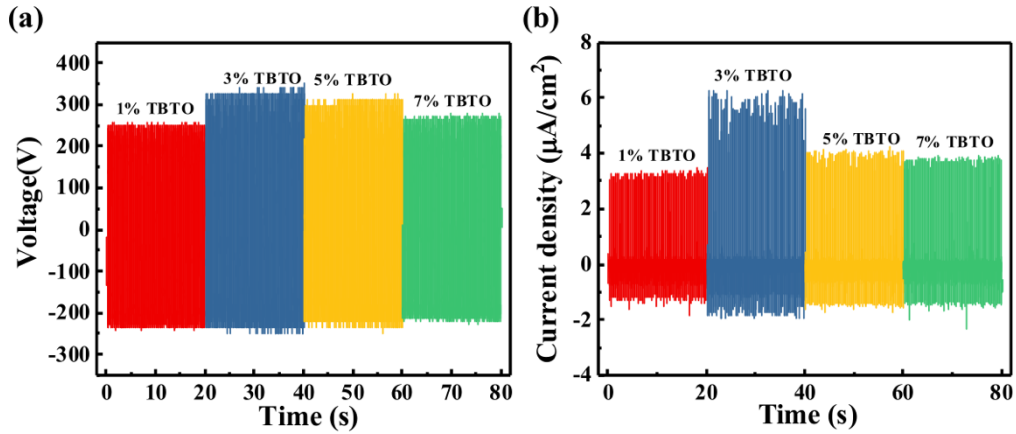


Fig. 5.2: TENG performance versus wt% of TBTO fillers in the tribo-negative P(VDF-TrFE)/TBTO layer showing (a) open circuit voltage and (b) short circuit current density [49].

5.2.2 Electrospinning

Electrospinning of the NFs was conducted using an electrospinning machine. The prepared solutions were filled into a 10mL syringe and connected to a spinneret with a 21G-gauge needle. After that, the electrospinning of solution was executed at a high voltage of 17kV and a flow rate of 0.5 mL/hr with a 15 cm distance between the needle and drum collector, as shown in Fig. 5.1(a-c). The electrospun NFs were collected by a drum collector, which was covered by an aluminum foil (Sigma-Aldrich, UK), with a 2 kV voltage rotating at 1500rpm. All three polymer solutions (P(VDF-TrFE), P(VDF-TrFE)/CBTO and P(VDF-TrFE)/TBTO NFs) were electrospun using the same fabrication parameters at room temperature and humidity. Note, achieving optimum electrospinning parameters for this application is not straightforward as formation of β -phase P(VDF-TrFE) (critical for enabling higher polarization) is sensitive to several parameters including voltage, concentration of P(VDF-TrFE), viscosity and distance between needle and collector. To have NF mats with similar thicknesses, each of the three NF mats were collected on the Al foil for around 2 hrs which produced nanofiber mats with thickness of about 8 μm . The electrospun NF mats covering the Al foil were then cut into small pieces ($4 \times 2.5 \text{ cm}^2$) as shown in Fig. 5.3 and used as the negative tribo-layer. A fixed ITO coated Polyethylene terephthalate (PET) film ($4 \times 2.5 \text{ cm}^2$, Sigma-Aldrich, UK) with a resistivity of $60 \Omega/\text{sq}$ and 0.127 mm thickness was used as the positive tribo-layer for each of the three sample types (to keep the counter-surface

material constant). To avoid a bulge from the electrode lead wires interfering with the contact area, the interface pair positioning was mismatched at a fixed nominal contact area of $2.5 \times 2.5 \text{ cm}^2$ during the measurements (i.e., to allow a free region for attachment of the wires). To measure the pure piezoelectric response, the P(VDF-TrFE)/TBTO nanofiber-based mat was sandwiched between two Al electrodes and encapsulated with a polyimide tape as shown in Fig. 5.4.

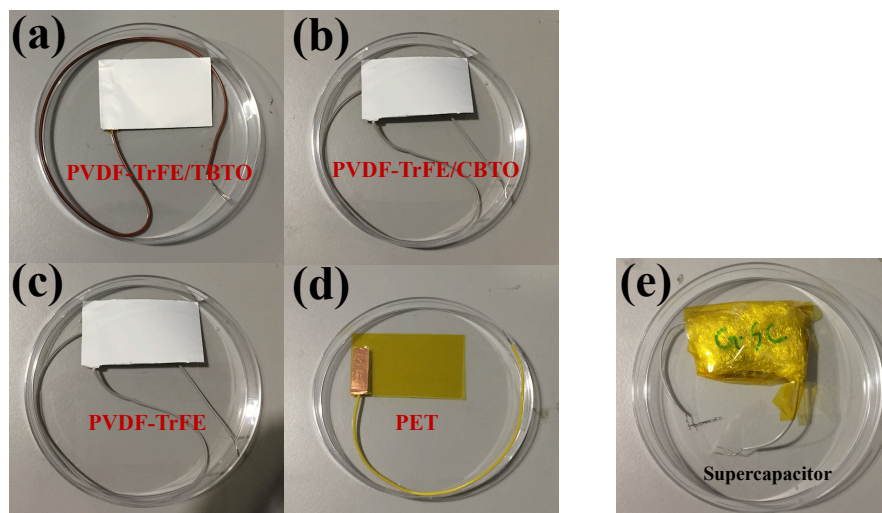


Fig. 5.3: indicates the purely piezoelectric output when a piezoelectric nanogenerators is fabricated for the PVDF-TrFE/TBTO case [49].

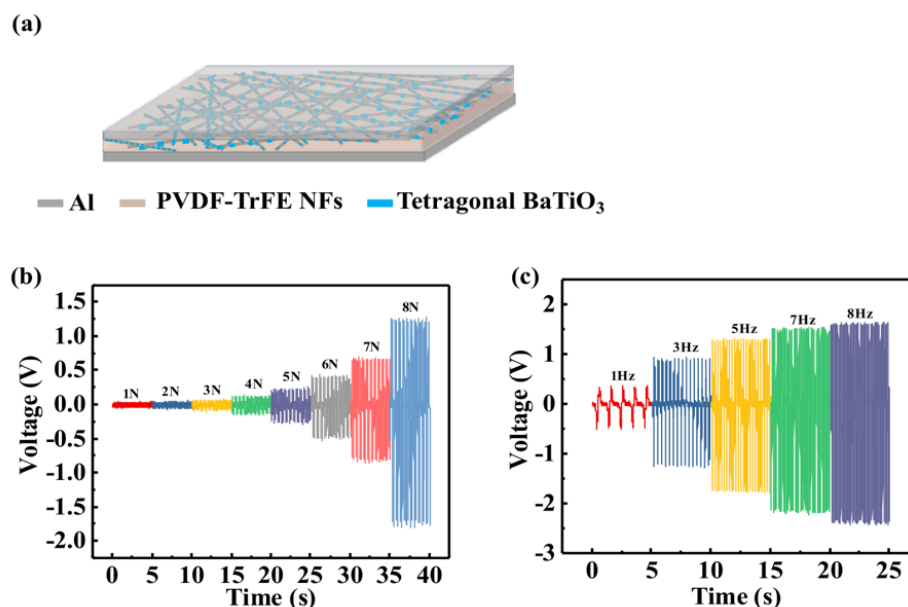


Fig. 5.4: (a) Schematic of equivalent piezoelectric nanogenerator (i.e. piezo only) by PVDF-TrFE/TBTO NFs, (b) output voltage signal with varying applied contact forces and (c) output voltage with varying operation frequencies [49].

5.2.3 Characterization and testing

X-ray diffraction (XRD), employing a PANalytical X'Pert Pro diffractometer with a Cu K α source ($\lambda = 1.541 \text{ \AA}$) was used to characterize crystallinity and the β – phase in the P(VDF-TrFE) matrix for each of the three varieties of electrospun NFs. The surface topography of electrospun NFs and PET surface was measured prior to testing by an optical 3D surface profilometer (Alicona, InfiniteFocus) and an atomic force microscope (AFM) (Dimension Icon, Bruker). A scanning electron microscopy (SEM) was used to describe the surface structure and morphology of the electrospun NF mats. The rig used for TENG testing (normal contact separation mode) is the same as explained elsewhere [147]. Prior to testing, a pre-load was applied to make contact and to self-align the surfaces. The alignment is then 'locked-in' by tightening lock screws. The mechanical oscillation for the TENGs was supplied by an oscillating force (8N with 4Hz frequency) using an electrodynamic shaker system (TIRA, TV 50018, Germany). This produces a corresponding nominal contact pressure of 12.8kPa. Mechanical oscillation was configured with a 2 mm max separation distance (i.e., peak-to-peak amplitude of 2 mm). A 5 min pre-charge time is employed before each set of measurements to ensure equilibrium of tribo-charge generation. The output voltage was recorded by an oscilloscope (MSO-X 4154A, KEYSIGHT, USA) connected to an operational amplifier and a voltage divider circuit to ensure that the impedance of the voltage meter setup was much larger than the TENG internal impedance (See Fig. 4.4a for details). Simultaneously, the oscilloscope was also coupled with an inverting current to voltage converter which consisted of a 100k Ω feedback resistor and a LMC6001 operational amplifier (ultra-input current amplifier) to measure the output current in Fig. 4.4b. When comparing the three TENG devices with the different tribo-negative surfaces (and when testing with different resistive loads) all test parameters (contact pressure, frequency, separation distance etc.) were maintained constant.

5.2.4 Graphene supercapacitor

To demonstrate the self-charging capability of the developed Fe-TENGs, a flexible supercapacitor (FSC) was fabricated using multilayer graphene sheets (GS, Graphene

Supermarket, USA) based on a previous report [234]. In a typical process, the GS film having an area of 3 cm² was used as the current collector and electrode material. At first, the GS film was pasted on flexible polyethylene terephthalate (PET) substrates by polyurethane (PU) resin as the binder. A conducting metal wire was fixed on top of the graphene sheet by silver (Ag) conductive epoxy (RS components, 1863600) for the external connection and insulated with PU coating and dried for 2 hrs at 80C° in a hot air oven. Polyvinyl alcohol (PVA)-phosphoric acid (H₃PO₄) based gel electrolyte was used for the FSC fabrication. The preparation of the gel electrolyte was reported in previous work [235]. Herein, first we dissolved the PVA (10 wt.%) in hot water with continuous stirring followed by the addition of H₃PO₄. A polyester/cellulose blend (Techni Cloth, TX 612) was used as a separator. A schematic representation of the fabricated FSC is shown in Fig. 5.12(a). To charge the supercapacitor, the Fe-TENGs and supercapacitor were coupled by a rectifier circuit which consists of four diodes as shown in Fig. 5.12(b).

5.3. Result and Discussion

5.3.1 TENG performance

Fig. 5.5(a-c) illustrates the structure of the three TENG devices under investigation having the tribo-negative material as pristine P(VDF-TrFE), P(VDF-TrFE)/CBTO composite or P(VDF-TrFE)/TBTO composite (each in contact with PET). Device output is characterized in Fig. 5.5(d-i). Fig. 5.5(d) and Fig. 5.5(e) compare voltages and current densities for each of the three devices at open circuit and short circuit conditions, respectively. Both outputs increase as we move from the pristine P(VDF-TrFE) case to P(VDF-TrFE)/CBTO and to P(VDF-TrFE)/TBTO. The peak positive open circuit voltage V_{oc} increased from 225 V (pristine) to 293V (P(VDF-TrFE)/CBTO) and to 315 V (P(VDF-TrFE)/TBTO), i.e., 1.4 times increase from pristine to P(VDF-TrFE)/TBTO. These voltages are comparable with previous work (Table 2.4). TENGs are high voltage but low current devices and a critical requirement therefore is to boost the current density. In Fig 5.5e, the peak short circuit current density was about 1.95 $\mu\text{A}/\text{cm}^2$ for the pristine case, 5.5 $\mu\text{A}/\text{cm}^2$ for P(VDF-TrFE)/CBTO and a maximum of 6.7 $\mu\text{A}/\text{cm}^2$ for P(VDF-TrFE)/TBTO representing an increase of 3.4 times over the pristine case.

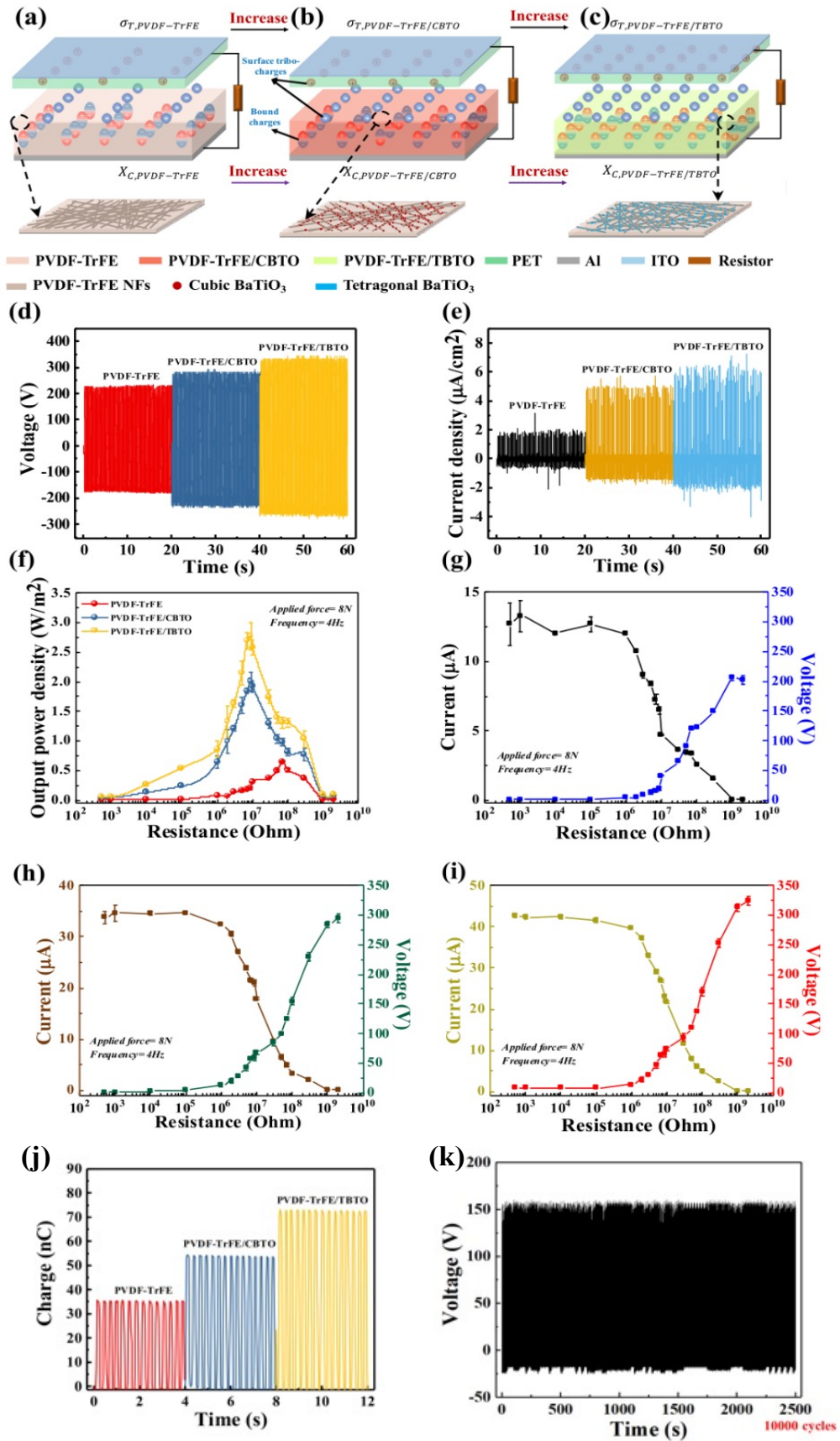


Fig. 5.5: Characterization of device performance. (a-c) illustrate Fe-TENG device structure having negative tribo-surface as: (a) P(VDF-TrFE), (b) P(VDF-TrFE)/CBTO and (c) P(VDF-TrFE)/TBTO (with

PET at the positive tribo-layer in each case). (a-c) also illustrate the role of ferroelectric polarization in affecting the triboelectric surface potential and charge density by indicating how the bias of the bound charges and the level of tribocharges increases as we move to P(VDF-TrFE)/TBTO (Note: XC is degree of crystallinity & σ_T is tribocharge density). Electrical output is characterized in (d-i) for each of the three device types as follows: (d) open circuit voltage, (e) short circuit current density, (f) output power density and (g-i) output current and voltage versus resistive load for (g) pristine P(VDF-TrFE) & PET, (h) P(VDF-TrFE)/CBTO & PET and (i) P(VDF-TrFE)/TBTO & PET. Contact pressure was fixed at 12.8 kPa. (j) transferred charge for three devices. (k) the stability of P(VDF-TrFE)/TBTO & PET device [49].

Additionally, a similar trend is seen in Fig. 5.5(j) for the transferred charges. The transferred charges of three devices have been measured as 35nC, 56nC and 74nC by an electrometer (Keithley 6517B, USA). The transferred charges result is illustrated in Fig. 5.5(j). The resulting boost in the transferred charges by mixing BTO particles into PVDF-TrFE can be attributed to higher crystallinity (and amount) of β -phase and increased permittivity as outlined in the paper. Note, the variation of transferred charges here coincide with trends for open circuit voltage and short circuit current in Fig. 5(d-e). The comparison of our result with previous work on similar materials is given in Table 2.4. For example, with a PVDF-TBTO based device in contact with PA6 in [126] and a P(VDF-TrFE)/TBTO based device in contact with Aluminum in [128]. The former achieved a maximum current density of $3.2 \mu\text{A}/\text{cm}^2$ at a contact pressure of 250 kPa and the latter reported a maximum of $1.25 \mu\text{A}/\text{cm}^2$ at a contact pressure of 98 kPa. The present work has produced significantly higher current density ($6.7 \mu\text{A}/\text{cm}^2$) at much lower contact pressure of only 12.8 kPa. Interestingly, these gains are possible with the counter surface (PET), which is far less tribo-positive than the tribo-positive materials used in above mentioned previous works. In fact, $6.7 \mu\text{A}/\text{cm}^2$ is among the highest values in Table 2.4 where the present work is compared to related work in the literature (i.e. where similar materials were used). The contact pressure is an important factor here as TENG output increases significantly with contact pressure. Therefore, this marked boosting of the current density could be largely attributed to the effect of the electrospinning process used here as previous works used spin-coated films with [128] and without [126] electrical poling. Specifically, the electrospinning here used a higher voltage (17 kV) compared to the poling used in [128] (8 kV). To illustrate this, we have compared our electrospun results to those from equivalent DC poled spin

coated films. Four devices each having non-poled or poled PVDF-TrFE and non-poled or poled PVDF-TrFE/TBTO as the negative tribo-layer (with a fixed PET at the tribo-positive layer) have been fabricated for comparison of output from DC poled and electrospun devices. To execute the polling process, high electric field (25MV/m) is applied on the spin-coated PVDF-TrFE and PVDF-TrFE/TBTO films. Accordingly, the dipoles are aligned with the direction of the external electric field. The increased dipole alignment (i.e. sum of the aligned dipoles) delivers a high surface potential in the films and attracts more surface tribo-charges to maintain the new equilibrium, resulting in enhanced surface tribo-charge density [1].

Fig. 5.6 shows the result of the comparison. For pristine P(VDF-TrFE), output voltage increased 1.5 times going from non-poled to poled and by 2.1 times going from poled to electrospun (Fig. 5.6(a)). The output voltage of the device fabricated by electrospun P(VDF-TrFE)/TBTO is 2.1 times higher than the equivalent poled PVDF-TrFE/TBTO device in Fig. 5.6(b). The higher voltage in electrospinning is likely to encourage enhanced dipole alignment in the P(VDF-TrFE) matrix. Also, uniaxial fiber stretching during the electrospinning process is likely to result in more highly aligned, more crystalline P(VDF-TrFE). These effects are likely to confer higher surface polarity (i.e., higher surface potential) and enable a further boosting of triboelectric charge transfer leading to the higher currents observed. Electrospinning also has the advantage of eliminating the extra poling step as this is now a seamless part of the process. Output power is plotted against resistive load in Fig. 5.5(f) and the corresponding plots of voltage and current versus resistance are shown in Fig. 5.5(g-i). Energy harvesting devices such as TENGs generally present high internal impedance to load circuits and in general, the maximum output power is obtained when the load impedance is matched to that of the harvester. Across the three TENG device variants here, the optimum power occurs in the resistance range of 100 to 500 M Ω . Following the voltage and current trend, peak power increased from about 0.75 W/m² for the pristine P(VDF-TrFE) to about 2 W/m² for P(VDF-TrFE)/CBTO and 2.75 W/m² for P(VDF-TrFE)/TBTO - thus representing 3.2 times increase over the pristine case. The developed Fe-TENG retained approximately 95% of the original output voltage in Fig. 5.5(i) after 10000 cycles of

repeated vibration, as shown in Fig. 5.5(k) – thus the device exhibits good stability.

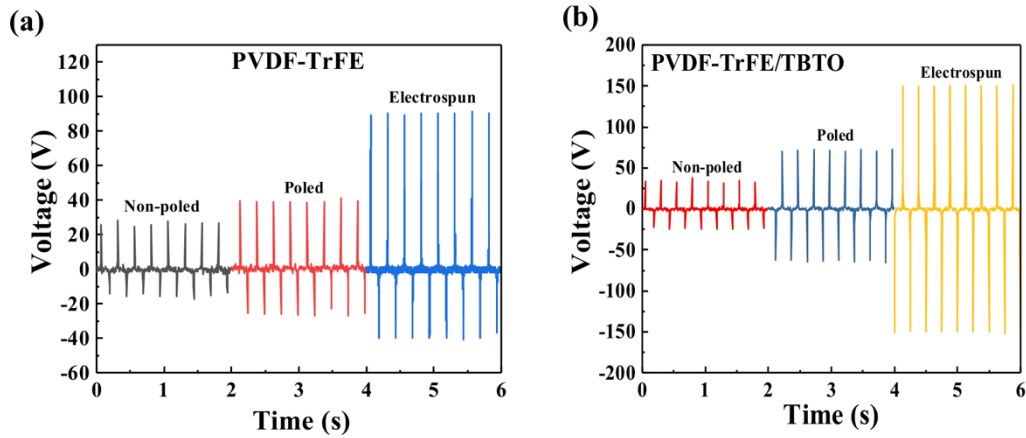


Fig. 5.6: Comparison of output voltage for the device with (a) PVDF-TrFE and (b) PVDF-TrFE/TBTO by non-poling, poling and electrospinning processes [49].

Analyzing the intrinsic properties of the three negative tribo-layer materials can help trace the source of the output differences between the three cases and improve our understanding of the underlying behavior. It has been shown that the intrinsic properties of P(VDF-TrFE) NFs govern the output performance of TENGs. This is because the surface potential of the contact layer is correlated with the degree of crystallinity of the β -phase of the P(VDF-TrFE) NFs [174, 216, 236]. To probe the crystallinity of the NFs, X-ray diffraction (XRD) measurements were performed on all three categories of P(VDF-TrFE) and its composite NF samples (results are shown in Fig. 5.7(a)). From the XRD data, we can see a dominant peak centered at $2\theta=19.96^\circ$ for all three samples, corresponding to the reflection of the crystalline β -phase (110/200) of P(VDF-TrFE). It is important to note that none of the samples showed the non-polar α phase (present at $2\theta = 18.3$). These results also suggest good dispersion of BTO nanoparticles in the P(VDF-TrFE) matrix. Among the three phases of P(VDF-TrFE) namely, alpha, beta and gamma, the β -phase can generate highest surface tribo-charge density because it provides the highest dipolar moment per unit cell (i.e. surface dipole moment) [237, 238]. The characteristic diffraction peak of BTO nanoparticles at $2\theta=22.2^\circ$ is also apparent in Fig. 5.7(a) for the P(VDF-TrFE) composite NFs (in blue for TBTO and black for CBTO). In theory, the XRD diffraction of the tetragonal BTO show peak

splitting at 22.2° corresponding to the (hkl) Miller index (001) and (100), whereas cubic BTO would have a single peak corresponding to (002) [239]. The P(VDF-TrFE)/TBTO NFs diffraction pattern (blue line) exhibits typical characteristics of tetragonal BTO (peak splitting at 22.2° degree) with a single peak at $2\theta = 22.2^\circ$ for the CBTO sample. The cubic phase of BTO belongs to the centrosymmetric crystal class $m\bar{3}m$ and thus, is non-piezoelectric [240].

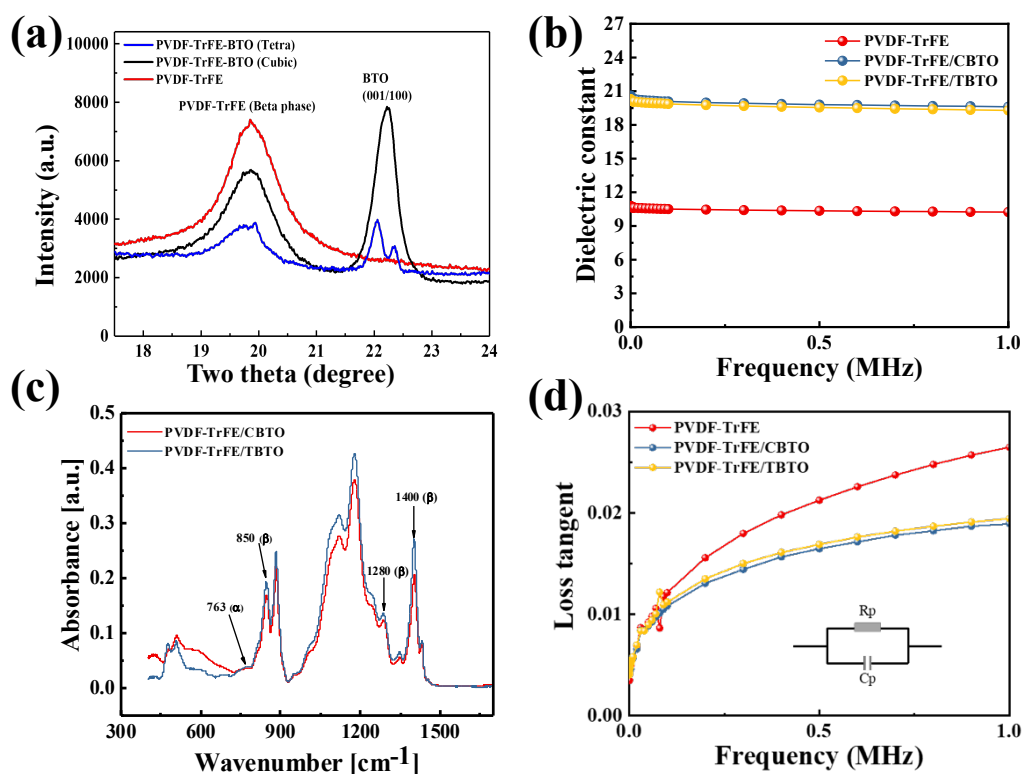


Fig. 5.7: Materials characterization for P(VDF-TrFE) and P(VDF-TrFE)/BTO: (a) X-ray diffraction (XRD) results of P(VDF-TrFE) (red line), P(VDF-TrFE)/CBTO (black line) and P(VDF-TrFE)/TBTO (blue line) with crystalline β -phase (110/200) and XRD patterns of the cubic and tetragonal BTO nanoparticles (001/100); (b) as-measured dielectric properties of the nano-fibrous mats for: P(VDF-TrFE), P(VDF-TrFE)/CBTO, and P(VDF-TrFE)/TBTO. Note: there is little difference in permittivity between CBTO and TBTO nanofillers meaning that permittivity cannot explain the TENG output boost with TBTO (c) : FTIR spectra of P(VDF-TrFE)/BTO composite nanofibers with P(VDF-TrFE)/CBTO (red) and P(VDF-TrFE)/TBTO (blue) and (d) as-measured tangent loss of the nanofibrous mats for: P(VDF-TrFE), P(VDF-TrFE)/CBTO and P(VDF-TrFE)/TBTO [49].

Exploring both CBTO and TBTO in the same work allows us to probe the underlying behavior further. We noted from Fig. 5.5, that voltage, current and power increase progressively as we move from pristine P(VDF-TrFE) to P(VDF-TrFE)/CBTO to P(VDF-TrFE)/TBTO. For example, the current density increases 2.8 times in going

from the pristine case to P(VDF-TrFE)/CBTO. If we then go to P(VDF-TrFE)/TBTO, we notice a further boosting of output to 3.4 times the pristine case. To explain the increases attributable to the BTO nanofillers, there are two key mechanisms: the first (well outlined in [128] and [126]) is that the addition of high permittivity fillers (i.e. the CBTO) dramatically increases the permittivity of the resulting P(VDF-TrFE)/BTO matrix (for example, a factor of 6 to 7 increase in permittivity is reported after addition of CBTO nanofillers to P(VDF-TrFE) [241]). Higher permittivity contact materials increase TENG capacitance, thereby increasing the ability to induce and store more tribo-charge and drive higher currents. Permittivity measurements for the three nanofibrous mat types in this work are given in Fig. 5.7(b). The results show the expected boost in permittivity due to the BTO fillers, and also confirm that CBTO and TBTO result in near identical permittivity values. Therefore, to explain the higher TENG output with TBTO (compared to CBTO), we turn to the second reason and the one we would like to focus on more in this paper.

In a recent work on piezoelectric sensors, the addition of CBTO nanofillers into a P(VDF-TrFE) matrix has been noted to significantly boost β -phase crystallinity by becoming advantageous nucleation sites for the crystalline β -phase [242]. This therefore increased residual polarity and piezoelectric coefficient. Here we explore this role of the BTO nanofillers in increasing crystallinity and how this might be advantageous in the TENG context. The crystalline quality is a parameter that can be determined by calculating the full width at half maximum (FWHM) [243]. Note, a smaller value of FWHM corresponds to the higher β -phase crystallinity. We calculated the FWHM values for pristine P(VDF-TrFE), P(VDF-TrFE)/CBTO and P(VDF-TrFE)/TBTO NFs and these were 0.95, 0.89 and 0.81, respectively. Based on these results, the P(VDF-TrFE)/TBTO NFs have highest crystallinity among the three electrospun materials. We also noted via FTIR Spectroscopy analysis of the P(VDF-TrFE)/BTO that the amount of β -phase was higher for TBTO nanofillers (67%) than for CBTO (54%). Fig. 5.7(c) shows the absorbance spectra for the P(VDF-TrFE)/CBTO and P(VDF-TrFE)/TBTO composite mats obtained by FTIR Spectroscopy. We note the peaks at 850 cm^{-1} , 1280 cm^{-1} and 1400 cm^{-1} corresponding to the β -phase and the α -

phase peak at 763 cm^{-1} . Using the Beer-Lambert law $F(\beta) = \frac{A_\beta}{1.26A_\alpha + A_\beta}$, (A_α and A_β are α -phase and β -phase absorption) the amount of β -phase, $F(\beta)$, for the CBTO and TBTO composites was determined at 54% and 67%, respectively. The existence of β -phase with higher crystallinity and in higher proportions will improve dipole alignment and polarization in the P(VDF-TrFE)/BTO matrix leading to an increase in the surface potential of the tribo-negative contact material. Estimates of surface potential outlined in Fig. 5.8 follow this trend. Estimated surface potential for pristine P(VDF-TrFE) was 133 V and this increased to 189 V with addition of CBTO fillers and was further boosted to 214 V for TBTO fillers.

Fig. 5.8 shows simulated estimates of surface potentials for the TENG devices having each of the three types of tribo-negative nano-fibrous mats (PVDF-TrFE, PVDF-TrFE/CBTO and PVDF-TrFE/TBTO). The finite element multiphysics software COMSOL was used to estimate the surface potential distributions given the key material and surface properties of the tribo-layers and the TENG dimensions and separation distance. The negative tribo-layer consisted of $8 \text{ }\mu\text{m}$ thickness of PVDF-TrFE, PVDF-TrFE/CBTO or PVDF-TrFE/TBTO, while the positive tribo-layer was a $127 \text{ }\mu\text{m}$ thick PET sheet. The lateral dimensions were $2.5 \times 2.5 \text{ cm}^2$ and the max separation distance was 2 mm. The key triboelectric parameter required by the simulation is the tribo-charge density at the interface. This was estimated from the experiments as follows. The voltage drop V across the TENG is:

$$V = \frac{Q_I}{A_n \varepsilon_1} d_1 + \frac{Q_I - Q_T}{A_n \varepsilon_0} x(t) + \frac{Q_I}{A_n \varepsilon_2} d_2, \quad (5.1)$$

were d_1 , $x(t)$ and d_2 are the tribo-positive dielectric thickness, air gap thickness and tribo-negative layer thickness, respectively; ε_1 , ε_0 and ε_2 are the dielectric constants; A_n is the nominal device area and Q_I and Q_T are the total induced charge (on the electrodes) and the total tribo-charge at the interface, respectively. Therefore, the induced charge is related to the tribo-charge in short circuit mode (i.e. $V = 0$) as:

$$\frac{Q_I}{A_n} = \frac{Q_T}{A_n} \times \frac{1}{1 + \frac{\varepsilon_0 d_1}{\varepsilon_1 x(t)} + \frac{\varepsilon_0 d_2}{\varepsilon_2 x(t)}} \quad (5.2)$$

When: $\varepsilon_0 < \varepsilon_1 \approx \varepsilon_2$ and $d_1 \approx d_2 \ll x(t)$ (which is the case here), Eq. (5.2) approximates to:

$$Q_1 \approx Q_2 \quad (5.3)$$

Therefore, we can use the induced charge to approximate the tribo-charge. The induced charge was calculated from the experimental short circuit current I_{SC} using:

$$I_{sc} = \frac{Q_I d_o v(t)}{(d_o + x(t))^2} \quad (5.4)$$

Since COMSOL assumes complete contact over the full device area, the tribo-charge density for the COMSOL simulation was calculated in the average sense as:

$$\sigma_T = \frac{Q_T}{A_n} \quad (5.5)$$

This led to tribo-charge densities of 0.53, 1.4 and 1.7 $\mu\text{C}/\text{cm}^2$ (for PVDF-TrFE, PVDF-TrFE/CBTO and PVDF-TrFE/TBTO, respectively). With the σ_T estimated from experiment, the COMSOL simulated potential distributions are given in Fig. 5.8 for PVDF-TrFE (left), PVDF-TrFE/CBTO (middle) and PVDF-TrFE/TBTO (right). The estimations here confirm that surface potential is increased by the addition of CBTO fillers (by 42.1%) and further increased by the addition of the TBTO fillers (a further 13.2%). As noted, the extra output available with the TBTO nanofillers (compared with CBTO nanofillers) seems to be entirely attributable to the crystallinity effect (as both P(VDF-TrFE)/CBTO and P(VDF-TrFE)/TBTO produce very similar permittivity – Fig. 5.7(b)). We can thus conclude that, in both cases (CBTO and TBTO nanofillers), the TENG enhancement mechanism is a combination of enhancing both permittivity and β -phase crystallinity.

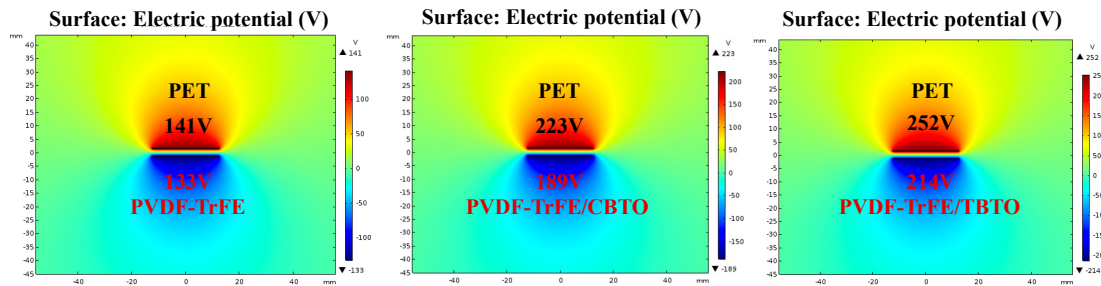


Fig. 5.8: COMSOL simulated potential distributions for PVDF-TrFE (left), PVDF-TrFE/CBTO (middle) and PVDF-TrFE/TBTO (right) devices. Surface potential is clearly highest for the TBTO case [49].

The loss tangent for P(VDF-TrFE)/TBTO, P(VDF-TrFE)/CBTO and P(VDF-TrFE) has been calculated by using: $\tan\delta = \frac{1}{2\pi f C_p R_p}$. Note, the C_p and R_p were tested using a

LCR meter (Keysight E4980, UK). They are the parallel mode capacitance and resistance of the sample as illustrated in Fig. 5.7d. The loss tangent is lower in the P(VDF-TrFE)/BTO composites compared with the pristine P(VDF-TrFE), especially at the higher frequencies in Fig. 5.7(d), because of the glass transition relaxation of the PVDF-TrFE polymer matrix [244, 245]. However, the loss tangent of P(VDF-TrFE)/TBTO and P(VDF-TrFE)/CBTO result in near identical values.

To fully understand how enhanced residual polarization of the P(VDF-TrFE) and its composites boosts TENG output, it is useful to refer to the overlapped electron-cloud (OEC) model [157, 246]. This model describes the process of intrinsic electron transfer between two contact materials. Using the OEC model, Fig. 5.9 schematically illustrates the electron transfer process when each of the three tribo-negative materials are pressed into contact with the tribo-positive PET. In Fig. 5.9, $E_{F, P(VDF-TrFE)}$, $E_{F, P(VDF-TrFE)/CBTO}$ and $E_{F, P(VDF-TrFE)/TBTO}$ represent the Fermi levels of P(VDF-TrFE), P(VDF-TrFE)/CBTO and P(VDF-TrFE)/TBTO, respectively and the greatest energy level difference between these surfaces and PET are represented by ΔE , $\Delta E'$ and $\Delta E''$, respectively.

P(VDF-TrFE) and its composites play the role of the tribo-negative material, accepting electrons from PET during contact electrification. The combination of polarization due to electrospinning and due to enhancements in crystallinity is likely to lead to high dipole alignment resulting in high surface potential. Simultaneously, the presence of bound charges, generated by aligned dipoles, could impact the potential energy [216]. As confirmed by the XRD scans, the P(VDF-TrFE)/TBTO sample has shown higher crystallinity than P(VDF-TrFE)/CBTO and P(VDF-TrFE)/CBTO has shown better crystallinity than pristine P(VDF-TrFE). Accordingly, as shown in Fig. 5.9, the Fermi levels should be in order of $E_{F, P(VDF-TrFE)} > E_{F, P(VDF-TrFE)/CBTO} > E_{F, P(VDF-TrFE)/TBTO}$. As shown in Fig. 5.9(a), when the PET is not in contact with pristine P(VDF-TrFE) NFs, the electron clouds of the materials do not overlap and there is negligible electron transfer between the two atoms. When contact occurs, the potential barrier between them (ΔE) decreases, and the electrons can transfer between the two atoms until their Fermi levels are in equilibrium (i.e. until $E'_{F, PET} = E'_{F, PVDF-TrFE}$). After

incorporating the CBTO/TBTO nanoparticles into the P(VDF-TrFE) matrix, the Fermi level of the negative tribo-layer can be expected to shift downwards due to enhanced surface polarization. As the Fermi level of the PET sheet ($E_{F,PET}$) is fixed in each case, the energy difference is in the following order: $\Delta E < \Delta E' < \Delta E''$. A greater difference in energy levels means more empty surface states of the negative tribo-layer can be filled with electrons from the PET surface (due to the increased differences in work function between the contact materials) and hence higher tribo-charge transfer. After separating the interface pair, the tribo-charge density of a dielectric-dielectric TENG is given by [139]:

$$\sigma_T = \frac{e(\varphi_2 - \varphi_1)}{\frac{1}{N_{s1}} + \frac{1}{N_{s2}} + \frac{2e^2 x_0}{\epsilon_0}} \quad (5.6)$$

Where, $\varphi_{1,2}$ and $N_{s1,s2}$ are the work function and average surface states of the positive and negative tribo-layer, respectively, e is the elementary charge, ϵ_0 is air permittivity, and x_0 is the separation distance. Due to the increased differences in work function and surface states of the negative tribo-layer (i.e., N_{s2}), Eq. 5.6 shows how the tribo-charge density can clearly be boosted. It is important to note that TBTO has a higher dipole moment than CBTO which is non-piezoelectric. Thus, it can be expected to promote higher crystallinity and better dipole alignment similarly to how high dipole solvents have been shown to increase crystallinity and dipole alignment for P(VDF-TrFE) [236]. Thus, in the case of P(VDF-TrFE)-TBTO, the Fermi level of the negative triboelectric material can be expected to further shift to a lower level due to a higher surface potential. Thus, this case is expected to show the largest transfer of electrons between the two materials. This appears to be borne out in the TENG electrical output (Fig. 5.5) and the tribo-charge transfer result in Fig. 5.5(j) where the TBTO composite gives the highest output. The effect of polarized dipoles in affecting the output performance of Fe-TENGs is illustrated schematically in Fig. 5.5.

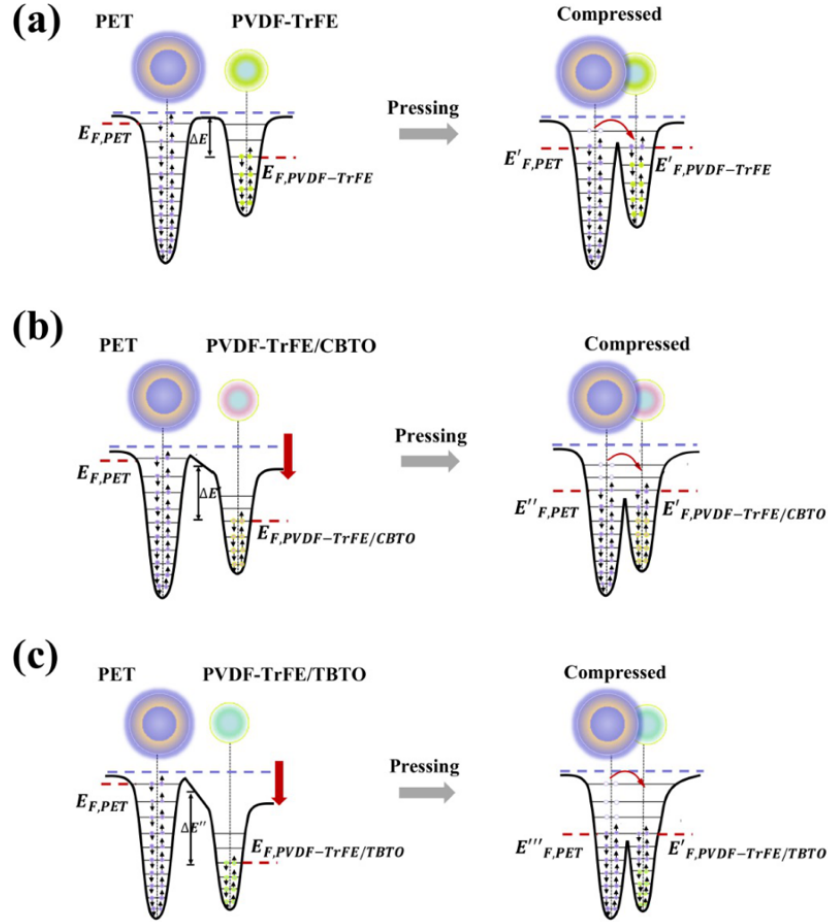


Fig. 5.9: (a) Overlapped electron cloud (OEC) model of electron transfer between interface pairs for (a) P(VDF-TrFE) & PET, (b) P(VDF-TrFE)/CBTO & PET and (c) P(VDF-TrFE)/TBTO & PET [49].

To investigate the contribution of conventional piezoelectricity to the TENG output, we tested a P(VDF-TrFE)/TBTO device in piezoelectric mode only. The result is shown in Fig. 5.4. Here we see that output voltage (1.25 V) at max contact force (8 N) is less than 1% of the corresponding output (315 V) in TENG mode (see Fig. 5.5d). Thus, the TENG devices in this work are referred to as ferroelectric-assisted TENGs rather than hybrid TENGs as the piezoelectric contribution can be considered relatively insignificant. All the above effects (increased permittivity and higher surface polarization) essentially combine in the case of the electrospun P(VDF-TrFE)-TBTO NFs to boost tribo-charge density and deliver the best output performance in the Fe-TENGs device (Fig. 5.5).

5.3.2 Pressure sensitivity, topography and contact area

We turn now to some other key factors that affect the output of these ferroelectric-assisted NF based TENGs. We know that TENG output is generally sensitive to contact pressure for TENGs having solid rough surfaces [133, 147]. Fig. 5.10 shows that this is also the case for the fibrous P(VDF-TrFE) matrix in contact with PET here. At this low-pressure range (3.2 to 12.8 kPa), we observe a roughly linear increase of voltage with pressure. The calculated pressure sensitivities (S) for pristine P(VDF-TrFE), P(VDF-TrFE)/CBTO and P(VDF-TrFE)/TBTO are 27, 28, and 32 V/kPa, respectively. Interestingly, the obtained sensitivity value for P(VDF-TrFE)/TBTO ($S = 32$ V/kPa) is higher than previously reported for TENG-based pressure sensors [77]. As expected, the P(VDF-TrFE)/TBTO plot shows higher voltages than P(VDF-TrFE)/CBTO and the P(VDF-TrFE)-CBTO plot gives higher voltages than the pristine P(VDF-TrFE) case.

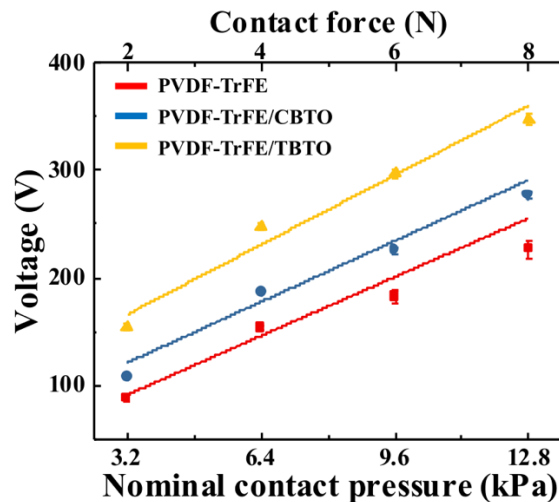


Fig. 5.10: Open circuit voltage versus nominal contact pressure [49].

We know that contact area also affects TENG output (Chapter IV) via the contact pressure and, although the contact pressure was fixed at 12.8 kPa for the electrical results in Fig. 5.5, it is still possible that differences in the topography or elastic modulus of the fibrous (electrospun) surfaces could be responsible for the differences in output already discussed. To evaluate this prospect, we imaged the topography of each surface type and used the boundary element method to estimate the real contact area. The topographies of all three P(VDF-TrFE) based nanofiber mats were measured using an optical profilometer (Infinite Focus, Alicona) prior to testing and the surface roughness

of the PET film was measured by Atomic Force Microscopy (AFM, Bruker, US). The roughness height contours of pure P(VDF-TrFE), P(VDF-TrFE)/CBTO and P(VDF-TrFE)/TBTO NF mats are shown in Fig. 5.11(a-c), respectively. The root mean square roughness (Sq) of the three types of P(VDF-TrFE) mats and the PET film are given in Table 5.1. It is nearly impossible to optically measure the real contact area between these two thin layers using the current test rig, thus, the boundary element method (BEM) [247] is utilized to simulate the linear elastic quasi-static contact between PET and each of the three types of P(VDF-TrFE) based NF mat. Since the sampling area ($0.5 \times 0.7 \text{ mm}^2$) measured by the optical profilometer is much smaller than the nominal contact area of the TENG devices ($25 \times 25 \text{ mm}^2$), the periodic assumption is adopted in the BEM assuming that the sampling area is periodic along two orthogonal scanning directions. Since the Sq of the PET film is approximately 143 times smaller than the average Sq of all three P(VDF-TrFE) NF mats (see Table 5.1), the rough surface contact simulation can be simplified to a rough-on-flat scenario. Note, the roughness of the positive tribo-layer was fixed by reusing the PET sheet. The surface morphology of the electrospun nanofibers for the three cases of tribo-negative layers were characterized using the SEM and are shown in Fig. 5.11(d-f). Each of the three types of NF mats exhibited a completely fibrous structure with uniform distribution of nanofibers and an average fiber diameter of 250 nm. As shown in Fig. 5.11(e) and Fig. 5.11(f), the BTO nanoparticles are inserted into the nanofibers uniformly and particles can be seen on the surface of the fibers. We see from Table 5.1 that the mats with the BTO particles have higher Sq roughness (1.7 and 1.8 μm) than the pristine case (0.57 μm).

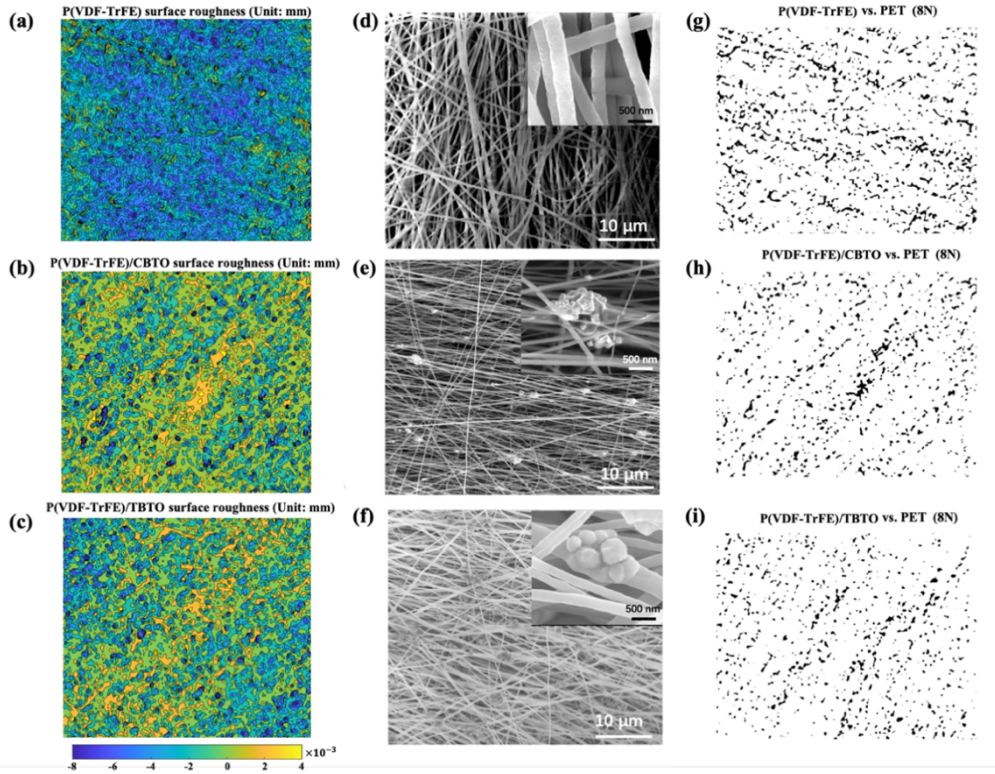


Fig. 5.11: Surface topography and contact analysis: surface height contour plots of (a) P(VDF-TrFE), (b) P(VDF-TrFE)/CBTO and (c) P(VDF-TrFE)/TBTO. SEM images of nanofiber surfaces for (d) P(VDF-TrFE), (e) P(VDF-TrFE)/CBTO and (f) P(VDF-TrFE)/TBTO (inset images at higher magnification). BEM prediction of real contact area (in black) for: (g) P(VDF-TrFE) & PET, (h) P(VDF-TrFE)/CBTO & PET and (i) P(VDF-TrFE)/TBTO & PET. Note how the predicted contact area follows the peaks of the fibers in the fiber orientation [49].

The BEM results for real contact area on the Fe-TENGs interfaces (at 12.8 kPa) are illustrated in Fig. 5.11(g-i) in the form of binary images where black pixels represent contact area. The binary images indicate that: (1) the contact commonly occurs on the higher peaks of the PVDF mats and its composites and, (2) the contact area distributions reflect the orientations of the clusters of high peaks on the rough surfaces. The total real contact area (A_r) is simply the sum of the black areas and the contact area ratio is defined as A_r/A_n where A_n is the (total) sampling area of the rough surface. The BEM calculation for each device is repeated three times using three different rough surface data measurements at different locations over the same P(VDF-TrFE) based NF mats. The BEM predicts a contact area ratio of 10.8% for P(VDF-TrFE), 6.7% for P(VDF-TrFE)/CBTO and 5.6% for P(VDF-TrFE)/TBTO. This corresponds with the surface roughness trend – i.e., the rougher the surfaces, the lesser the contact area.

Considering the electrical outputs now, we note that, although the contact area prediction is highest for pristine P(VDF-TrFE), electrical output is lowest for this case. Also, electrical output is significantly higher for P(VDF-TrFE)-TBTO compared to P(VDF-TrFE) but this is not the case for the predicted real contact areas which were similar (TBTO actually predicting a slightly lower contact area). Thus, we can rule out contact area as an explanation for the trends already observed in the results based on all devices based on fibrous electro-negative material.

Table 5.1: Areal root mean square surface roughness of the tribo-contact surfaces and predicted contact area percentage (BEM) of the Fe-TENGs tribo-contact pair [49].

Negative tribo-layer	RMS Roughness (Sq) (μm)	Average contact area percentage (A_r/A_n $\times 100$)	Positive tribo-layer (PET sheet) RMS Roughness (Sq) (nm)
P(VDF-TrFE)	0.57	10.8%	9.5
P(VDF-TrFE)/CBTO	1.7	6.7%	9.5
P(VDF-TrFE)/TBTO	1.8	5.6%	9.5

5.3.3 Ferroelectric-assisted TENG powered high performance self-charging system

Finally, the ability of the best performing Fe-TENGs (i.e., P(VDF-TrFE)/TBTO & PET) to charge an integrated supercapacitor was investigated. The purpose of demonstrating charging of the supercapacitor with the Fe-TENG device is to show its self-charging ability for applications like wearable electronics. In such applications, a supercapacitor is more suitable compared to a common electrolytic capacitor due to its very high energy density, flexibility and ease of integration. A graphene sheet (GS) based flexible supercapacitor (FSC) [234] with PVA-H₃PO₄ gel electrolyte was used as shown in Fig. 5.12(a). The electronic circuit which connects it with the Fe-TENGs via a rectifier is shown in Fig. 5.12(b). In the self-charging system, the Fe-TENGs will generate the free charges which are stored in the graphene sheet supercapacitor (GSC) through the rectifier. The purpose of the rectifier is to convert the alternating current (AC) output of the Fe-TENGs (see Fig. 5.5(d-e)) to direct current (DC) and hence provide a continuous electrical power supply to store the energy into the GSC.

Fig. 5.12(c) shows rapid charging (~5 min) of the GSC with the Fe-TENGs under

different applied forces with a fixed vibration time (5 min) and frequency (8Hz) followed by a slower self-discharging. It is evident from Fig. 5.12(c) that with increase in contact forces between 2 to 8N (i.e., 3.2 to 12.8 kPa), the maximum output voltage of the SC also increased roughly linearly. This is further evident from Fig. 5.12(d) which shows the variation in maximum output voltage with nominal contact pressures (i.e., contact force/nominal area). It was observed that the voltage could be improved from 0.75V to 1V, when the contact pressure increased from 3.2 to 12.8 kPa. A similar observation can also be seen in Fig. 5.12(e) and Fig. 5.12(f), when the operation frequencies varied between 2 to 10 Hz at a fixed time (5 min) and contact pressure 12.8 kPa (8N) – i.e., the output voltage also increases roughly linearly with frequency. This is due to the increased output current with increasing TENG operating frequency [59] which can be calculated as:

$$I = \frac{dQ}{dt} \quad (5.7)$$

Where, Q is output charge and t is generation period. To increase confidence in the results, three GSC devices with near identical specifications were fabricated and the experiments repeated, with results shown in Fig. 5.12(d) and Fig. 5.12(f). Note that the error in Fig. 5.12(d) and Fig. 5.12(f) is due to expected variation between the three separately fabricated GSC devices rather than instability in a single device.

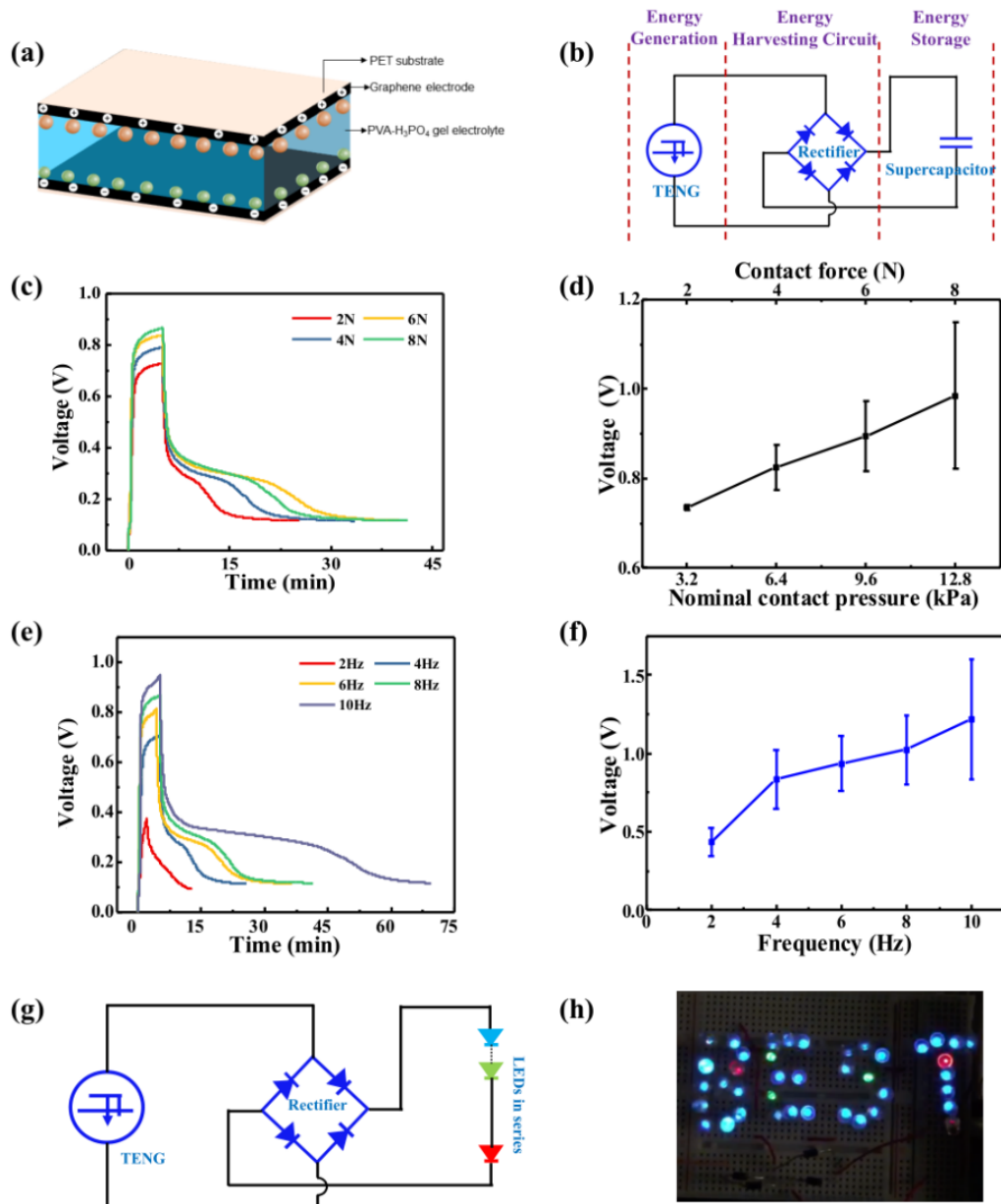


Fig. 5.12. (a) Schematic of graphene electrode based flexible supercapacitor (SC), (b) energy harvesting circuit for self-charging system (i.e. integration with the Fe-TENGs), (c) charging and discharging voltage of SC at different contact forces (frequency of 8Hz), (d) the maximum value of voltage charge into the SC versus nominal contact pressure, (e) charging and discharging voltage of SC by different frequencies (contact pressure 12.8 kPa), (f) the maximum value of voltage charge into the SC versus vibration frequencies, (g) representative energy harvesting circuit of Fe-TENGs for lighting LEDs and (h) photograph of lighted LED array representing the word “BEST” [49].

Table 5.2 summarizes the performance of the present device with the related TENG based self-charging supercapacitor systems in the literature. In the present work, we could charge the GSC to 1.25V voltage within the short time period of about 5 min. This is a considerably lower charging time then the other TENG based supercapacitor

systems in Table 5.2 which vary from 20 to 180 min, thus showing the compatibility of presented devices as an excellent energy harvesting and storage system. For instance, the Polypyrrole paper-based SC charged by a TENG interface pair of PPy/Cellulose paper and Nitrocellulose membrane exhibited a maximum charged voltage value of 1.5V in 167 min at a frequency of 10 Hz (similar to this work) and under much higher contact pressure of 30kPa [198]. In the present work, we were able to charge the SC in a considerably lower charging time with much lower contact pressure, thus indicating the high efficiency of the self-charging system. The rapid charge time is due to high electron mobility in the graphene electrodes which reduce SC impedance as well as the high current being produced by the Fe-TENGs. However, during the self-discharging of the GSC, a rapid drop in voltage to about 0.4V, followed by a slow decrease, is apparent (Fig. 5.12(c) and Fig. 5.12(e)). This high drift in potential or fast discharging indicates the low efficiency of charge storing capacity of the graphene electrode. This is because of the low electroactive surface area, low electrochemical activity and hydrophobicity of graphene electrodes [234]. However, this may still be sufficient for wearable applications as often low power sensors (nanowatt to microwatt power range [200-203]) are needed to be powered. The charging of three series connected GSCs to a maximum 2.3V voltage with the presented Fe-TENG devices has also been demonstrated. To demonstrate the high energy harvesting efficiency of the Fe-TENGs supercapacitor system, we have lighted 40 LEDs connected in series forming the word 'BEST' as shown in Fig 5.12g. In this case, the applied contact pressure was 0.8 kPa at a frequency of 8 Hz. The LEDs are bright even at this low contact pressure. Hence the Fe-TENGs/supercapacitor system produces usable output even at low contact pressures such as those available in wearable applications.

Table 5.2: Typical charging performance and charging period for TENG based self-charging systems in the literature as compared with the present work (final row) [49].

TENG interface pair	SC electrode & electrolytes	Pressure (kPa)	Frequency (Hz)	Period (min)	$V_{max,SC}$ (V)	Ref.
C ₄ F ₈ & ITO	Electrode: CNT/paper Electrolytes: PVA/H ₃ PO ₄	-	8	180	0.9	[197]
PTFE & ITO	Electrode: Cu sheet Electrolytes: [BMIM] [BF ₄]/ ETPTA	40	2	20	0.06	[248]
LIG & PTFE	Electrode: LIG Electrolytes: PVA/H ₂ PO ₄	-	-	117	3	[196]
PTFE & Al	Electrode: peptide-Co ₉ S ₈ Electrolytes: KOH/PVA	-	1	167	1.78	[249]
PVDF-HFP & steel	Electrode: CoFe ₂ O ₄ and Fe-RGO Electrolytes: Fe ³⁺ -PAA/KOH	44	3.8	32	1.6	[250]
PPy/Cellulose paper & Nitrocellulose Membrane	Electrode: Polypyrrole Electrolytes: PVA/H ₃ PO ₄	30	10	167	1.5	[198]
P(VDF-TrFE)/TBTO NFs & PET	Electrode: Graphene Electrolytes: PVA/H ₃ PO ₄	12.8	10	5	1.25	This work

5.4 Conclusions

In this chapter, novel ferroelectric-assisted TENGs (Fe-TENGs) were fabricated whereby the tribo-negative surface is based on electrospun P(VDF-TrFE) composite nano-fibrous mats (having the advantageous β -phase) with dispersed BaTiO₃ (BTO) nanofillers in either cubic (CBTO) or tetragonal (TBTO) form. The approach used electrospinning to significantly increase triboelectric output by boosting surface polarization. TENGs with three types of tribo-negative surface were investigated: pristine P(VDF-TrFE), P(VDF-TrFE)/CBTO and P(VDF-TrFE)/TBTO). The tribo-positive surface was smooth PET. Open circuit voltage and short circuit current density increased progressively from the pristine P(VDF-TrFE) case (225 V & 1.9 $\mu\text{A}/\text{cm}^2$) to P(VDF-TrFE)/CBTO (293 V & 5.5 $\mu\text{A}/\text{cm}^2$) and reached a maximum for P(VDF-TrFE)/TBTO (315 V & 6.7 $\mu\text{A}/\text{cm}^2$), representing 1.4 and 3.4 times increase in voltage and current density, respectively. The corresponding optimum power densities were 0.75, 2 and 2.75 W/m², respectively. Accounting for contact pressure, max output ($V_{oc} = 315 \text{ V}$ & $J_{sc} = 6.7 \mu\text{A}/\text{cm}^2$) is significantly higher than for TENGs having spin-coated P(VDF-TrFE)/BTO.

The gain (versus spin-coating and poling) is likely due to enhanced dipole alignment in

the P(VDF-TrFE) matrix owing to the higher applied voltage during electrospinning. Also, uniaxial fiber stretching during electrospinning is likely to produce highly aligned, more crystalline P(VDF-TrFE). These effects are likely to confer higher surface polarity (i.e., higher surface potential). The increase in electrical output with the addition of the BTO particles is partly due to these high permittivity particles boosting the permittivity of the P(VDF-TrFE) as has been noted in previous literature. However, we found a significant output increase in moving from P(VDF-TrFE)/CBTO to P(VDF-TrFE)/TBTO even though these two materials have near identical permittivity. XRD and FTIR Spectroscopy analysis have revealed that TENG output is boosted by enhancing the amount and crystallinity of the β -phase of the P(VDF-TrFE) matrix. Higher crystallinity in the β -phase is likely to further increase dipole alignment and further boost surface potential. The overlapped electron cloud (OEC) model explains how this can then boost TENG performance: higher surface potential increases the energy gap between Fermi levels and thereby increases the amount of tribo-charge transfer. Thus, this work has shown that the addition of BTO particles boosts TENG output, not just by enhancing permittivity, but by enhancing the amount and crystallinity of the P(VDF-TrFE)/BTO matrix – hence the higher output with TBTO. Finally, the chapter developed an efficient self-charging system by integrating the Fe-TENGs with a graphene electrode based flexible supercapacitor. The system is capable of charging to 1.25 V in the notably short time of 5 mins due to high electron mobility in the graphene electrodes and high current output from the Fe-TENGs. This technology can have significant application in wearable electronics where higher output currents and more efficient charging are required from devices.

Chapter VI.

A wide range self-powered flexible pressure sensor based on the triboelectric nanogenerator

6.1 Introduction

From Chapter II, it is clear that one of the major applications of triboelectric nanogenerators (TENGs) is their application as self-powered sensors. Flexible sensors and sensing systems are widely used in numerous applications of information and communication technology (ICT) such as health monitoring [251], electronic skin (e-skin) [252-254], robotics [253, 254], and sensor networks for Internet-of-Things (IoT) [255] etc. to simultaneously record the wide variety of physical, chemical and biological parameters [238, 256-258]. Among the various sensors, the flexible pressure sensors have attracted huge attention since the contact force or pressure forms an important controlling parameter in numerous applications including for the human-machine interface, and controlled robotic movements [160, 255, 259]. As a result, highly sensitive flexible pressure sensors based on capacitive [260, 261], piezoelectric [262], piezoresistive [263] and triboelectric [160] etc. transduction methods have been reported. Most of these sensors are reported for robotics applications and have been developed for tasks requiring pressure measurement in the range (0.1-100kPa) typically experienced by humans in daily tasks [264]. However, there are many other applications, both in the robotics field and outside, where wide-range pressure sensors are needed. For example, the pressure sensors in the sole of a humanoid robot or in the soles of a person's shoes with walking problems should withstand the body weight. Flexible pressure sensors capable of working over a wide range (i.e. low (1-10kPa), medium (10-100kPa) and high (>100kPa)) for static and dynamic pressures for applications, ranging from intra-body pressures to deep sea [265, 266] are much needed. Further, self-powering of sensors is desirable for continuous operation [267]. High precision, low maintenance, self-powering and wide sensing range are some of the key requirements for the next generation sensors [268, 269].

Chapter III discussed the contact force dependent behaviour often observed with TENGs (where output increases with contact force). For instance, some results in the literature simply show a linear variation of electrical output with contact force [139], while others also include a later-stage saturation occurring at higher forces [142]. In Chapter IV, the origin of this behaviour was explored via concurrent measurement of both electrical output and real contact area (A_r) in a TENG (from 3.2kPa to 1.488MPa). The A_r was notably small at low pressures (0.25% at 16 kPa), but increased 328-fold to as much as 82% when it saturated beyond about 1.12 MPa pressure. This means that the magnitude of electrical output signals from TENGs can be correlated with the external pressure leading to TENG based pressure sensors with the additional feature of being ‘self-powered’ [43, 270]. These results suggest that the contact pressure dependence of the real contact area in TENGs can be used as a basis to develop a wide range pressure sensor (up to ~1200 kPa).

In this regard, this chapter has demonstrated TENG based wide-range self-powered sensors by exploiting this real-contact area dependence. A CS-TENG was fabricated using Cu foil and PET film as the general class of non-engineered triboelectric materials (Fig.4.1). The sensitivities at different pressure ranges were calculated from voltage (V) versus nominal pressure plots. Further, we propose that such a device is ideal for self-powered flexible pressure sensing for applications such as detecting the pressure in wearables, e-Skin for soles of humanoid robots to help them walk and stand, and for sensing the impact force for water wave impacts. In addition to this, we demonstrate the potential application of the self-powered pressure sensing technology in two example applications. The fabricated CS-TENG is firstly employed to monitor human body movements including finger tapping and to collect users gait information, and, secondly, for impact force sensing for free-falling objects.

6.2 Characterization of self-powered pressure sensor

Fig.6.1a schematically shows the working principle of a CS-TENG. The obtained V_{oc} , collected by an oscilloscope, is used as the sensing signal for the applied dynamic pressures. Fig. 6.1b plots the output V_{oc} signal from the CS-TENG, corresponding to a

nominal contact pressure of 1176 kPa (735N on an area of 6.25cm²) at a frequency of 0.5Hz. For a given contact force, the peak voltage signal in Fig. 6.1(b) is almost constant indicating equilibrium of TENG operation. The peak positive voltages at different contact pressures are then taken from the V_{oc} signals and plotted against applied contact pressure in Fig. 6.1(c-e). Note, the nominal contact pressure has been separated as three segments, comprising low (1-10kPa), medium-high (10-500kPa) and super high-pressure range (>500kPa). The obtained sensitivities for each of these three pressure regimes are 3.16, 0.023 and 0.031 V·kPa⁻¹, respectively. To the best of the authors knowledge, this is the first time a TENG as a self-powered pressure sensor has been characterized over such a wide pressure range covering both low and super high pressures. Several suitable low to super-high pressure application areas are proposed incorporating TENG based self-powered sensors. Fig. 6.1 also indicates the typical contact pressure available for various applications, including medical diagnosis, road/traffic monitoring and the deep undersea environment. One potential application could be for accurate pressure measurement in ocean and maritime research. The developed pressure sensor can be placed on human-like robotic structures to collect vital information, which could help researchers measure and record deep-sea pressures (up to ~100 m below the sea surface which corresponds to 1.2MPa) [219]. It can also sense a wide range under sea forces to give haptic feedback to control the robot's activity such as grasping objects.

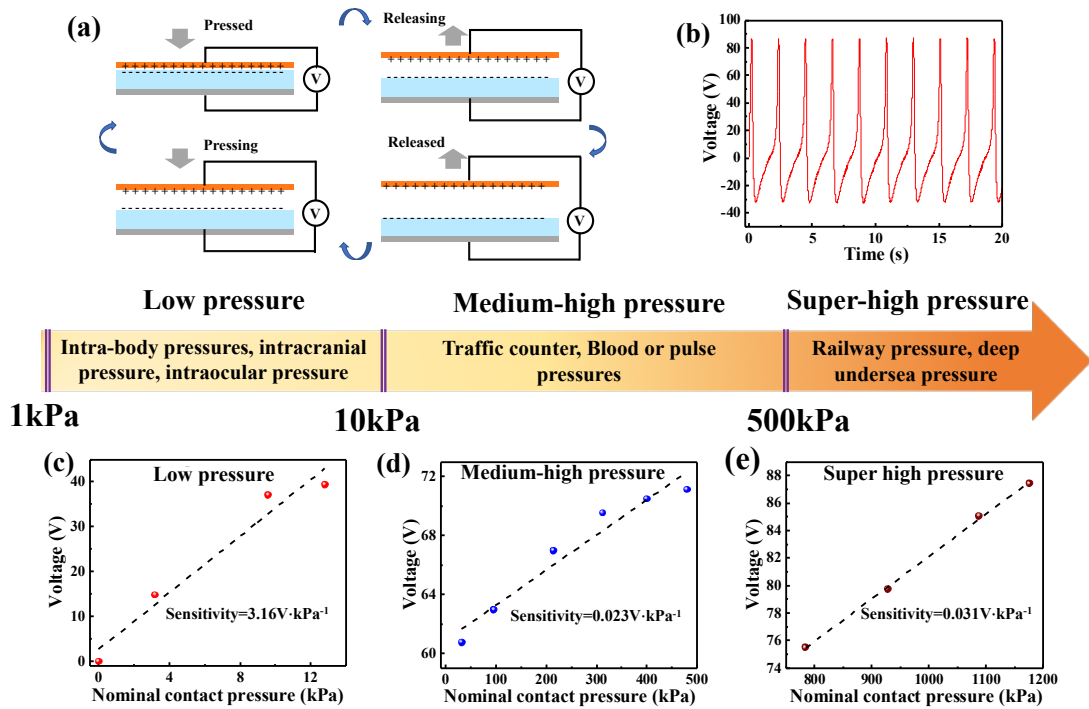


Fig. 6.1: Characterization of TENG based self-powered pressure sensor and its potential applications: (a) working principles of a CS-TENG, (b) a sample of TENG V_{oc} signal under the contact pressure of 1176kPa (735N). (c-e) Voltage output of TENG based self-powered pressure sensor for: (c) low, (d) medium-high pressure and (e) Super high-pressure ranges [27].

6.3 Applications

The fabricated TENG device shows a high response and wide range of pressure detection capability, which can be applied to detect human body movements and impact forces. Cu and PET tribo-contact layers (i.e., same as the device in Fig. 4.1) separated by a gap of 5 mm using a spacer is used to demonstrate the multi-sensing capabilities of the TENG device.

6.3.1 Monitoring of human body movements

The TENG device is demonstrated for human body movement monitoring. As different body parts exert a wide range of pressures, the device here is ideal for recording different physiological signal characteristics.

1) Finger tapping

Fig. 6.2 shows the output voltage signal of the TENG device after being pressed by different numbers of fingers. When the device was pressed by one, two and three fingers, the peak positive output voltage of the TENG was increased from 50 to 65, and to 90V,

respectively (Fig. 6.2). The enhancement in the output voltage is due to the increase in the contact area between the active TENG layers when pressed by increasing numbers of fingers (contact force was kept constant). The electrical output of the self-powered sensor also exhibits a high stability which is clearly evident from the uniform positive voltage output peak in Fig. 6.2. Therein, the positive voltage peaks correspond to the status of pressing the device, and the subsequent negative voltage peaks are corresponding to the releasing state of the device.

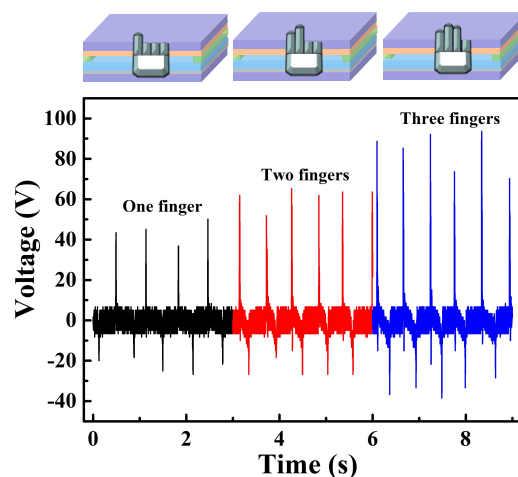


Fig. 6.2: Voltage signal of the pressure sensing TENG when pressed using different numbers of fingers.

2) Gait information collection

The fabricated TENG based self-powered sensor was integrated under the shoes of different users to collect their gait information. Through the TENG output voltage signal, the gait of the users can be analyzed. According to the working mechanism of TENGs, the positive voltage peaks are when the tribo-layers come into contact due to the applied force on the device and the negative voltage peaks can be detected when the interface pair is releasing. Thus, some preliminary gait characterizations can be obtained by monitoring the output voltage features, including amplitudes of output voltage peaks, the frequency of cycles etc. (Fig. (6.3-6.4)). A variety of people's activities can be monitored by these detected gait features. For example, the frequencies of the output voltage signals are 1Hz, 3Hz and 4Hz which corresponds to walking, jogging, and running, respectively (Fig. 6.3(a-c)). Additionally, there is a 20V negative voltage peaks and a 157V positive voltage peak in Fig. 6.3(d). The negative voltage

peak indicates the people jumping up, and the positive voltage peak corresponds to feet impacting with the ground. Note, the gait information in Fig. 6.3 was collected from a man weighing 80 kg (corresponding to a 1280kPa pressure). Fig. 6.4 indicates a very similar response for the gait information extracted from a 45 kg female (corresponding to a 720 kPa pressure). Comparing the output voltage amplitude in Fig. 6.3 and 6.4, the output under four types of gait conditions from the man is higher than from the woman. This is, of course, because the higher the weight of the person, the greater the contact pressure on the TENG device. The output differences in Fig. 6.3 and 6.4, clearly indicate that this self-powered pressure sensor can detect a wide range of pressures.

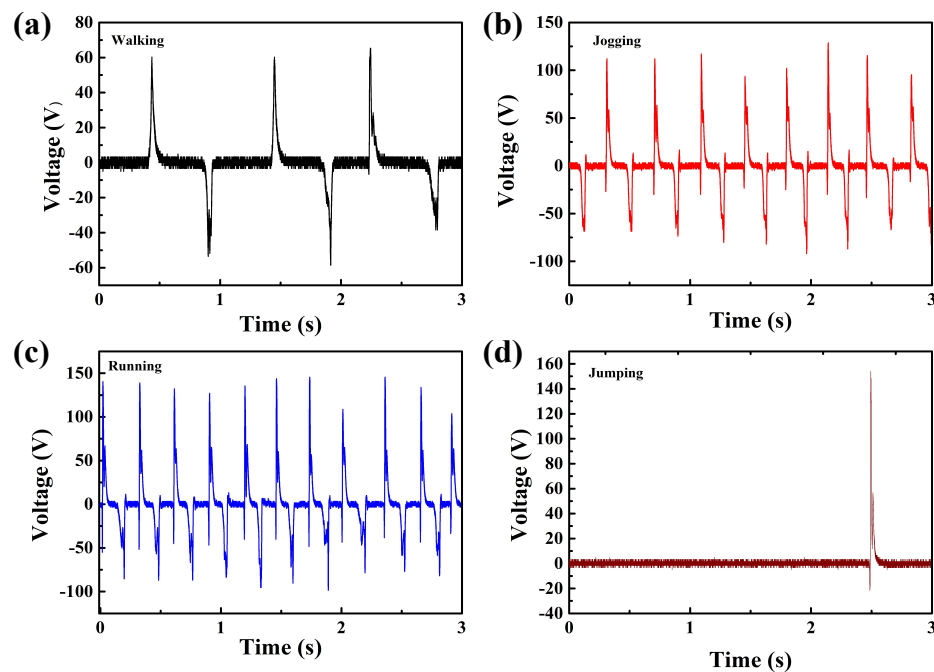


Fig. 6.3: Gait information from a man of 80kg weight collected by the pressure sensing TENG (a) walking, (b) jogging, (c) running and (d) jumping.

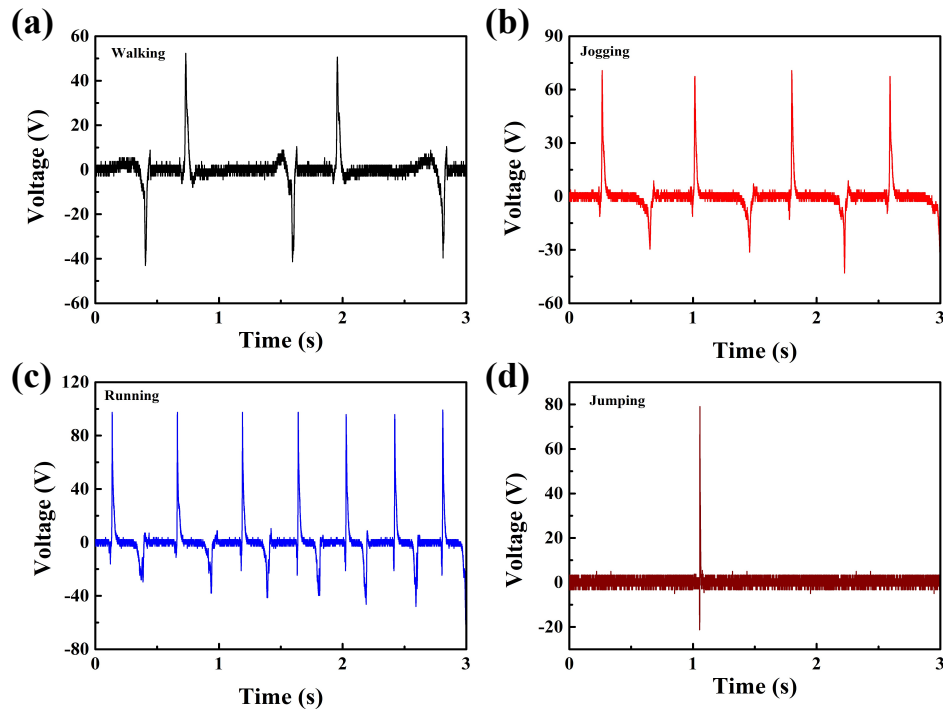


Fig. 6.4: Gait information from a woman of 45kg weight collected by the pressure sensing TENG (a) walking, (b) jogging, (c) running and (d) jumping.

6.3.2 TENG as self-powered impact force sensor for falling objects

The fabricated TENG device also has potential to be used as a self-powered impact force sensor. This is demonstrated by free-falling an object of a fixed mass over the device from different heights, as illustrated in Fig. 6.5(a). The response of the TENG based self-powered impact force sensor is essentially given by the output voltage of the TENG. TENG output voltage exhibits a number of peaks because of multiple rebounding of the object. The high amplitude first peak in Fig. 6.5(b) indicates the first direct impact of the object when dropped from a chosen height and the subsequent voltage peaks are corresponding to the rebounding (i.e., object jumps on the device) motion of the object. The rebounded height of the object is lower than the pre-established height (due to the energy dissipation). Thus, the values of the voltage peaks are lower for subsequent peaks. Fig. 6.5(b) plots the TENG output voltage signals used for observing the impact force sensor characterization. When the object is dropped from a 5cm height, the value of the first positive output voltage peak is 117V. The peak value then increases to 183V, when the preestablished height is adjusted to 14cm. Thus, the output voltage of the TENG is (as expected) related to the dropping height of the object.

The positive voltages for the first peak are then taken from Fig. 6.5(b) and plotted against dropping height in Fig. 6.5(c). As the dropping height increases (5cm to 14cm), a highly linear increase of voltage with dropping height is observed. Note, the calculated height sensitivity (S) is approximated to 7V/cm. According to the law of conservation of energy, the impact velocity and impact force can be calculated by using the dropping height. Therefore, this sensor not only can detect the falling height of the object, but its impact velocity and impact force as depicted in Fig. 6.5(d&e), respectively.

Due to the free-falling motion of the object, the potential energy from the gravity of the object is converted to kinetic energy just before the impact as:

$$\text{Work done by gravity} = \frac{1}{2}mv_{\text{impact}}^2 - \frac{1}{2}mv_{\text{initial}}^2 \quad (6.1)$$

$$\text{Work done of gravity} = mgh \quad (6.2)$$

Where, m is the mass of the object, v_{initial} is the initial velocity of the object, v_{impact} is object impact velocity, and h is the preestablished height. Due to the free-falling motion, the initial velocity of the object is zero. Thus, the impact velocity can be calculated by:

$$v_{\text{impact}} = \sqrt{2gh} \quad (6.3)$$

According to Eq. (6.3), the impact velocity of the object from a height of 5cm, 10.5cm, 13cm and 14cm was calculated. The increase of impact velocity is quantified in Fig. 6.5(d) where impact velocity is plotted against height. The obtained sensitivity between the impact velocity and height is 0.075m/s*cm. Simultaneously, the sensitivity (S') between output voltage (V_o) and impact velocity can be calculated, depending on the regression equation of V_o vs. h and v_{impact} vs. h . S' is the proportionality constant having the value of 92.8m(s·V)⁻¹.

Additionally, the impact force is related to the impact energy and deformation of the impacted object. The impact energy is equal to the work done by gravity from the dropping point to the TENG top surface or the kinetic energy just before the impact. Thus, according to the energy conservation, the impact force can be calculated by the

work-energy theorem [38], as

$$F_{impact} = \frac{\text{Work done of impact force}}{d} = \frac{\frac{1}{2}mv_{impact}^2}{d} = \frac{mgh}{d} \quad (6.4)$$

Where, d is the distance of impacted object deformation. Hence, in this experiment, d should approximate to the separation distance of the TENG. The calculated impact force was calculated by the work done by gravity. The calculated impact forces are plotted against the dropping height in Fig. 6.5(e). For this height range (5cm to 14cm), we observe a linear increase of impact force with dropping height. The extracted sensitivity of 0.4N/cm is 4 times higher than the previously reported TENG based impact force sensors [271]. The sensitivity (S'') between output voltage (V_o) and impact force can be recalculated by the regression equation of V_o versus h and F_{impact} versus h . S'' is the proportionality constant having a value of 17.4V/N.

Furthermore, we demonstrate wireless transfer of the output voltage signal from the TENG. Towards this aim, the AC signal was converted to DC using a microcontroller circuit (FireBeetle ESP32-E) and sent via the Bluetooth Classic protocol (2.4 GHz) to a mobile device. As a proof-of-concept, the finger tapping signals are transferred to a tablet.

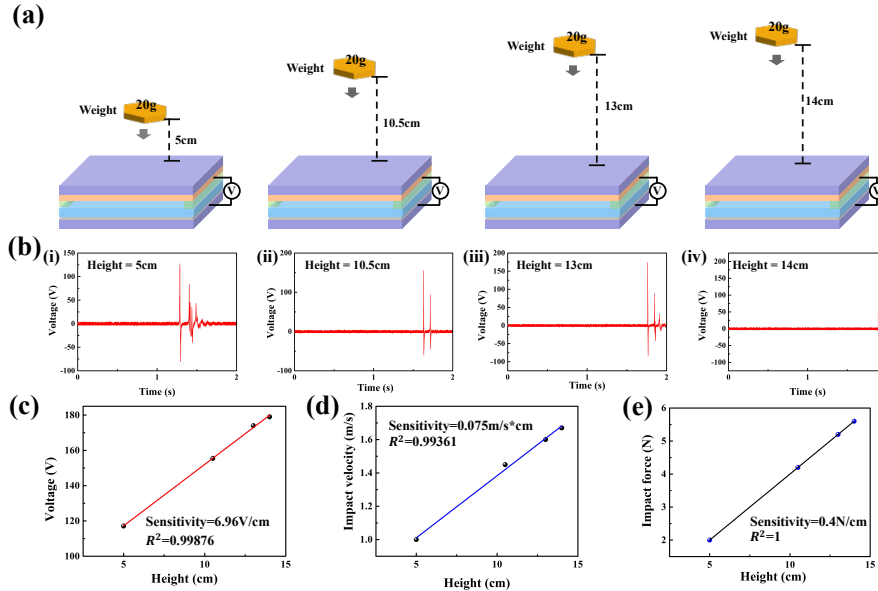


Fig. 6.5: (a) Schematic of free-falling object onto TENG impact sensor from different heights of 5cm, 10.5cm, 13cm, 14cm; (b) output voltage peaks of TENG impact sensor showing the consecutive rebounding of the object from different heights shown in (a); (c) represents the results of output voltage against heights; (d) depicts impact velocity versus fall height and (e) shows the results for impact force against heights.

6.4 Conclusion

The results demonstrate that a CS-TENG based self-powered pressure sensor can detect a wide range of pressures with high sensitivity up to considerably higher pressures than previously considered. To achieve this, the sensor relies on the contact pressure dependence of the real contact area A_r in TENGs. This leads directly to a contact pressure dependent electrical output that can be utilized for pressure sensing. In order to explain the effect, pressure sensitive film was used to quantify the A_r/A_n ratio over a wide range of pressures. The detected pressure sensing range was separated into three regimes comprising: low, medium-high and super high pressure covering a range from 3.2 to 1176 kPa. The associated sensor sensitivities for the three pressure regimes were determined at $3.16\text{V}\cdot\text{kPa}^{-1}$, $0.023\text{ V}\cdot\text{kPa}^{-1}$ and $0.031\text{ V}\cdot\text{kPa}^{-1}$, respectively. Simultaneously, it is proposed that the TENG based sensor has high potential to be used for ocean and robotics research due to its ability to detect high pressures. Finally, we have demonstrated how the fabricated pressure sensing CS-TENG can be applied to a variety of applications. To provide relevant examples, the chapter shows how the sensor can be used to detect finger tapping, collect user gait information and detect impact forces.

Chapter VII.

Conclusion and future perspectives

7.1 Conclusions

The overall aim of this PhD research was to boost the performance of contact and separation mode triboelectric nanogenerators (CS-TENGs) via parameters that can have a significant effect on output. An important goal was also to study how the physics of these parameters effects output. The application of these high performance TENGs in self-powered sensors/systems and self-charging systems was also explored.

TENGs as newly emerging renewable energy harvesters are ideal as the energy supply in autonomous systems and have found application in a wide spectrum of areas such as: internet-of-things (IoT), powering wearable electronics, rehabilitation, respiration monitoring, powering or self-powered actuation and motion sensing, air purification and gas sensing, and implantable biomedical devices. Output power of TENGs is still comparatively low and any increase can have significant implications. This thesis has put forward three key approaches to boosting output: boosting output via control of substrate permittivity, via control of contact area and via use of permanently polarised optimised composite ferroelectric materials.

The theories of CS-TENGs (e.g. device structure and tribo-charge transfer) were studied by simulation and numerical study in Chapter III. These simulations showed that, among the factors that confer higher performance are: materials with a strong triboelectric effect together with low permittivity. However, it is challenging to optimize both within a single material. Therefore, Chapter III presented a solution to this challenge by optimizing a low permittivity substrate beneath the tribo-contact layer. Results were simulated over a range of substrate permittivity. The open circuit voltage was found to increase by a factor of 1.6 in moving from PVDF to the lower permittivity PTFE. Two TENG devices have been fabricated with 100 μm PET and PTFE substrates to compare performance. The experiments confirm that lowering the substrate dielectric constant (i.e. PET to PTFE) raises the open circuit voltage in line with simulation predictions.

In Chapter IV, attention turned to contact area. The review in Chapter II indicated that TENG output tends to be contact force dependent, but its origin had yet to be established. Herein, this thesis shows that the origin lies in the *real* contact area A_r , probed with novel experiments specifically designed for this purpose. The open circuit voltage V_{oc} , short circuit current I_{sc} and A_r for a TENG, having two nominally flat tribo-contact surfaces, were found to increase with contact force/pressure. The A_r was notably small at low pressures (0.25% at 16 kPa) that are typically experienced in wearable applications. However, it increased 328 fold to as much as 82% when it saturated beyond about 1.12 MPa pressure - achievable for something like impact with ocean waves. Critically, V_{oc} and I_{sc} saturated at the same contact pressure as A_r suggesting that electrical output follows the evolution of the A_r . Assuming that tribo-charges can only transfer across the interface at areas of real contact, it follows that an increasing A_r with contact pressure should produce a corresponding increase in the electrical output. These results underline the importance of accounting for real contact area in TENG design to boost their performance, the distinction between real and nominal contact area in tribo-charge density definition, and the possibility of using TENGs as a self-powered pressure/load sensors. Crucially, the results indicate that the large contact pressures, readily available in applications such as road-tyre contact and wave energy, alone could be enough to boost the performance, thus avoiding the need for costly surface engineering to increase A_r .

Chapter V focused on boosting output via careful optimisation of composite ferroelectric materials in fibrous matt form. This entailed the development of high-performance ferroelectric-assisted TENGs using electrospun fibrous surfaces based on P(VDF-TrFE) with dispersed BaTiO₃ (BTO) nanofillers in either cubic (CBTO) or tetragonal (TBTO) form. TENGs with three types of tribo-negative surface (pristine P(VDF-TrFE), P(VDF-TrFE)/CBTO and P(VDF-TrFE)/TBTO) in contact with PET were investigated and output increased progressively from pristine (0.75 W/m²) to CBTO (2 W/m²) and to TBTO (2.75 W/m²). Accounting for contact pressure, the max output ($V_{oc} = 315$ V & $J_{sc} = 6.7$ μ A/cm²) was significantly higher than for TENGs having spin-coated P(VDF-TrFE)/BTO. It is hypothesized that electrospinning

increases dipole alignment due to high applied voltages, but also aids the formation of a highly oriented crystalline β -phase via uniaxial stretching. Essentially, tribo-charge transfer is boosted due to increased surface potential owing to enhanced ferroelectric polarization. P(VDF-TrFE)/TBTO produced higher output than P(VDF-TrFE)/CBTO even though permittivity is nearly identical. Thus, it is shown that BTO fillers boost output, not just by increasing permittivity, but also by enhancing the crystallinity and amount of the β -phase (as TBTO produced a more crystalline β -phase present in greater amounts). Finally, the ferroelectric-assisted TENG was integrated with a flexible graphene electrode-based supercapacitor to produce a self-charging system capable of charging to 1.25 V in just 5 min. These results demonstrate that this technology can be valuable in wearable applications where higher power output, more efficient charging and flexibility are paramount.

In Chapter VI, a CS-TENG-based self-powered pressure sensor has been demonstrated to detect a wide range of pressures with high sensitivity up to considerably higher pressures than previously considered. To achieve this, the sensor relies on the contact pressure dependence of the real contact area A_r in TENGs. In order to explain the effect, pressure sensitive film was used to quantify the A_r/A_n ratio over a wide range of pressures. The detected pressure sensing range was separated into three regimes comprising: low, medium-high and super high pressure covering a range from 3.2 to 1176 kPa. The associated sensor sensitivities for the three pressure regimes were determined at $3.16\text{V}\cdot\text{kPa}^{-1}$, $0.023\text{ V}\cdot\text{kPa}^{-1}$ and $0.031\text{ V}\cdot\text{kPa}^{-1}$, respectively. Simultaneously, we propose that the TENG based sensor has high potential to be used for ocean and robotics research due to its ability to detect high pressures. Finally, we have demonstrated how the fabricated pressure sensing CS-TENG can be applied to a variety of applications. To provide relevant examples, the chapter shows how the sensor can be used to detect finger tapping, collect user gait information and detect impact forces.

In summary, this work has demonstrated how CS-TENG output can be boosted via three distinct approaches: by introduction of a low permittivity substrate, by increase of the real contact area and via use of highly optimised (and polarised) ferroelectric

composites (in this case, P(VDF-TrFE) with barium titanate (BaTiO_3) fillers). The physical understanding developed in relation to these will be valuable in helping to optimise performance in future TENG design work. One avenue for future work would be to attempt to combine each of these optimisations into a single TENG design. Further possibilities for future work are discussed next.

7.2 Future perspectives

The emphasis of this multidisciplinary study was to provide methods to optimize contact and separation mode triboelectric nanogenerator (CS-TENG) performance. However, there are several key areas where additional studies are required to address, improve and further develop the conclusions in this thesis. An effective method to measure the real contact area (A_r) of CS-TENG by pressure sensitive film has been demonstrated in Chapter VI. However, it is believed that the electrical outputs of CS-TENGs can be significantly improved by using micro/nano-structured surfaces for both mating surfaces. Thus, a competitive CS-TENG fabrication method to produce micro/nano-structured surface has already been applied in Chapter V. However, there are many gaps between the nanofibers on the fibrous mat surface. If there is an efficient material surface design to match with these gaps, then the A_r between the interface pair could be greatly increased. Therefore, use of a ZnO nanowire surface to contact with the fibrous mat surface is planned.

The electrospun fibrous mat is more suitable for designing a wearable TENG, because it not only possesses high triboelectric properties, but also good breathability. However, if a polymer film substrate or metal layer electrode is adopted, it will decrease the breathability. Therefore, if the fibrous mat can combine with a fabric film, their wearability will be improved significantly.

One of the applications in TENG based self-charging system has been highlighted in Chapter V. However, due to the low output current of TENG devices, it will take a long time to charge high performance energy storage devices (e.g. lithium battery). A potential method to negotiate this limit is to use a step-down transformer to convert it as high output current and low output voltage. Therefore, a wearable step-down

transformer circuit is planned for future work. Simultaneously, since TENGs depend on mechanical energy input, this places a limitation on its applications. In light of this, there is potential to design hybrid nanogenerators where non-mechanical energy input can also be relied on (e.g. integrating solar cell and TENG or PyENG and TENG).

Appendix A: Surface Roughness Metrology

The definitions, as well as the computing methods relating to the surface metrology parameters used in Table. 4.1 are given here. All of these parameters are easily calculated from surface x, y, z data obtained from surface profilometers at sufficient resolution.

The roughness height, h , is leveled so that $\text{mean}(h) = 0$.

Center line average (CLA) S_a :

$$S_a = \sqrt{\langle |h| \rangle} = \sqrt{\frac{1}{n_x n_y} \sum_{i=1}^{n_x} \sum_{j=1}^{n_y} |h_{ij}|}$$

Root mean square (RMS) roughness S_q :

$$S_q = \sqrt{\langle |h|^2 \rangle} = \sqrt{\frac{1}{n_x n_y} \sum_{i=1}^{n_x} \sum_{j=1}^{n_y} h_{ij}^2}$$

RMS surface gradient S_{dq} :

A continuous form of RMS surface gradient is

$$\begin{aligned} S_{dq} &= \sqrt{\langle |\nabla h|^2 \rangle} = \sqrt{\left\langle \left(\frac{\partial h}{\partial x} + \frac{\partial h}{\partial y} \right)^2 \right\rangle} \\ &\approx \sqrt{\frac{1}{(n_x - 2)(n_y - 2)} \sum_{i=2}^{n_x-1} \sum_{j=2}^{n_y-1} \left[\left(\frac{\partial h}{\partial x} \right)_{ij} + \left(\frac{\partial h}{\partial y} \right)_{ij} \right]^2} \end{aligned}$$

where the partial derivatives are calculated using the central differential scheme:

$$\left(\frac{\partial h}{\partial x} \right)_{ij} = \frac{h_{i+1,j} - h_{i-1,j}}{2\Delta_x}, \quad \left(\frac{\partial h}{\partial y} \right)_{ij} = \frac{h_{i,j+1} - h_{i,j-1}}{2\Delta_y},$$

where Δ_x and Δ_y are the sampling resolution in the x and y directions, respectively.

Appendix B: MATLAB code

```

function dU_dt = myodefunction(t,U)
x1=0.0002;%thickness of surface1
x2=0.00022;%thickness of surface2
w=0.05;%wide of device
e1=28.674*10.^-12; %permmitity of surface1
e2=29.205*10.^-12;%permmitity of surface2
z=linspace(22,0.01,170);%distance
T=40.7;%density of tribo-charge
H=1*(10.^-3);
f=1; %operational frequency
z=(H.*(sin(((2*pi)*f). *t)+((3*pi)/2))))+H;
R=10.^6;
M1=(1/e1).*(((x1+z).*(atan((w)./(2.*(x1+z)).*(sqrt((4.*((x1+z).^2)+2))))))-
((w/2).*(log((sqrt((4.*((x1+z).^2)+2)+1)./(sqrt((4.*((x1+z).^2)+2)-1))))))-
(((x1).*(atan((w)./(2.*(x1)).*(sqrt((4.*((x1).^2)+2))))))-
((w/2).*(log((sqrt((4.*((x1).^2)+2)+1)./(sqrt((4.*((x1).^2)+2)-1)))))));
M2=(1/e2).*(((x2+z).*(atan((w)./(2.*(x2+z)).*(sqrt((4.*((x2+z).^2)+2))))))-
((w/2).*(log((sqrt((4.*((x2+z).^2)+2)+1)./(sqrt((4.*((x2+z).^2)+2)-1))))))-
(((x2).*(atanh((w)./(2.*(x2)).*(sqrt((4.*((x2).^2)+2))))))-
((w/2).*(log((sqrt((4.*((x2).^2)+2)+1)./(sqrt((4.*((x2).^2)+2)-1)))))));
M3=((1/e1)+(1/e2)).*(((x1+x2+z).*(atan((w)./(2.*(x1+x2+z)).*(sqrt((4.*((x1+x2+z).^2)+2))))))-
((w/2).*(log((sqrt((4.*((x1+x2+z).^2)+2)+1)./(sqrt((4.*((x1+x2+z).^2)+2)-1))))))-
(((0).*(atanh((w)./(2.*(0)).*(sqrt((4.*((0).^2)+2))))))-
((w/2).*(log((sqrt((4.*((0).^2)+2)+1)./(sqrt((4.*((0).^2)+2)-1)))))));
M4=((T/pi).*(M1+M2));
P=(M3./pi);
dU_dt=[(1/((w.^2)*(R))).*(M4)-(U.*P)];
end

```

References:

- [1] T. Ahmad and D. Zhang, "A critical review of comparative global historical energy consumption and future demand: The story told so far," *Energy Reports*, vol. 6, pp. 1973-1991, 2020.
- [2] J. Broderick, K. Anderson, C. Jones, and J. Watson, "A review of research relevant to new build nuclear power plants in the UK," 2013.
- [3] G. Crabtree, "Energy: the Next Fifty Years," 2014.
- [4] S. L. Montgomery. "Biden taps the Strategic Petroleum Reserve – What is it? Where did it come from? And does the US still need it?" The conversation. <https://theconversation.com/biden-taps-the-strategic-petroleum-reserve-what-is-it-where-did-it-come-from-and-does-the-us-still-need-it-172473> (accessed).
- [5] "Proved Reserves of Crude Oil and Natural Gas in the United States, Year-End 2019." eia U.S Energy Information Administration. <https://www.eia.gov/naturalgas/crudeoilreserves/> (accessed).
- [6] J. Jurasz, F. Canales, A. Kies, M. Guezgouz, and A. Beluco, "A review on the complementarity of renewable energy sources: Concept, metrics, application and future research directions," *Solar Energy*, vol. 195, pp. 703-724, 2020.
- [7] J. Iannacci, "Microsystem based Energy Harvesting (EH-MEMS): Powering pervasivity of the Internet of Things (IoT)—A review with focus on mechanical vibrations," *Journal of King Saud University-Science*, vol. 31, no. 1, pp. 66-74, 2019.
- [8] L. Mateu and F. Moll, "Review of energy harvesting techniques and applications for microelectronics," in *VLSI Circuits and Systems II*, 2005, vol. 5837: International Society for Optics and Photonics, pp. 359-373.
- [9] A. S. Algamili *et al.*, "A review of actuation and sensing mechanisms in MEMS-based sensor devices," *Nanoscale research letters*, vol. 16, no. 1, pp. 1-21, 2021.
- [10] L. A. Villarruel Mendoza, N. A. Scilletta, M. G. Bellino, M. F. Desimone, and P. N. Catalano, "Recent advances in micro-electro-mechanical devices for controlled drug release applications," *Frontiers in Bioengineering and Biotechnology*, vol. 8, p. 827, 2020.
- [11] A. Dehghani-Sani, E. Tharumalingam, M. Dusseault, and R. Fraser, "Study of energy storage systems and environmental challenges of batteries," *Renewable and Sustainable Energy Reviews*, vol. 104, pp. 192-208, 2019.
- [12] Z. L. Wang, L. Lin, J. Chen, S. Niu, and Y. Zi, *Triboelectric nanogenerators*. Springer, 2016.
- [13] G. Zhu, B. Peng, J. Chen, Q. Jing, and Z. L. Wang, "Triboelectric nanogenerators as a new energy technology: from fundamentals, devices, to applications," *Nano Energy*, vol. 14, pp. 126-138, 2015.
- [14] B. Bera, "Literature review on triboelectric nanogenerator," *Imperial Journal of Interdisciplinary Research (IJIR)*, vol. 2, no. 10, pp. 1263-1271, 2016.
- [15] S. Pan and Z. Zhang, "Fundamental theories and basic principles of triboelectric effect: A review," *Friction*, vol. 7, no. 1, pp. 2-17, 2019.
- [16] S. P. Sukhatme and J. Nayak, *Solar energy*. McGraw-Hill Education, 2017.
- [17] H. J. Goldsmid, *Introduction to thermoelectricity*. Springer, 2010.
- [18] K. Liu *et al.*, "Thermal–electric nanogenerator based on the electrokinetic effect in porous carbon film," *Advanced Energy Materials*, vol. 8, no. 13, p. 1702481, 2018.
- [19] B. Bera and M. D. Sarkar, "Piezoelectricity in PVDF and PVDF based piezoelectric nanogenerator: A concept," *IOSR J. Appl. Phys.*, vol. 9, no. 3, pp. 95-99, 2017.

- [20] S. Wang, S. Niu, J. Yang, L. Lin, and Z. L. Wang, "Quantitative measurements of vibration amplitude using a contact-mode freestanding triboelectric nanogenerator," *ACS nano*, vol. 8, no. 12, pp. 12004-12013, 2014.
- [21] P. Bai *et al.*, "Integrated multilayered triboelectric nanogenerator for harvesting biomechanical energy from human motions," *ACS nano*, vol. 7, no. 4, pp. 3713-3719, 2013.
- [22] C. Rodrigues *et al.*, "Integrated study of triboelectric nanogenerator for ocean wave energy harvesting: Performance assessment in realistic sea conditions," *Nano Energy*, vol. 84, p. 105890, 2021.
- [23] Y. Xie *et al.*, "Rotary triboelectric nanogenerator based on a hybridized mechanism for harvesting wind energy," *ACS nano*, vol. 7, no. 8, pp. 7119-7125, 2013.
- [24] Z. L. Wang, "Triboelectric nanogenerators as new energy technology for self-powered systems and as active mechanical and chemical sensors," *ACS nano*, vol. 7, no. 11, pp. 9533-9557, 2013.
- [25] J. Luo and Z. L. Wang, "Recent advances in triboelectric nanogenerator based self-charging power systems," *Energy Storage Materials*, vol. 23, pp. 617-628, 2019.
- [26] P. Gipe, "Wind power," *Wind Engineering*, vol. 28, no. 5, pp. 629-631, 2004.
- [27] A. de O Falcão, "Control of an oscillating-water-column wave power plant for maximum energy production," *Applied Ocean Research*, vol. 24, no. 2, pp. 73-82, 2002.
- [28] F. Verástegui, Á. Lorca, M. Negrete-Pincetic, and D. Olivares, "Firewood heat electrification impacts in the Chilean power system," *Energy Policy*, vol. 144, p. 111702, 2020.
- [29] R. Fuller and L. Aye, "Human and animal power—The forgotten renewables," *Renewable energy*, vol. 48, pp. 326-332, 2012.
- [30] H. Ritchie and M. Roser, "Fossil fuels," *Our world in data*, 2017.
- [31] M. H. Dickson and M. Fanelli, *Geothermal energy*. Wiley, 2004.
- [32] P. P. Edwards, V. Kuznetsov, and W. I. David, "Hydrogen energy," *Philosophical Transactions of the Royal Society A: Mathematical, Physical and Engineering Sciences*, vol. 365, no. 1853, pp. 1043-1056, 2007.
- [33] S. V. Vassilev, C. G. Vassileva, and V. S. Vassilev, "Advantages and disadvantages of composition and properties of biomass in comparison with coal: An overview," *Fuel*, vol. 158, pp. 330-350, 2015.
- [34] D. Bodansky, *Nuclear energy: principles, practices, and prospects*. Springer Science & Business Media, 2007.
- [35] R. J. Pearson, A. B. Antoniazzi, and W. J. Nuttall, "Tritium supply and use: a key issue for the development of nuclear fusion energy," *Fusion Engineering and Design*, vol. 136, pp. 1140-1148, 2018.
- [36] A. Gorlov, "Tidal energy," *Elements of Physical Oceanography*, pp. 103-108, 2001.
- [37] K. A. Kvenvolden and T. D. Lorenson, "The global occurrence of natural gas hydrate," *Natural Gas Hydrates: Occurrence, Distribution, and Detection: Occurrence, Distribution, and Detection*, vol. 124, pp. 3-18, 2001.
- [38] L. Lakatos, G. Hevessy, and J. Kovács, "Advantages and disadvantages of solar energy and wind-power utilization," *World Futures*, vol. 67, no. 6, pp. 395-408, 2011.
- [39] I. Yüksel, "Hydropower for sustainable water and energy development," *Renewable and Sustainable Energy Reviews*, vol. 14, no. 1, pp. 462-469, 2010.
- [40] N. Sriram and M. Shahidehpour, "Renewable biomass energy," in *IEEE Power Engineering Society General Meeting, 2005*, 2005: IEEE, pp. 612-617.

- [41] P. Takahashi and A. Trenka, "Ocean thermal energy conversion," 1996.
- [42] "Questions and Answers - Making our energy system fit for our climate targets." (accessed.
- [43] G. Min, L. Manjakkal, D. M. Mulvihill, and R. S. Dahiya, "Triboelectric nanogenerator with enhanced performance via an optimized low permittivity substrate," *IEEE Sensors Journal*, vol. 20, no. 13, pp. 6856-6862, 2019.
- [44] M. Sarno, "Nanotechnology in energy storage: The supercapacitors," in *Studies in Surface Science and Catalysis*, vol. 179: Elsevier, 2020, pp. 431-458.
- [45] H. Xue *et al.*, "A wearable pyroelectric nanogenerator and self-powered breathing sensor," *Nano Energy*, vol. 38, pp. 147-154, 2017.
- [46] H. Ryu and S. W. Kim, "Emerging pyroelectric nanogenerators to convert thermal energy into electrical energy," *Small*, vol. 17, no. 9, p. 1903469, 2021.
- [47] J. Briscoe and S. Dunn, "Piezoelectric nanogenerators—a review of nanostructured piezoelectric energy harvesters," *Nano Energy*, vol. 14, pp. 15-29, 2015.
- [48] Z. Zhang *et al.*, "Deep learning-enabled triboelectric smart socks for IoT-based gait analysis and VR applications," *npj Flexible Electronics*, vol. 4, no. 1, pp. 1-12, 2020.
- [49] Z. Zhou *et al.*, "Wireless self-powered sensor networks driven by triboelectric nanogenerator for in-situ real time survey of environmental monitoring," *Nano Energy*, vol. 53, pp. 501-507, 2018.
- [50] G. Min *et al.*, "Ferroelectric-assisted high-performance triboelectric nanogenerators based on electrospun P(VDF-TrFE) composite nanofibers with barium titanate nanofillers," *Nano Energy*, vol. 90, p. 106600, 2021.
- [51] Y. Kumaresan, G. Min, A. S. Dahiya, A. Ejaz, D. Shakthivel, and R. Dahiya, "Kirigami and Mogul-Patterned Ultra-Stretchable High-Performance ZnO Nanowires-Based Photodetector," *Advanced Materials Technologies*, p. 2100804, 2021.
- [52] X. Pu *et al.*, "A self-charging power unit by integration of a textile triboelectric nanogenerator and a flexible lithium-ion battery for wearable electronics," *Advanced Materials*, vol. 27, no. 15, pp. 2472-2478, 2015.
- [53] C. Zhang, W. Fan, S. Wang, Q. Wang, Y. Zhang, and K. Dong, "Recent Progress of Wearable Piezoelectric Nanogenerators," *ACS Applied Electronic Materials*, 2021.
- [54] X.-S. Zhang, M. Han, B. Kim, J.-F. Bao, J. Brugger, and H. Zhang, "All-in-one self-powered flexible microsystems based on triboelectric nanogenerators," *Nano Energy*, vol. 47, pp. 410-426, 2018.
- [55] L. Xu *et al.*, "Coupled triboelectric nanogenerator networks for efficient water wave energy harvesting," *ACS nano*, vol. 12, no. 2, pp. 1849-1858, 2018.
- [56] S. Naik, R. Mukherjee, and B. Chaudhuri, "Triboelectrification: A review of experimental and mechanistic modeling approaches with a special focus on pharmaceutical powders," *International journal of pharmaceutics*, vol. 510, no. 1, pp. 375-385, 2016.
- [57] S. Niu *et al.*, "Theoretical study of contact-mode triboelectric nanogenerators as an effective power source," *Energy & Environmental Science*, vol. 6, no. 12, pp. 3576-3583, 2013.
- [58] Y. S. Zhou *et al.*, "Manipulating nanoscale contact electrification by an applied electric field," *Nano letters*, vol. 14, no. 3, pp. 1567-1572, 2014.
- [59] R. D. I. G. Dharmasena *et al.*, "Triboelectric nanogenerators: providing a fundamental framework," *Energy & Environmental Science*, vol. 10, no. 8, pp. 1801-1811, 2017.
- [60] S. Matsusaka, H. Maruyama, T. Matsuyama, and M. Ghadiri, "Triboelectric charging of

- powders: A review," *Chemical Engineering Science*, vol. 65, no. 22, pp. 5781-5807, 2010.
- [61] J. Wu, X. Wang, H. Li, F. Wang, W. Yang, and Y. Hu, "Insights into the mechanism of metal-polymer contact electrification for triboelectric nanogenerator via first-principles investigations," *Nano Energy*, vol. 48, pp. 607-616, 2018.
- [62] J. Wu, X. Wang, H. Li, F. Wang, and Y. Hu, "First-principles investigations on the contact electrification mechanism between metal and amorphous polymers for triboelectric nanogenerators," *Nano Energy*, vol. 63, p. 103864, 2019.
- [63] Z. L. Wang and A. C. Wang, "On the origin of contact-electrification," *Materials Today*, vol. 30, pp. 34-51, 2019.
- [64] F. A. Furfari, "A history of the Van de Graaff generator," *IEEE Industry Applications Magazine*, vol. 11, no. 1, pp. 10-14, 2005.
- [65] R. Herb, "Van de Graaff generators," in *Nuclear Instrumentation I/Instrumentelle Hilfsmittel der Kernphysik I*: Springer, 1959, pp. 64-104.
- [66] F.-R. Fan, Z.-Q. Tian, and Z. L. Wang, "Flexible triboelectric generator," *Nano energy*, vol. 1, no. 2, pp. 328-334, 2012.
- [67] R. Dharmasena, K. Jayawardena, C. Mills, R. Dorey, and S. Silva, "A unified theoretical model for Triboelectric Nanogenerators," *Nano Energy*, vol. 48, pp. 391-400, 2018.
- [68] H. Zhang, L. Yao, L. Quan, and X. Zheng, "Theories for triboelectric nanogenerators: A comprehensive review," *Nanotechnology Reviews*, vol. 9, no. 1, pp. 610-625, 2020.
- [69] Y. Li *et al.*, "Contribution of Ferromagnetic Medium to the Output of Triboelectric Nanogenerators Derived from Maxwell's Equations," *Advanced Energy Materials*, p. 2003921, 2021.
- [70] Z. L. Wang, "From contact-electrification to triboelectric nanogenerators," *Reports on Progress in Physics*, 2021.
- [71] S. Niu *et al.*, "Theory of sliding-mode triboelectric nanogenerators," *Advanced materials*, vol. 25, no. 43, pp. 6184-6193, 2013.
- [72] J. Shao *et al.*, "Studying about applied force and the output performance of sliding-mode triboelectric nanogenerators," *Nano Energy*, vol. 48, pp. 292-300, 2018.
- [73] Y. Mao, D. Geng, E. Liang, and X. Wang, "Single-electrode triboelectric nanogenerator for scavenging friction energy from rolling tires," *Nano Energy*, vol. 15, pp. 227-234, 2015.
- [74] Y. Li, G. Cheng, Z.-H. Lin, J. Yang, L. Lin, and Z. L. Wang, "Single-electrode-based rotary triboelectric nanogenerator and its applications as self-powered contact area and eccentric angle sensors," *Nano Energy*, vol. 11, pp. 323-332, 2015.
- [75] Q. Liang *et al.*, "Highly transparent triboelectric nanogenerator for harvesting water-related energy reinforced by antireflection coating," *Scientific reports*, vol. 5, no. 1, pp. 1-7, 2015.
- [76] S. A. Shankaregowda *et al.*, "Single-electrode triboelectric nanogenerator based on economical graphite coated paper for harvesting waste environmental energy," *Nano Energy*, vol. 66, p. 104141, 2019.
- [77] X. Pu *et al.*, "Ultrastretchable, transparent triboelectric nanogenerator as electronic skin for biomechanical energy harvesting and tactile sensing," *Science advances*, vol. 3, no. 5, p. e1700015, 2017.
- [78] N. Zhang, C. Tao, X. Fan, and J. Chen, "Progress in triboelectric nanogenerators as self-powered smart sensors," *Journal of Materials Research*, vol. 32, no. 9, pp. 1628-1646, 2017.
- [79] H. Zhang *et al.*, "A theoretical approach for optimizing sliding-mode triboelectric nanogenerator

- based on multi-parameter analysis," *Nano Energy*, vol. 61, pp. 442-453, 2019.
- [80] S. Niu *et al.*, "Theoretical investigation and structural optimization of single-electrode triboelectric nanogenerators," *Advanced Functional Materials*, vol. 24, no. 22, pp. 3332-3340, 2014.
- [81] S. Niu *et al.*, "Theory of freestanding triboelectric-layer-based nanogenerators," *Nano Energy*, vol. 12, pp. 760-774, 2015.
- [82] F. Peng *et al.*, "Facile fabrication of triboelectric nanogenerator based on low-cost thermoplastic polymeric fabrics for large-area energy harvesting and self-powered sensing," *Nano Energy*, vol. 65, p. 104068, 2019.
- [83] L. Jin *et al.*, "Manipulating relative permittivity for high-performance wearable triboelectric nanogenerators," *Nano Letters*, vol. 20, no. 9, pp. 6404-6411, 2020.
- [84] Y. Yu, Z. Li, Y. Wang, S. Gong, and X. Wang, "Sequential infiltration synthesis of doped polymer films with tunable electrical properties for efficient triboelectric nanogenerator development," *Advanced Materials*, vol. 27, no. 33, pp. 4938-4944, 2015.
- [85] H. Zou *et al.*, "Quantifying the triboelectric series," *Nature communications*, vol. 10, no. 1, pp. 1-9, 2019.
- [86] A. Chen, C. Zhang, G. Zhu, and Z. L. Wang, "Polymer materials for high-performance triboelectric Nanogenerators," *Advanced Science*, vol. 7, no. 14, p. 2000186, 2020.
- [87] V. F. Cardoso, D. M. Correia, C. Ribeiro, M. M. Fernandes, and S. Lanceros-Méndez, "Fluorinated polymers as smart materials for advanced biomedical applications," *Polymers*, vol. 10, no. 2, p. 161, 2018.
- [88] B. Dudem, D. H. Kim, A. R. Mule, and J. S. Yu, "Enhanced performance of microarchitected PTFE-based triboelectric nanogenerator via simple thermal imprinting lithography for self-powered electronics," *ACS applied materials & interfaces*, vol. 10, no. 28, pp. 24181-24192, 2018.
- [89] Y. Yang *et al.*, "Single-electrode-based sliding triboelectric nanogenerator for self-powered displacement vector sensor system," *Acs Nano*, vol. 7, no. 8, pp. 7342-7351, 2013.
- [90] T. Prada *et al.*, "Enhancement of output power density in a modified polytetrafluoroethylene surface using a sequential O₂/Ar plasma etching for triboelectric nanogenerator applications," *Nano Research*, pp. 1-8, 2021.
- [91] Y. Yang, Y. S. Zhou, H. Zhang, Y. Liu, S. Lee, and Z. L. Wang, "A single-electrode based triboelectric nanogenerator as self-powered tracking system," *Advanced Materials*, vol. 25, no. 45, pp. 6594-6601, 2013.
- [92] Z. Zhang, Y. Xu, D. Wang, H. Yang, J. Guo, and L.-S. Turng, "Enhanced performance of an expanded polytetrafluoroethylene-based triboelectric nanogenerator for energy harvesting," *Nano Energy*, vol. 60, pp. 903-911, 2019.
- [93] Y. Zhou, W. Deng, J. Xu, and J. Chen, "Engineering materials at the nanoscale for triboelectric nanogenerators," *Cell Reports Physical Science*, p. 100142, 2020.
- [94] P. Jiang *et al.*, "Signal output of triboelectric nanogenerator at oil–water–solid multiphase interfaces and its application for dual-signal chemical sensing," *Advanced Materials*, vol. 31, no. 39, p. 1902793, 2019.
- [95] D. Graiver, K. Farminer, and R. Narayan, "A review of the fate and effects of silicones in the environment," *Journal of Polymers and the Environment*, vol. 11, no. 4, pp. 129-136, 2003.
- [96] M. P. Wolf, G. B. Salieb-Beugelaar, and P. Hunziker, "PDMS with designer functionalities—

- Properties, modifications strategies, and applications," *Progress in Polymer Science*, vol. 83, pp. 97-134, 2018.
- [97] H. G. Menge, J. O. Kim, and Y. T. Park, "Enhanced Triboelectric Performance of Modified PDMS Nanocomposite Multilayered Nanogenerators," *Materials*, vol. 13, no. 18, p. 4156, 2020.
- [98] D. Tantraviwat *et al.*, "Highly dispersed porous polydimethylsiloxane for boosting power-generating performance of triboelectric nanogenerators," *Nano Energy*, vol. 67, p. 104214, 2020.
- [99] X. He, H. Guo, X. Yue, J. Gao, Y. Xi, and C. Hu, "Improving energy conversion efficiency for triboelectric nanogenerator with capacitor structure by maximizing surface charge density," *Nanoscale*, vol. 7, no. 5, pp. 1896-1903, 2015.
- [100] S. Y. Shin, B. Saravanakumar, A. Ramadoss, and S. J. Kim, "Fabrication of PDMS-based triboelectric nanogenerator for self-sustained power source application," *International Journal of Energy Research*, vol. 40, no. 3, pp. 288-297, 2016.
- [101] X.-Z. Jiang, Y.-J. Sun, Z. Fan, and T.-Y. Zhang, "Integrated flexible, waterproof, transparent, and self-powered tactile sensing panel," *ACS nano*, vol. 10, no. 8, pp. 7696-7704, 2016.
- [102] W. He, M. Sohn, R. Ma, and D. J. Kang, "Flexible single-electrode triboelectric nanogenerators with MXene/PDMS composite film for biomechanical motion sensors," *Nano Energy*, vol. 78, p. 105383, 2020.
- [103] T. Otitoju, A. Ahmad, and B. Ooi, "Polyvinylidene fluoride (PVDF) membrane for oil rejection from oily wastewater: A performance review," *Journal of Water Process Engineering*, vol. 14, pp. 41-59, 2016.
- [104] Y. Lu, Y. Jiang, Z. Lou, R. Shi, D. Chen, and G. Shen, "Wearable supercapacitor self-charged by P(VDF-TrFE) piezoelectric separator," *Progress in Natural Science: Materials International*, vol. 30, no. 2, pp. 174-179, 2020.
- [105] R. Liu *et al.*, "Poly (vinylidene fluoride) separators for next-generation lithium based batteries," *Nano Select*, 2021.
- [106] C. Baur, D. J. Apo, D. Maurya, S. Priya, and W. Voit, "Advances in piezoelectric polymer composites for vibrational energy harvesting," in *Polymer composites for energy harvesting, conversion, and storage*: ACS Publications, 2014, pp. 1-27.
- [107] Q. Jing and S. Kar-Narayan, "Nanostructured polymer-based piezoelectric and triboelectric materials and devices for energy harvesting applications," *Journal of Physics D: Applied Physics*, vol. 51, no. 30, p. 303001, 2018.
- [108] H.-Y. Mi *et al.*, "High-performance flexible triboelectric nanogenerator based on porous aerogels and electrospun nanofibers for energy harvesting and sensitive self-powered sensing," *Nano Energy*, vol. 48, pp. 327-336, 2018.
- [109] J. Kim *et al.*, "High-performance piezoelectric, pyroelectric, and triboelectric nanogenerators based on P(VDF-TrFE) with controlled crystallinity and dipole alignment," *Advanced Functional Materials*, vol. 27, no. 22, p. 1700702, 2017.
- [110] A. Šutka, K. Mālnieks, L. Lapčinskis, M. Timusk, K. Pudzs, and M. Rutkis, "Matching the directions of electric fields from triboelectric and ferroelectric charges in nanogenerator devices for boosted performance," *Iscience*, vol. 23, no. 4, p. 101011, 2020.
- [111] T. Huang *et al.*, "'Self-Matched' Tribo/Piezoelectric Nanogenerators Using Vapor-Induced Phase-Separated Poly (vinylidene fluoride) and Recombinant Spider Silk," *Advanced Materials*, vol. 32, no. 10, p. 1907336, 2020.
- [112] J.-H. Zhang, Y. Li, J. Du, X. Hao, and H. Huang, "A high-power wearable triboelectric

- nanogenerator prepared from self-assembled electrospun poly (vinylidene fluoride) fibers with a heart-like structure," *Journal of Materials Chemistry A*, vol. 7, no. 19, pp. 11724-11733, 2019.
- [113] G. Kalimuldina *et al.*, "A review of piezoelectric PVDF film by electrospinning and its applications," *Sensors*, vol. 20, no. 18, p. 5214, 2020.
- [114] G. L. Robertson, *Food packaging: principles and practice*. CRC press, 2005.
- [115] J. Jog, "Crystallization of polyethyleneterephthalate," *Journal of Macromolecular Science, Part C: Polymer Reviews*, vol. 35, no. 3, pp. 531-553, 1995.
- [116] L. Cheng, Q. Xu, Y. Zheng, X. Jia, and Y. Qin, "A self-improving triboelectric nanogenerator with improved charge density and increased charge accumulation speed," *Nature communications*, vol. 9, no. 1, pp. 1-8, 2018.
- [117] J. Xiong *et al.*, "Skin-touch-actuated textile-based triboelectric nanogenerator with black phosphorus for durable biomechanical energy harvesting," *Nature communications*, vol. 9, no. 1, pp. 1-9, 2018.
- [118] F. R. Fan *et al.*, "Highly transparent and flexible triboelectric nanogenerators: performance improvements and fundamental mechanisms," *Journal of Materials Chemistry A*, vol. 2, no. 33, pp. 13219-13225, 2014.
- [119] C. Liu, J. Li, L. Che, S. Chen, Z. Wang, and X. Zhou, "Toward large-scale fabrication of triboelectric nanogenerator (TENG) with silk-fibroin patches film via spray-coating process," *Nano Energy*, vol. 41, pp. 359-366, 2017.
- [120] K. Xia *et al.*, "A triboelectric nanogenerator based on cosmetic fixing powder for mechanical energy harvesting," *Microsystems & nanoengineering*, vol. 5, no. 1, pp. 1-9, 2019.
- [121] H. Wang, L. Xu, and Z. Wang, "Advances of High-Performance Triboelectric Nanogenerators for Blue Energy Harvesting," *Nanoenergy Advances*, vol. 1, no. 1, pp. 32-57, 2021.
- [122] F.-R. Fan, L. Lin, G. Zhu, W. Wu, R. Zhang, and Z. L. Wang, "Transparent triboelectric nanogenerators and self-powered pressure sensors based on micropatterned plastic films," *Nano letters*, vol. 12, no. 6, pp. 3109-3114, 2012.
- [123] D. W. Kim, J. H. Lee, J. K. Kim, and U. Jeong, "Material aspects of triboelectric energy generation and sensors," *NPG Asia Materials*, vol. 12, no. 1, pp. 1-17, 2020.
- [124] M. Akdere and T. Schneiders, "Modeling of the electrospinning process," in *Advances in Modeling and Simulation in Textile Engineering*: Elsevier, 2021, pp. 237-253.
- [125] Z. Wang *et al.*, "Two voltages in contact-separation triboelectric nanogenerator: from asymmetry to symmetry for maximum output," *Nano Energy*, vol. 69, p. 104452, 2020.
- [126] X. Tao *et al.*, "Significantly enhanced performance of triboelectric nanogenerator by incorporating BaTiO₃ nanoparticles in poly (vinylidene fluoride) film," *physica status solidi (a)*, vol. 216, no. 7, p. 1900068, 2019.
- [127] A. Ahmed *et al.*, "Triboelectric nanogenerator versus piezoelectric generator at low frequency (< 4 Hz): a quantitative comparison," *Iscience*, vol. 23, no. 7, p. 101286, 2020.
- [128] Y. Park *et al.*, "Ferroelectric multilayer nanocomposites with polarization and stress concentration structures for enhanced triboelectric performances," *ACS nano*, vol. 14, no. 6, pp. 7101-7110, 2020.
- [129] S. Cheon *et al.*, "High-performance triboelectric nanogenerators based on electrospun polyvinylidene fluoride–silver nanowire composite nanofibers," *Advanced Functional Materials*, vol. 28, no. 2, p. 1703778, 2018.
- [130] Y. Zi, H. Guo, Z. Wen, M.-H. Yeh, C. Hu, and Z. L. Wang, "Harvesting low-frequency (< 5 Hz)

- irregular mechanical energy: a possible killer application of triboelectric nanogenerator," *ACS nano*, vol. 10, no. 4, pp. 4797-4805, 2016.
- [131] Z. Zhang, X. Sun, Y. Chen, D. K. Debeli, and J. Guo, "Comprehensive dependence of triboelectric nanogenerator on dielectric thickness and external impact for high electric outputs," *Journal of Applied Physics*, vol. 124, no. 4, p. 045106, 2018.
- [132] A. Gomes, C. Rodrigues, A. Pereira, and J. Ventura, "Influence of thickness and contact area on the performance of pdms-based triboelectric nanogenerators," *arXiv preprint arXiv:1803.10070*, 2018.
- [133] G. Min, Y. Xu, P. Cochran, N. Gadegaard, D. M. Mulvihill, and R. Dahiya, "Origin of the contact force-dependent response of triboelectric nanogenerators," *Nano Energy*, vol. 83, p. 105829, 2021/05/01/ 2021, doi: <https://doi.org/10.1016/j.nanoen.2021.105829>.
- [134] D. M. Mulvihill and M. P. Sutcliffe, "Effect of tool surface topography on friction with carbon fibre tows for composite fabric forming," *Composites Part A: Applied Science and Manufacturing*, vol. 93, pp. 199-206, 2017.
- [135] S. Sneddon, Y. Xu, M. Dixon, D. Rugg, P. Li, and D. M. Mulvihill, "Sensitivity of material failure to surface roughness: a study on titanium alloys Ti64 and Ti407," *Materials & Design*, vol. 200, p. 109438, 2021.
- [136] D. Mulvihill, H. Brunskill, M. Kartal, R. Dwyer-Joyce, and D. Nowell, "A comparison of contact stiffness measurements obtained by the digital image correlation and ultrasound techniques," *Experimental Mechanics*, vol. 53, no. 7, pp. 1245-1263, 2013.
- [137] M.-L. Seol, S.-H. Lee, J.-W. Han, D. Kim, G.-H. Cho, and Y.-K. Choi, "Impact of contact pressure on output voltage of triboelectric nanogenerator based on deformation of interfacial structures," *Nano Energy*, vol. 17, pp. 63-71, 2015.
- [138] A. I. Uddin, P. S. Kumar, K. Hassan, and H. C. Kim, "Enhanced sensing performance of bimetallic Al/Ag-CNF network and porous PDMS-based triboelectric acetylene gas sensors in a high humidity atmosphere," *Sensors and Actuators B: Chemical*, vol. 258, pp. 857-869, 2018.
- [139] P. Vasandani, Z.-H. Mao, W. Jia, and M. Sun, "Relationship between triboelectric charge and contact force for two triboelectric layers," *Journal of Electrostatics*, vol. 90, pp. 147-152, 2017.
- [140] J. Song, L. Gao, X. Tao, and L. Li, "Ultra-Flexible and large-area textile-based triboelectric nanogenerators with a sandpaper-induced surface microstructure," *Materials*, vol. 11, no. 11, p. 2120, 2018.
- [141] H. Zhang, Y. Lu, A. Ghaffarinejad, and P. Basset, "Progressive contact-separate triboelectric nanogenerator based on conductive polyurethane foam regulated with a Bennet doubler conditioning circuit," *Nano energy*, vol. 51, pp. 10-18, 2018.
- [142] X.-W. Zhang *et al.*, "High-performance triboelectric nanogenerator with double-surface shape-complementary microstructures prepared by using simple sandpaper templates," *ACS Sustainable Chemistry & Engineering*, vol. 6, no. 2, pp. 2283-2291, 2018.
- [143] M.-L. Seol, J.-W. Han, D.-I. Moon, and M. Meyyappan, "Hysteretic behavior of contact force response in triboelectric nanogenerator," *Nano Energy*, vol. 32, pp. 408-413, 2017.
- [144] S. Li, Y. Zhou, Y. Zi, G. Zhang, and Z. L. Wang, "Excluding contact electrification in surface potential measurement using kelvin probe force microscopy," *ACS nano*, vol. 10, no. 2, pp. 2528-2535, 2016.
- [145] Y. S. Zhou *et al.*, "In situ quantitative study of nanoscale triboelectrification and patterning," *Nano letters*, vol. 13, no. 6, pp. 2771-2776, 2013.

- [146] W. Yang, X. Wang, H. Li, J. Wu, and Y. Hu, "Comprehensive contact analysis for vertical-contact-mode triboelectric nanogenerators with micro-/nano-textured surfaces," *Nano Energy*, vol. 51, pp. 241-249, 2018.
- [147] Y. Xu, G. Min, N. Gadegaard, R. Dahiya, and D. M. Mulvihill, "A unified contact force-dependent model for triboelectric nanogenerators accounting for surface roughness," *Nano Energy*, vol. 76, p. 105067, 2020.
- [148] Y. Nurmakanov, G. Kalimuldina, G. Nauryzbayev, D. Adair, and Z. Bakenov, "Structural and Chemical Modifications Towards High-Performance of Triboelectric Nanogenerators," *Nanoscale Research Letters*, vol. 16, no. 1, pp. 1-27, 2021.
- [149] C. Bu, F. Li, K. Yin, J. Pang, L. Wang, and K. Wang, "Research progress and prospect of triboelectric nanogenerators as self-powered human body sensors," *ACS Applied Electronic Materials*, vol. 2, no. 4, pp. 863-878, 2020.
- [150] J.-H. Seo, K. Zhang, M. Kim, W. Zhou, and Z. Ma, "High-performance flexible BiCMOS electronics based on single-crystal Si nanomembrane," *NPJ Flexible Electronics*, vol. 1, no. 1, pp. 1-7, 2017.
- [151] Y. Su *et al.*, "Alveolus-inspired active membrane sensors for self-powered wearable chemical sensing and breath analysis," *ACS nano*, vol. 14, no. 5, pp. 6067-6075, 2020.
- [152] Y. Su *et al.*, "A wireless energy transmission enabled wearable active acetone biosensor for non-invasive prediabetes diagnosis," *Nano Energy*, vol. 74, p. 104941, 2020.
- [153] Y. Su *et al.*, "Self-powered room temperature NO₂ detection driven by triboelectric nanogenerator under UV illumination," *Nano Energy*, vol. 47, pp. 316-324, 2018.
- [154] S. Wang *et al.*, "An integrated flexible self-powered wearable respiration sensor," *Nano Energy*, vol. 63, p. 103829, 2019.
- [155] J. Chen *et al.*, "Enhancing performance of triboelectric nanogenerator by filling high dielectric nanoparticles into sponge PDMS film," *ACS applied materials & interfaces*, vol. 8, no. 1, pp. 736-744, 2016.
- [156] Y. J. Kim, J. Lee, S. Park, C. Park, C. Park, and H.-J. Choi, "Effect of the relative permittivity of oxides on the performance of triboelectric nanogenerators," *RSC advances*, vol. 7, no. 78, pp. 49368-49373, 2017.
- [157] J. S. C. Koay, W. C. Gan, A. E. Soh, J. Y. Cheong, K. C. Aw, and T. S. Velayutham, "An overlapped electron-cloud model for the contact electrification in piezo-assisted triboelectric nanogenerators via control of piezoelectric polarization," *Journal of Materials Chemistry A*, vol. 8, no. 48, pp. 25857-25866, 2020.
- [158] H. Oh *et al.*, "Hard coating films of fluorine-containing ladder-like structured polysilsesquioxane as negative triboelectric materials for high-performance triboelectric generators," *Extreme Mechanics Letters*, p. 101533, 2021.
- [159] H. S. Nalwa, *Ferroelectric polymers: chemistry, physics, and applications*. CRC Press, 1995.
- [160] S. Wang, L. Lin, and Z. L. Wang, "Triboelectric nanogenerators as self-powered active sensors," *Nano Energy*, vol. 11, pp. 436-462, 2015.
- [161] J. Chen, H. Guo, C. Hu, and Z. L. Wang, "Robust triboelectric nanogenerator achieved by centrifugal force induced automatic working mode transition," *Advanced Energy Materials*, vol. 10, no. 23, p. 2000886, 2020.
- [162] K. Y. Lee *et al.*, "Controllable charge transfer by ferroelectric polarization mediated triboelectricity," *Advanced Functional Materials*, vol. 26, no. 18, pp. 3067-3073, 2016.

- [163] W. Seung *et al.*, "Boosting power-generating performance of triboelectric nanogenerators via artificial control of ferroelectric polarization and dielectric properties," *Advanced Energy Materials*, vol. 7, no. 2, p. 1600988, 2017.
- [164] Z. Wang *et al.*, "Ultrahigh electricity generation from low-frequency mechanical energy by efficient energy management," *Joule*, vol. 5, no. 2, pp. 441-455, 2021.
- [165] H. Niu, H. Zhou, and H. Wang, "Electrospinning: an advanced nanofiber production technology," *Energy Harvesting Properties of Electrospun Nanofibers*, pp. 1-44, 2020.
- [166] K. Gao, X. Hu, C. Dai, and T. Yi, "Crystal structures of electrospun PVDF membranes and its separator application for rechargeable lithium metal cells," *Materials Science and Engineering: B*, vol. 131, no. 1-3, pp. 100-105, 2006.
- [167] Z. He, F. Rault, M. Lewandowski, E. Mohsenzadeh, and F. Salaün, "Electrospun PVDF nanofibers for piezoelectric applications: A review of the influence of electrospinning parameters on the β phase and crystallinity enhancement," *Polymers*, vol. 13, no. 2, p. 174, 2021.
- [168] S. M. Damaraju, S. Wu, M. Jaffe, and T. L. Arinzeh, "Structural changes in PVDF fibers due to electrospinning and its effect on biological function," *Biomedical Materials*, vol. 8, no. 4, p. 045007, 2013.
- [169] H. Jiyong, Z. Yinda, Z. Hele, G. Yuanyuan, and Y. Xudong, "Mixed effect of main electrospinning parameters on the β -phase crystallinity of electrospun PVDF nanofibers," *Smart Materials and Structures*, vol. 26, no. 8, p. 085019, 2017.
- [170] X. Ma *et al.*, "Regulating the output performance of triboelectric nanogenerator by using P (VDF-TrFE) Langmuir monolayers," *Nano Energy*, vol. 66, p. 104090, 2019.
- [171] Y. Su *et al.*, "Piezoelectric fiber composites with polydopamine interfacial layer for self-powered wearable biomonitoring," *Nano Energy*, vol. 89, p. 106321, 2021.
- [172] H.-S. Kim and I.-K. Park, "Enhanced output power from triboelectric nanogenerators based on electrospun Eu-doped polyvinylidene fluoride nanofibers," *Journal of Physics and Chemistry of Solids*, vol. 117, pp. 188-193, 2018/06/01/ 2018, doi: <https://doi.org/10.1016/j.jpcs.2018.02.045>.
- [173] Y. Wu, J. Qu, W. A. Daoud, L. Wang, and T. Qi, "Flexible composite-nanofiber based piezo-triboelectric nanogenerators for wearable electronics," *Journal of Materials Chemistry A*, vol. 7, no. 21, pp. 13347-13355, 2019.
- [174] S. Cheon *et al.*, "High-Performance Triboelectric Nanogenerators Based on Electrospun Polyvinylidene Fluoride–Silver Nanowire Composite Nanofibers," *Advanced Functional Materials*, <https://doi.org/10.1002/adfm.201703778> vol. 28, no. 2, p. 1703778, 2018/01/01 2018, doi: <https://doi.org/10.1002/adfm.201703778>.
- [175] Y. Guo *et al.*, "All-fiber hybrid piezoelectric-enhanced triboelectric nanogenerator for wearable gesture monitoring," *Nano Energy*, vol. 48, pp. 152-160, 2018.
- [176] T. Bhatta *et al.*, "High-performance triboelectric nanogenerator based on MXene functionalized polyvinylidene fluoride composite nanofibers," *Nano Energy*, vol. 81, p. 105670, 2021/03/01/ 2021, doi: <https://doi.org/10.1016/j.nanoen.2020.105670>.
- [177] L. Shi *et al.*, "High-performance triboelectric nanogenerator based on electrospun PVDF-graphene nanosheet composite nanofibers for energy harvesting," *Nano Energy*, vol. 80, p. 105599, 2021/02/01/ 2021, doi: <https://doi.org/10.1016/j.nanoen.2020.105599>.
- [178] S. M. S. Rana *et al.*, "Electrospun PVDF-TrFE/MXene Nanofiber Mat-Based Triboelectric Nanogenerator for Smart Home Appliances," *ACS Applied Materials & Interfaces*, vol. 13, no.

- 4, pp. 4955-4967, 2021/02/03 2021, doi: 10.1021/acsami.0c17512.
- [179] D. Ali, B. Yu, X. Duan, H. Yu, and M. Zhu, "Enhancement of output performance through post-poling technique on BaTiO₃/PDMS-based triboelectric nanogenerator," *Nanotechnology*, vol. 28, no. 7, p. 075203, 2017/01/13 2017, doi: 10.1088/1361-6528/aa52b7.
- [180] H. Patnam, B. Dudem, S. A. Graham, and J. S. Yu, "High-performance and robust triboelectric nanogenerators based on optimal microstructured poly(vinyl alcohol) and poly(vinylidene fluoride) polymers for self-powered electronic applications," *Energy*, vol. 223, p. 120031, 2021/05/15/ 2021, doi: <https://doi.org/10.1016/j.energy.2021.120031>.
- [181] Y. Z. Liu, H. Zhang, J. X. Yu, Z. Y. Huang, C. Wang, and Y. Sun, "Ferroelectric P(VDF-TrFE)/POSS nanocomposite films: compatibility, piezoelectricity, energy harvesting performance, and mechanical and atomic oxygen erosion," *RSC Advances*, 10.1039/D0RA01769H vol. 10, no. 29, pp. 17377-17386, 2020, doi: 10.1039/D0RA01769H.
- [182] X. Ma *et al.*, "Regulating the output performance of triboelectric nanogenerator by using P(VDF-TrFE) Langmuir monolayers," *Nano Energy*, vol. 66, p. 104090, 2019/12/01/ 2019, doi: <https://doi.org/10.1016/j.nanoen.2019.104090>.
- [183] J. Chen *et al.*, "Self-powered triboelectric micro liquid/gas flow sensor for microfluidics," *ACS nano*, vol. 10, no. 8, pp. 8104-8112, 2016.
- [184] C. B. Han *et al.*, "Self-powered velocity and trajectory tracking sensor array made of planar triboelectric nanogenerator pixels," *Nano Energy*, vol. 9, pp. 325-333, 2014.
- [185] Q. Jing *et al.*, "Self-powered triboelectric velocity sensor for dual-mode sensing of rectified linear and rotary motions," *Nano Energy*, vol. 10, pp. 305-312, 2014.
- [186] T. K. Phan *et al.*, "A self-powered and low pressure loss gas flowmeter based on fluid-elastic flutter driven triboelectric nanogenerator," *Sensors*, vol. 20, no. 3, p. 729, 2020.
- [187] S. Shen, X. Xiao, and J. Chen, "Wearable triboelectric nanogenerators for heart rate monitoring," *Chemical Communications*, 2021.
- [188] B. Wang *et al.*, "New Hydrophobic Organic Coating Based Triboelectric Nanogenerator for Efficient and Stable Hydropower Harvesting," *ACS Applied Materials & Interfaces*, vol. 12, no. 28, pp. 31351-31359, 2020.
- [189] M. Xu *et al.*, "A highly-sensitive wave sensor based on liquid-solid interfacing triboelectric nanogenerator for smart marine equipment," *Nano Energy*, vol. 57, pp. 574-580, 2019.
- [190] B. Zhang *et al.*, "Self-powered acceleration sensor based on liquid metal triboelectric nanogenerator for vibration monitoring," *ACS nano*, vol. 11, no. 7, pp. 7440-7446, 2017.
- [191] C. Zhang *et al.*, "Harvesting Wind Energy by a Triboelectric Nanogenerator for an Intelligent High-Speed Train System," *ACS Energy Letters*, vol. 6, no. 4, pp. 1490-1499, 2021.
- [192] K. Parida, V. Bhavanasi, V. Kumar, R. Bendi, and P. S. Lee, "Self-powered pressure sensor for ultra-wide range pressure detection," *Nano Research*, vol. 10, no. 10, pp. 3557-3570, 2017.
- [193] X. Xia, Q. Liu, Y. Zhu, and Y. Zi, "Recent advances of triboelectric nanogenerator based applications in biomedical systems," *EcoMat*, vol. 2, no. 4, p. e12049, 2020.
- [194] J. Shao, T. Jiang, and Z. Wang, "Theoretical foundations of triboelectric nanogenerators (TENGs)," *Science China Technological Sciences*, vol. 63, no. 7, pp. 1087-1109, 2020.
- [195] Z. L. Wang, "On the expanded Maxwell's equations for moving charged media system—General theory, mathematical solutions and applications in TENG," *Materials Today*, 2021.
- [196] J. Luo *et al.*, "Integration of micro-supercapacitors with triboelectric nanogenerators for a flexible self-charging power unit," *Nano Research*, vol. 8, no. 12, pp. 3934-3943, 2015.

- [197] Y. Song *et al.*, "Integrated self-charging power unit with flexible supercapacitor and triboelectric nanogenerator," *Journal of Materials Chemistry A*, vol. 4, no. 37, pp. 14298-14306, 2016.
- [198] X. Shi, S. Chen, H. Zhang, J. Jiang, Z. Ma, and S. Gong, "Portable self-charging power system via integration of a flexible paper-based triboelectric nanogenerator and supercapacitor," *ACS Sustainable Chemistry & Engineering*, vol. 7, no. 22, pp. 18657-18666, 2019.
- [199] M. Parvez Mahmud, N. Huda, S. H. Farjana, M. Asadnia, and C. Lang, "Recent advances in nanogenerator-driven self-powered implantable biomedical devices," *Advanced Energy Materials*, vol. 8, no. 2, p. 1701210, 2018.
- [200] C. G. Núñez, L. Manjakkal, and R. Dahiya, "Energy autonomous electronic skin," *npj Flexible Electronics*, vol. 3, no. 1, pp. 1-24, 2019.
- [201] H. Wang and P. P. Mercier, "Near-Zero-Power Temperature Sensing via Tunneling Currents Through Complementary Metal-Oxide-Semiconductor Transistors," *Scientific Reports*, vol. 7, no. 1, p. 4427, 2017/06/30 2017, doi: 10.1038/s41598-017-04705-6.
- [202] T. Tekeste, H. Saleh, B. Mohammad, A. Khandoker, H. Jelinek, and M. Ismail, "A Nanowatt Real-Time Cardiac Autonomic Neuropathy Detector," *IEEE Transactions on Biomedical Circuits and Systems*, vol. 12, no. 4, pp. 739-750, 2018, doi: 10.1109/TBCAS.2018.2833624.
- [203] P. Escobedo, M. Bhattacharjee, F. Nikbakhtnasrabadi, and R. Dahiya, "Smart Bandage with Wireless Strain and Temperature Sensors and Battery-less NFC Tag," *IEEE Internet of Things Journal*, 2020.
- [204] Y. Wang, Y. Yang, and Z. L. Wang, "Triboelectric nanogenerators as flexible power sources," *npj Flexible Electronics*, vol. 1, no. 1, pp. 1-10, 2017.
- [205] D. Halliday, R. Resnick, and J. Walker, *Fundamentals of physics*. John Wiley & Sons, 2013.
- [206] S.-J. Park, M.-L. Seol, S.-B. Jeon, D. Kim, D. Lee, and Y.-K. Choi, "Surface engineering of triboelectric nanogenerator with an electrodeposited gold nanoflower structure," *Scientific reports*, vol. 5, no. 1, pp. 1-7, 2015.
- [207] D. Hong, Y.-M. Choi, and J. Jeong, "Test bed for contact-mode triboelectric nanogenerator," *Review of Scientific Instruments*, vol. 89, no. 6, p. 065110, 2018.
- [208] Y. Xiong and X. Tao, "Compression garments for medical therapy and sports," *Polymers*, vol. 10, no. 6, p. 663, 2018.
- [209] F. You, J. Wang, X. Luo, Y. Li, and X. Zhang, "Garment's pressure sensation (1): subjective assessment and predictability for the sensation," *International Journal of Clothing Science and Technology*, 2002.
- [210] M. H. Müser *et al.*, "Meeting the contact-mechanics challenge," *Tribology Letters*, vol. 65, no. 4, pp. 1-18, 2017.
- [211] L. Helseth, "Optical force sensing principle based on transparent elastomer with a rough surface," *Sensors and Actuators A: Physical*, vol. 263, pp. 667-676, 2017.
- [212] L. Dhakar *et al.*, "Large scale triboelectric nanogenerator and self-powered pressure sensor array using low cost roll-to-roll UV embossing," *Scientific reports*, vol. 6, no. 1, pp. 1-10, 2016.
- [213] J. Chen *et al.*, "Transparent triboelectric generators based on glass and polydimethylsiloxane," *Nano Energy*, vol. 30, pp. 235-241, 2016.
- [214] Z. Saadatania, S. G. Mosanenzadeh, E. Esmailzadeh, and H. Naguib, "Performance-enhanced triboelectric nanogenerator using polyimide aerogel for energy harvesting and sensing," in *Smart Materials and Nondestructive Evaluation for Energy Systems IV*, 2018, vol. 10601: International Society for Optics and Photonics, p. 1060105.

- [215] J. Peng *et al.*, "A composite generator film impregnated with cellulose nanocrystals for enhanced triboelectric performance," *Nanoscale*, vol. 9, no. 4, pp. 1428-1433, 2017.
- [216] P. Bai *et al.*, "Dipole-moment-induced effect on contact electrification for triboelectric nanogenerators," *Nano Research*, vol. 7, no. 7, pp. 990-997, 2014.
- [217] H. Chen *et al.*, "Effects of truck tire pressures on pavements," 1987.
- [218] L. Zhou, H. Brunskill, M. Pletz, W. Daves, S. Scheriau, and R. Lewis, "Real-time measurement of dynamic wheel-rail contacts using ultrasonic reflectometry," *Journal of Tribology*, vol. 141, no. 6, p. 061401, 2019.
- [219] J. G. Rose and T. E. Guenther, "Vehicle Tire-Pavement Interfacial Surface Pressure Measurements and Assessments," 2009.
- [220] A. Führböter, "Model and prototype tests for wave impact and run-up on a uniform 1: 4 slope," *Coastal engineering*, vol. 10, no. 1, pp. 49-84, 1986.
- [221] D. Kisacik, "Loading conditions due to violent wave impacts on coastal structures with cantilever surfaces," Ghent University, 2012.
- [222] J.-R. Henry and F. Bailey, "SLAMMING OF SHIPS: A CRITICAL REVIEW OF THE CURRENT STATE OF KNOWLEDGE," 1970.
- [223] J. C. Daidola, V. Mishkevich, and A. Bromwell, "Hydrodynamic Impact on Displacement Ship Hulls. An Assessment of the State of the Art. Bibliography," ROSENBLATT (M) AND SON INC NEW YORK, 1995.
- [224] J.-H. Yang, Y.-K. Kim, and J. Y. Lee, "Simplified process for manufacturing macroscale patterns to enhance voltage generation by a triboelectric generator," *Energies*, vol. 8, no. 11, pp. 12729-12740, 2015.
- [225] G.-G. Cheng *et al.*, "Effect of argon plasma treatment on the output performance of triboelectric nanogenerator," *Applied Surface Science*, vol. 412, pp. 350-356, 2017.
- [226] C. K. Jeong *et al.*, "Topographically-designed triboelectric nanogenerator via block copolymer self-assembly," *Nano letters*, vol. 14, no. 12, pp. 7031-7038, 2014.
- [227] K. Dong, X. Peng, and Z. L. Wang, "Fiber/fabric-based piezoelectric and triboelectric nanogenerators for flexible/stretchable and wearable electronics and artificial intelligence," *Advanced Materials*, vol. 32, no. 5, p. 1902549, 2020.
- [228] J. Chen *et al.*, "Actuation and sensor integrated self-powered cantilever system based on TENG technology," *Nano Energy*, vol. 64, p. 103920, 2019.
- [229] H. Guo *et al.*, "A highly efficient triboelectric negative air ion generator," *Nature Sustainability*, vol. 4, no. 2, pp. 147-153, 2021.
- [230] Y. Su *et al.*, "Self-Powered Respiration Monitoring Enabled By a Triboelectric Nanogenerator," *Advanced Materials*, vol. 33, no. 35, p. 2101262, 2021.
- [231] Y. Su *et al.*, "Muscle fibers inspired high-performance piezoelectric textiles for wearable physiological monitoring," *Advanced Functional Materials*, vol. 31, no. 19, p. 2010962, 2021.
- [232] S. Ma *et al.*, "Highly oriented electrospun P (VDF-TrFE) fibers via mechanical stretching for wearable motion sensing," *Advanced Materials Technologies*, vol. 3, no. 7, p. 1800033, 2018.
- [233] Y. Liu, H. Zhang, J. Yu, Z. Huang, C. Wang, and Y. Sun, "Ferroelectric P (VDF-TrFE)/POSS nanocomposite films: Compatibility, piezoelectricity, energy harvesting performance, and mechanical and atomic oxygen erosion," *RSC Advances*, vol. 10, no. 29, pp. 17377-17386, 2020.
- [234] L. Manjakkal, W. T. Navaraj, C. G. Núñez, and R. Dahiya, "Graphene-graphite polyurethane composite based high-energy density flexible supercapacitors," *Advanced Science*, vol. 6, no. 7,

- p. 1802251, 2019.
- [235] A. Pullanchiyodan, L. Manjakkal, S. Dervin, D. Shakthivel, and R. Dahiya, "Metal coated conductive fabrics with graphite electrodes and biocompatible gel electrolyte for wearable supercapacitors," *Advanced Materials Technologies*, vol. 5, no. 5, p. 1901107, 2020.
- [236] J. Kim *et al.*, "High-Performance Piezoelectric, Pyroelectric, and Triboelectric Nanogenerators Based on P(VDF-TrFE) with Controlled Crystallinity and Dipole Alignment," vol. 27, no. 22, p. 1700702, 2017, doi: <https://doi.org/10.1002/adfm.201700702>.
- [237] P. Martins, A. Lopes, and S. Lanceros-Mendez, "Electroactive phases of poly (vinylidene fluoride): Determination, processing and applications," *Progress in polymer science*, vol. 39, no. 4, pp. 683-706, 2014.
- [238] E. S. Hosseini, L. Manjakkal, D. Shakthivel, and R. Dahiya, "Glycine–chitosan-based flexible biodegradable piezoelectric pressure sensor," *ACS applied materials & interfaces*, vol. 12, no. 8, pp. 9008-9016, 2020.
- [239] D. Yoon, "Tetragonality of barium titanate powder for a ceramic capacitor application," *Journal of Ceramic Processing Research*, vol. 7, no. 4, p. 343, 2006.
- [240] M. Acosta *et al.*, "BaTiO₃-based piezoelectrics: Fundamentals, current status, and perspectives," *Applied Physics Reviews*, vol. 4, no. 4, p. 041305, 2017.
- [241] J. Nunes-Pereira *et al.*, "Energy harvesting performance of BaTiO₃/poly (vinylidene fluoride–trifluoroethylene) spin coated nanocomposites," *Composites Part B: Engineering*, vol. 72, pp. 130-136, 2015.
- [242] X. Hu *et al.*, "Improved Piezoelectric Sensing Performance of P (VDF–TrFE) Nanofibers by Utilizing BTO Nanoparticles and Penetrated Electrodes," *ACS applied materials & interfaces*, vol. 11, no. 7, pp. 7379-7386, 2019.
- [243] A. P. Indolia and M. Gaur, "Investigation of structural and thermal characteristics of PVDF/ZnO nanocomposites," *Journal of thermal analysis and calorimetry*, vol. 113, no. 2, pp. 821-830, 2013.
- [244] K. Yu, H. Wang, Y. Zhou, Y. Bai, and Y. Niu, "Enhanced dielectric properties of BaTiO₃/poly(vinylidene fluoride) nanocomposites for energy storage applications," *Journal of Applied Physics*, vol. 113, no. 3, p. 034105, 2013/01/21 2013, doi: 10.1063/1.4776740.
- [245] S. Gupta, D. Shakthivel, L. Lorenzelli, and R. Dahiya, "Temperature Compensated Tactile Sensing Using MOSFET With P(VDF-TrFE)/BaTiO₃ Capacitor as Extended Gate," *IEEE Sensors Journal*, vol. 19, no. 2, pp. 435-442, 2019, doi: 10.1109/JSEN.2018.2876678.
- [246] C. Xu *et al.*, "On the electron-transfer mechanism in the contact-electrification effect," *Advanced materials*, vol. 30, no. 15, p. 1706790, 2018.
- [247] I. Polonsky and L. Keer, "A numerical method for solving rough contact problems based on the multi-level multi-summation and conjugate gradient techniques," *Wear*, vol. 231, no. 2, pp. 206-219, 1999.
- [248] J. Zou *et al.*, "Coupled Supercapacitor and Triboelectric Nanogenerator Boost Biomimetic Pressure Sensor," vol. 8, no. 10, p. 1702671, 2018, doi: <https://doi.org/10.1002/aenm.201702671>.
- [249] W. Xiong *et al.*, "A wearable system based on core-shell structured peptide-Co₉S₈ supercapacitor and triboelectric nanogenerator," *Nano Energy*, vol. 66, p. 104149, 2019/12/01/ 2019, doi: <https://doi.org/10.1016/j.nanoen.2019.104149>.

- [250] A. Maitra *et al.*, "Trieoelectric Nanogenerator Driven Self-Charging and Self-Healing Flexible Asymmetric Supercapacitor Power Cell for Direct Power Generation," *ACS Applied Materials & Interfaces*, vol. 11, no. 5, pp. 5022-5036, 2019/02/06 2019, doi: 10.1021/acsami.8b19044.
- [251] J. McWhorter, L. Brown, and L. Khansa, "A wearable health monitoring system for posttraumatic stress disorder," *Biologically inspired cognitive architectures*, vol. 22, pp. 44-50, 2017.
- [252] R. Dahiya *et al.*, "Large-area soft e-skin: The challenges beyond sensor designs," *Proceedings of the IEEE*, vol. 107, no. 10, pp. 2016-2033, 2019.
- [253] W. Taube Navaraj *et al.*, "Nanowire FET based neural element for robotic tactile sensing skin," *Frontiers in neuroscience*, vol. 11, p. 501, 2017.
- [254] C. G. Núñez, W. T. Navaraj, E. O. Polat, and R. Dahiya, "Energy-autonomous, flexible, and transparent tactile skin," *Advanced Functional Materials*, vol. 27, no. 18, p. 1606287, 2017.
- [255] Y. Zhou, M. Shen, X. Cui, Y. Shao, L. Li, and Y. Zhang, "Trieoelectric nanogenerator based self-powered sensor for artificial intelligence," *Nano Energy*, p. 105887, 2021.
- [256] M. Soni, M. Bhattacharjee, M. Ntagios, and R. Dahiya, "Printed temperature sensor based on PEDOT: PSS-graphene oxide composite," *IEEE Sensors Journal*, vol. 20, no. 14, pp. 7525-7531, 2020.
- [257] L. Manjakkal, S. Dervin, and R. Dahiya, "Flexible potentiometric pH sensors for wearable systems," *RSC Advances*, vol. 10, no. 15, pp. 8594-8617, 2020.
- [258] Y. Su *et al.*, "Self-powered humidity sensor based on trieoelectric nanogenerator," in *2017 IEEE SENSORS*, 2017: IEEE, pp. 1-3.
- [259] Y. Kumaresan, O. Ozioko, and R. Dahiya, "Effect of Dielectric and Stiffness of Soft Material between the Electrodes of a Capacitive Pressure Sensor on its Performance," in *2020 IEEE International Conference on Flexible and Printable Sensors and Systems (FLEPS)*, 2020: IEEE, pp. 1-4.
- [260] M. Ntagios, H. Nassar, A. Pullanchiyodan, W. T. Navaraj, and R. Dahiya, "Robotic hands with intrinsic tactile sensing via 3D printed soft pressure sensors," *Advanced Intelligent Systems*, vol. 2, no. 6, p. 1900080, 2020.
- [261] Y. Kumaresan, O. Ozioko, and R. Dahiya, "Multifunctional electronic skin with a stack of temperature and pressure sensor arrays," *IEEE Sensors Journal*, 2021.
- [262] W. Navaraj and R. Dahiya, "Fingerprint-enhanced capacitive-piezolectric flexible sensing skin to discriminate static and dynamic tactile stimuli," *Advanced Intelligent Systems*, vol. 1, no. 7, p. 1900051, 2019.
- [263] O. Ozioko, P. Karipoth, P. Escobedo, M. Ntagios, A. Pullanchiyodan, and R. Dahiya, "SensAct: The Soft and Squishy Tactile Sensor with Integrated Flexible Actuator," *Advanced Intelligent Systems*, vol. 3, no. 3, p. 1900145, 2021.
- [264] R. S. Dahiya, P. Mittendorfer, M. Valle, G. Cheng, and V. J. Lumelsky, "Directions toward effective utilization of tactile skin: A review," *IEEE Sensors Journal*, vol. 13, no. 11, pp. 4121-4138, 2013.
- [265] Y. Zang, F. Zhang, C.-a. Di, and D. Zhu, "Advances of flexible pressure sensors toward artificial intelligence and health care applications," *Materials Horizons*, vol. 2, no. 2, pp. 140-156, 2015.
- [266] M. Li, J. Liang, X. Wang, and M. Zhang, "Ultra-sensitive flexible pressure sensor based on microstructured electrode," *Sensors*, vol. 20, no. 2, p. 371, 2020.
- [267] J. A. Rogers, "A diverse printed future," *Nature*, vol. 468, no. 7321, pp. 177-178, 2010.

- [268] D.-H. Kim *et al.*, "Epidermal electronics," *science*, vol. 333, no. 6044, pp. 838-843, 2011.
- [269] S. Xu, Y. Qin, C. Xu, Y. Wei, R. Yang, and Z. L. Wang, "Self-powered nanowire devices," *Nature nanotechnology*, vol. 5, no. 5, pp. 366-373, 2010.
- [270] Z. L. Wang, L. Lin, J. Chen, S. Niu, and Y. Zi, "Triboelectrification," in *Triboelectric Nanogenerators*: Springer, 2016, pp. 1-19.
- [271] A. K. Kasi, J. K. Kasi, M. Uddin, and M. Bokhari, "Triboelectric nanogenerator as self-powered impact force sensor for falling object," *Current Applied Physics*, vol. 20, no. 1, pp. 137-144, 2020.